A measurement of the relative decay rate of the charm quark into leptons

Dissertation der Fakultät für Physik
der Ludwig-Maximilians-Universität München

vorgelegt von
Aretina Magdalena David
aus Bukarest, Rumänien

München, den 10. Februar 2003

Erstgutachter: Prof. Dr. Walter Blum
Zweitgutachter: Prof. Dr. Arnold Staude

Contents

Zusammenfassung **v**

Abstract **vi**

1 Introduction **1**

2 Introduction to Charm Physics **4**
2.1 The Standard Model 4
2.1.1 Quarks 5
2.1.2 Gluons 6
2.1.3 Leptons 7
2.1.4 Electroweak Gauge Bosons 8
2.2 Z^0 Production in e^+e^- Collisions 8
2.3 The Production of c-Quarks in Z^0-Decays 9
2.4 B–$\overline{B}$ Mixing 10
2.5 Hadronisation 11
2.5.1 JETSET fragmentation model 12
2.5.2 The Peterson Model 13
2.6 Leptonic Decays of Charmed Hadrons 14
2.6.1 Correlation between the Charges of the Charm Quark and the Lepton 15
2.6.2 The Spectator Model and $BR(c \to l)$ 15

3 The ALEPH Detection System **18**
3.1 The Accelerator System 18
3.2 The ALEPH Detector 20
3.2.1 The Beam Pipe 22
3.2.2 The Silicon Vertex Detector (VDET) 22
3.2.3 The Inner Tracking Chamber (ITC) 23
3.2.4 The Time Projection Chamber (TPC) 24
3.2.5 The Electromagnetic Calorimeter (ECAL) 26
3.2.6 The Magnet and Hadronic Calorimeter (HCAL) 28
3.2.7 The Muon Chambers 29
3.2.8 The Trigger System 29

3.3 Particle Identification 30
3.3.1 Charged Particles 30
3.3.2 Neutral Particles 30
3.3.3 Energy Flow 31

4 The Monte Carlo Simulated Events 32
4.1 Monte Carlo Events in ALEPH 32
4.1.1 Event Generation 33
4.1.2 Detector Simulation and Event Reconstruction 35
4.2 MC–Data Consistency Checks 38
4.3 The MC Dataset Used 38

5 Analysis Principle and Initial Dataset 43
5.1 Method 43
5.2 Background Reduction 46
5.3 Data Samples 48
5.4 Preselection 48
5.5 Selection of the Charm Events 51
5.6 Selection of the Charm Events Leptonically Decaying 51

6 The Neuronal Nets 52
6.1 Analogy to Biological Neural Networks 52
6.2 Multilayer Perceptron 53
6.2.1 Architecture and Mathematical Description 54
6.2.2 The Process of Training 57
6.2.3 The RPROP Method 58
6.2.4 Dynamic Learning Parameters 59
6.2.5 End of Training 60
6.3 Implementation in JETNET 60
6.4 Neuronal Nets Used 61

7 The Charm Selection 65
7.1 Reconstruction of D-Decays 66
7.1.1 Particle Identification 66
7.1.2 Channel Identification 67
7.2 Application of NN to Charm Selection 69
7.3 The Working Point 74
7.3.1 Mass Window Cuts 74
7.3.2 NN Output Cuts 76
7.3.3 Channel Selection 80
7.4 MC Reweighting 84
7.5 The Final Selection 85

8 The (D, l) sample **90**
8.1 Lepton Detection with the ALEPH Detector 90
8.1.1 Electrons 90
8.1.2 Muons 91
8.1.3 Neutrinos 92
8.2 Corrections to the Number of Leptons Generated by Monte Carlo 92
8.3 Incorrect Assignment of the D Charge 93
8.4 Principle of Selection 95
8.5 Lepton Sample 97
8.6 Corrections of the Lepton Background 99
8.6.1 Corrections due to Fake Leptons ($\Delta N^{b,c}_{D,f}$) 99
8.6.2 Corrections due to b–D candidates ($\Delta N^{b}_{D,l}$) 101
8.6.3 Corrections due to Fake D Candidates ($\Delta N^{b,c}_{F,l}$) 104
8.6.4 Corrections due to Fake D and Lepton Candidates ($\Delta N^{b,c,uds}_{F,f}$) 105
8.7 Implementation of MC Corrections 106
8.8 Number of Leptons Found in Data 107

9 Error Analysis **108**
9.1 Statistical Errors 108
9.1.1 The Statistical Errors on the Number of D Candidates . 109
9.1.2 The Statistical Errors on the Number of (D, l) Candidates 111
9.1.3 Combining Statistical Errors due to D and (D, l) Candidates 112
9.1.4 Combining Statistical Errors due to Data and MC . . . 112
9.2 Systematic Uncertainties 113
9.2.1 Charge Tagging in Charm Quark Hemispheres 113
9.2.2 Fragmentation of b and c Quarks 114
9.2.3 Heavy Quarks from Gluon Splitting 115
9.2.4 B–$\overline{B}$ Mixing 116
9.2.5 Efficiencies of b Tagging 116
9.2.6 Uncertainties of Leptonic Branching Ratios 117
9.2.7 Lepton Background 118
9.2.8 Lepton Identification Efficiency 119
9.2.9 Modelling of Leptonic Decays 119
9.3 Combining Statistical and Systematic Errors 120
9.3.1 The Correlation Matrix of Statistical Errors 120
9.3.2 The Correlation Matrix of Systematic Errors 121
9.3.3 The Correlation Matrix of Total Errors 122
9.4 Combining Correlated Estimates of a Single Quantity using the BLUE Technique 123
9.5 The Final Error and its Components 124

10 Discussion of the Results **127**
10.1 Consistency Checks 127
10.1.1 Variation Within the Time of Data Acquisition 127
10.1.2 Variations of the Mass Cut $3\sigma_{MC}$ 129
10.2 The Final Result and Overall Discussion 132
10.3 Comparison to Other Measurements 133
10.3.1 Comparison to Past Measurements 133
10.3.2 Comparison to Contemporary Measurements 135
10.4 Outlook for Running and Future Experiments 137

A Monte Carlo Methods **140**

B More Diagrams of NN Outputs **142**

C Introduction to Probabilities and Statistics **147**

Acknowledgements **148**

Zusammenfassung

Ziel dieser Arbeit ist es das leptonische Verzweigungsverhältnis von Charm Quarks zu vermessen. Dafür wurden vier Millionen hadronische Z^0-Zerfaälle benutzt, die am LEP Experiment *ALEPH* zwischen 1991 und 1995 aufgezeichnet wurden. Diese Analyse ist selbstkalibrierend und beruht auf minimalem Gebrauch von Monte-Carlo Simulationen. Jedes Ereignis wurde in zwei Hemispheren aufgeteilt; wurde in der einen Hemisphere ein Charm Quark unter Beihilfe Neuronaler Netze identifiziert, so wurde in der anderen Hemisphere nach einem dazugehörigen Lepton gesucht. Aufgrund eines Datensatzes vollständig rekonstruierter D^0, D^+, D^{*+} Kandidaten war es möglich, ein Verzweigungsverhältnis $BR(c \to l + X) = 9.09 \pm 0.61\%$ ($l = e$ oder μ) zu erhalten. Der angegebene Fehler beinhaltet statistische und systematische Unsicherheiten.

Abstract

The inclusive rate of leptons produced from charmed particle decays from $Z^0 \to c\bar{c}$ has been measured using a data sample of four million hadronic Z^0 decays recorded by the $ALEPH$ experiment at LEP from 1991 to 1995. The analysis uses a double-tag and is self-calibrating, i.e. it makes minimum use of Monte Carlo simulated information. Each event is divided into two hemispheres; hemispheres containing c quarks are identified with a Neural Network analysis method. Lepton candidates are then searched for in the opposite hemisphere. Based on fully reconstructed D^0, D^+, D^{*+} candidates, a value of $BR(c \to l + X) = 9.09 \pm 0.61\%$ ($l = e$ or μ) is obtained. The uncertainty includes both the statistical and systematic components.

Chapter 1

Introduction

According to the Standard Model of particle physics (SM), matter is made of fermions, and forces are governed by bosons exchanged between elementary particles. The fermions come in three generations of leptons and quarks. The leptons are called: electron and electron neutrino (e & ν_e), muon and muon neutrino (μ & ν_μ), tau and tau neutrino (τ & ν_τ). The quarks are named: up and down (u & d), charm and strange (c & s), top and bottom (t & b).

The SM interactions between the elementary fermions are governed by three fundamental forces, strong, electromagnetic and weak, for which the bosons exchanged are called respectively gluons (g), photons (γ) and $W^{\pm}$ and Z^0 bosons. Development of the SM revealed that the electromagnetic and weak forces have a common origin, which is called the electroweak force. The fourth force, gravity, is attached in an ad-hoc fashion to the SM, and a self-consistent inclusion of this all-prevalent force is still being sought. More details of the SM are covered in Chapter 2.

Only the particles of the first generation (e, ν_e, u, d) constitute the visible matter in our universe, since the heavier second and third generation particles decay into these lighter ones. The decay of heavy quarks (s, c, b and t) and charged leptons (μ and τ) follows via the weak force, and the study of these decays is essential in order to increase the understanding of the SM.

The branch of physics investigating heavy quarks is called Heavy Flavour Physics. Inclusive semileptonic branching ratios, which involve events where heavy quarks decay into a lepton, are part of these studies. In recent years most effort in this branch has been directed towards the b and c quark systems. Precise vertex measurements with high-resolution detectors have enabled the

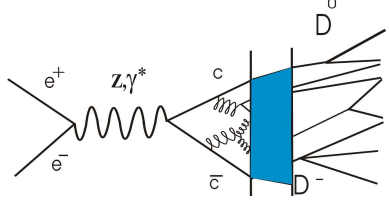

Figure 1.1: *Diagram symbolising charmed quark production at a primary vertex created by an e^+ e^- annihilation.*

separation of tracks of short–lived hadrons containing b or c quarks from the combinatorial background of the tracks emerging from the primary vertex (see Figure 1.1).

The inclusive charmed hadron semileptonic branching fraction *BR(c →l+X)* is the subject of this dissertation. It is defined as the average of all the semileptonic branching ratios of weakly decaying charm hadrons, weighted by their cross sections in prompt charm events $e^+e^- \to Z^0 \to c\bar{c}$:

$$BR(c \to l + X) \quad = \quad \frac{\sum_i \sigma_i \cdot BR(H_{c_i} \to Xl)}{\sum_i \sigma_i} \tag{1.1}$$

whereby $H_{c_i} =$ weakly decaying charmed hadron in channel i
$\sigma_i =$ cross section of charmed hadron H_{c_i}
$l =$ e, μ and
$X =$ anything which is produced together with the lepton.

In this formula, the lepton symbol l does not include the τ lepton because it is too heavy to be kinematically allowed in charmed hadron decays.

The present analysis is based on the hypothesis that, after the $Z^0 \to c\bar{c}$ transition, the first quark acts independently of the second. For a measurement of the leptonic decay of the first charm quark it should be, therefore, unimportant in which hadronic state the presence of the second quark is identified. The following analysis uses $D^0(1864)$, $D^+(1968)$ and $D^{*+}(2010)$ states for this because they can be efficiently reconstructed by ALEPH. The selected channels (see Section 5.1) gave a clear signal in the detector, their corresponding branching ratios from the Z^0 being large compared to all possible decay modes of the D^0, D^+ and D^{*+}.

Because the theoretical computation of $BR(c \to l + X)$ is very difficult and has only been performed for some of the hadrons H_c, this branching ratio measurement gives empirical information. Such empirical parameters are the result of a number of measurements performed at energies around the Z^0 resonance where leptonic decays of heavy quarks are involved [1]. The uncertainty on the world average of $BR(c \to l + X)$ can be improved by exploiting existing data samples as much as possible, as it will be shown in this thesis.

From 1989–1995 the e^+e^- Large Electron-Positron Collider (LEP) at the European Organization for Nuclear Research Center (CERN) had the collision energy of its electrons and positrons tuned to the mass of the neutral carrier of the weak force, the Z^0 boson. This is referred to as the LEP1 phase, and the four LEP experiments, ALEPH, DELPHI, L3 and OPAL, each collected a sample of approximately four million hadronic Z^0 decays. Detection of millions of Z^0 bosons and, later, thousands of $W^\pm$ bosons have allowed the LEP collaborations to make extremely precise tests of the SM. The Z^0 events at LEP exhibit clean topologies which makes it possible to obtain a high purity of charm-events. This was thus a very good environment for extracting the $BR(c \to l + X)$ branching ratio and performing many other electroweak

measurements.

The inclusive rate of leptons produced from charmed particle decays has been measured in previous experiments such as ARGUS [2, 3], MARK2 [4], JADE[5], DELCO [6]. These experiments took place at centre-of-mass energies significantly below the Z^0 mass, and some of these analyses depend strongly on the modelling of the lepton yield from b decays, which was needed for background subtraction. During recent years at LEP more effort has been made to determine the $BR(c \to l + X)$ with high accuracy by OPAL [7] and DELPHI [8], taking advantage of the most recent advances in c and b physics for selecting a sample enriched in $Z^0 \to c\bar{c}$ decays and reducing the $Z^0 \to b\bar{b}$ background.

The measurement of $BR(c \to l + X)$ described in this thesis is the first one performed by the ALEPH collaboration. The ALEPH detector was functioning well in the entire 1991–1995 period, and during 1997–1998 the collected data was completely reprocessed in order to improve the resolution of the track reconstruction. This ALEPH data set enables a measurement less dependent on the background from $e^+e^- \to b\bar{b}$ events by using the sample of events which includes highly energetic D^{*+}, D^0, D^+.

In $Z^0 \to c\bar{c}$ events, when the Z^0 is produced at rest as at LEP1, the c and $\bar{c}$ are produced back to back. Therefore, the hadrons containing the c and $\bar{c}$ appear in opposite hemispheres. Hence, in this analysis each event is divided into two hemispheres. In each hemisphere a charmed D candidate is searched for and reconstructed using the tracks identified as K and π mesons. Neural Networks are employed to select D mesons if there is ambiguity in the combination of the kaon and pion candidates. A lepton is then looked for in the hemisphere opposite to the one containing a reconstructed D candidate. The inverse ratio of the number of selected D candidates by the number of times it decays into a lepton in the opposite hemisphere yields a measurement of the inclusive semileptonic branching fraction of charm hadrons.

The theoretical basis of this measurement is presented in Chapter 2. A discussion of the accelerator and of the detector system is presented in Chapter 3. Chapter 4 describes the Monte Carlo generators used for this analysis. Chapter 5 details the principle of analysis, the data sample used and the event selection. In order to perform the final selection of charm events Neural Net techniques have been used to classify events as c or non–c, on a statistical basis using event–shape variables. An overview of the Neural Net technology is given in Chapter 6. The identification of charm events using reconstructed D mesons is presented in Chapter 7, along with a description of the event sample. The preparation of the lepton sample in charm-tagged events and the background estimation in this sample is described in Chapter 8. The calculation of the statistical and systematic errors follows in Chapter 9. Finnaly, various consistency checks of the result, the final result and comparisons with other experiments are presented in Chapters 10.

Chapter 2

Introduction to Charm Physics

The purpose of this chapter is to describe the production of charm quarks via the Z^0 and their subsequent fragmentation into hadrons and leptons. The Standard Model (SM), quarks, leptons and the Z^0 boson were introduced in Chapter 1 and are reiterated in Section 2.1. The production of Z^0 in e^+ e^- collisions (Section 2.2) and its decay into a $c\overline{c}$ pair (Section 2.3) are also presented. The mixing of hard b quarks is covered in Section 2.4. The quarks themselves are not observed in a detector. The basic picture is that each of them fragments into a jet of observable hadrons in a process called hadronisation, which is treated in Section 2.5. The decay models of the charmed particles are described at the end of this chapter, including the decay into leptons (Section 2.6).

2.1 The Standard Model

The fundamental interactions in nature are: gravitational, strong and electroweak interactions, which proceed via the exchange of bosons. The currently accepted and experimentally well-tested theory of strong and electroweak (electromagnetic and weak) interactions is called the Standard Model (SM), as explained in Chapter 1, while the incorporation of the gravity is still an unachieved goal.

The basic constituents of matter form three generations of fermions called quarks and leptons, displayed in Table 2.1. Every elementary particle has a corresponding anti-particle with an opposite electrical charge (unless the particle is electrically neutral). When discussing "particles" in this thesis, in general "particles and anti-particles" are meant, unless otherwise stated.

Fermions (after the Italian physicist Enrico Fermi) are mutually exclusive particles with half-integer intrinsic angular momentum spin (multiples of $\frac{1}{2}\hbar$). Two fermions cannot be simultaneously in a state with identical quantum numbers. Bosons (after the Indian physicist Satyendranath Bose) are particles

with integral intrinsic spin ($= 0\hbar,\ 1\hbar, ...$) and have the property that an unlimited number of them can occupy the same quantum state at the same time.

Generation	**Quarks**			**Leptons**		
	Name	Mass (MeV)	Electric charge in units of e	Name	Mass (Mev)	Electric charge in units of e
1^{st}	up(u)	2-8	$\frac{2}{3}$	Electron neutrino(ν_e)	$< 15 * 10^{-6}$	0
	down(d)	5-15	$-\frac{1}{3}$	Electron (e)	0.511	-1
2^{nd}	charm(c)	1000-1600	$\frac{2}{3}$	Muon neutrino(ν_μ)	< 0.17	0
	strange(s)	100-300	$-\frac{1}{3}$	Muon (μ)	105.7	-1
3^{rd}	top(t)	$170000 - 180000$	$\frac{2}{3}$	Tau neutrino(ν_τ)	< 24	0
	bottom(b)	4100-4500	$-\frac{1}{3}$	Tau (τ)	1777	-1

Table 2.1: *The basic constituents of matter in SM [9]*

2.1.1 Quarks

Due to the strong force, quarks only exist confined in composite particles. They have never been detected alone, and all searches for free quarks have had negative results. Quarks carry *fractional* electrical charge and an additional charge called *colour*. The colour fields are described by Quantum Chromodynamics (QCD), where the colour charges are labeled as *red* (R), *green* (G) and *blue* (B). When a particle carries no net colour charge (that is, it is a colour singlet), one defines its colour as white or black (as for mesons). The observed hadrons are composite particles made up of quarks, have a net integer electrical charge and are colour singlets. The hadrons occur into two classes:

- *baryons* (qqq - made out of three quarks) and

- *mesons* ($q\overline{q}$ - made out of a quark and an antiquark).

The subject of the present study are D mesons, signalising the presence of a *charm* (c) quark and an antidown ($\overline{d}$) or antiup ($\overline{u}$) quark (see Table 5.1).

This study deals with weak decays of charm quarks into leptons (Section 2.6.2). Quark flavour is not conserved in weak interactions, the weak quark eigenstates (d', s', b') being linear combinations of the mass eigenstates (d, s, b)

$$\begin{pmatrix} d' \\ s' \\ b' \end{pmatrix} = V_{CKM} \begin{pmatrix} d \\ s \\ b \end{pmatrix} \tag{2.1}$$

where the $Cabibbo - Kobayashi - Maskawa$ quark mixing matrix V_{CKM} [25] is

$$V_{CKM} = \begin{pmatrix} V_{ud} & V_{us} & V_{ub} \\ V_{cd} & V_{cs} & V_{cb} \\ V_{td} & V_{ts} & V_{tb} \end{pmatrix} \tag{2.2}$$

The elements of this matrix are of different by orders of magnitude and can be approximated by

$$V_{CKM} \sim \begin{pmatrix} 1 & s & s^3 \\ s & 1 & s^2 \\ s^3 & s^2 & 1 \end{pmatrix} \tag{2.3}$$

where $s \simeq 0.23$ [9].

2.1.2 Gluons

As stated earlier, quarks are not observed as free entities because they are subject to strong interactions to bind them together to form hadrons. The force between the colour charges carried by quarks is mediated by *gluons*. The carriers of the colour force are themselves coloured, in contrast to the electrically neutral photon.

In QCD gluons come in eight different colour combinations: $R\overline{G}$, $R\overline{B}$, $G\overline{R}$, $G\overline{B}$, $B\overline{R}$,$B\overline{G}$, $\sqrt{\frac{1}{2}}(R\overline{R} - G\overline{G})$ and $\sqrt{\frac{1}{6}}(R\overline{R} + G\overline{G} - 2B\overline{B})$. The remaining combination, $\sqrt{\frac{1}{3}}(R\overline{R} + G\overline{G} + B\overline{B})$, has no net colour and cannot mediate between colour charges.

A quark can emit a gluon reducing its momentum by a fraction z. The probability of gluon splitting at small angles is [13]:

$$P_{qq}(z) = \frac{4}{3} \cdot \frac{1 + z^2}{1 - z}. \tag{2.4}$$

In e^+ e^- collisions one can have

$$e^+e^- \rightarrow \gamma^* \rightarrow q\overline{q}g. \tag{2.5}$$

The presence of a gluon emission is signaled by a quark jet and a gluon jet in the final state.

If heavy quarks Q are produced ($Q = b, c$ for the case of this analysis), they decay (see Section 2.1.4) after a finite amount of time :

$$\begin{aligned} Q \rightarrow \quad qW^* \quad &\rightarrow qq^1\overline{q^2} \\ &\rightarrow ql\nu. \end{aligned}$$

and gluons can be emitted from the decay products. Because b and c are so long-lived that their energy scale is much less than 1 GeV, one has already a hadronised system when they decay and emitted gluons are not visible. Even if there is no visible gluon radiation, it has to be taken into account and calculate radiative corrections.

It is possible that a gluon splits into a $q\overline{q}$ pair. For small–angle emission, the probability that the quark q has a fraction z of the gluon momentum is [13]:

$$P_{qg}(z) = \frac{1}{2} \cdot [z^2 + (1 - z)]. \tag{2.6}$$

In particular, the decay of gluons to $c\overline{c}$ or $b\overline{b}$ constitutes a source of background for this measurement.

2.1.3 Leptons

Leptons appear to be point-like particles, without internal structure. There are six of them in total. Three of the leptons have electrical charge: e^-, μ^- and τ^- (and their anti-particles, e^+, μ^+ and τ^+). The other three are without electrical charge: the neutrinos ν_e, ν_μ, ν_τ (and the antineutrinos, $\overline{\nu_e}$, $\overline{\nu_\mu}$, $\overline{\nu_\tau}$).

The masses of charged leptons are well known, but definite masses have not yet been measured for neutrinos. The direct kinematic measurements do not exclude zero neutrino masses. However, experimental evidence for non-zero mass of neutrinos does exist [15].

A leptons carries the so–called lepton quantum number. The electron lepton number is

- 1 for e^- and ν_e,
- -1 for their anti-particles, e^+ and $\overline{\nu_e}$,
- 0 for the rest of leptons (and quarks).

In a similar way, muon and tau leptonic numbers are defined. Because leptonic numbers have to be conserved, when a lepton (e, μ or τ) is newly created, in W decays, its antineutrino counterpart (ν_e, ν_μ, ν_τ) is also produced.

The charged leptons e, μ and τ leptons can be easily detected. Neutrinos, however, are undetectable in the ALEPH detector because of their small cross sections. Their energies and momenta are inferred by using energy-momentum conservation laws.

2.1.4 Electroweak Gauge Bosons

The Gauge Bosons which mediate the electroweak force are the massive W^+, W^- , Z^0 and the massless photon (γ). The masses are listed in Table 2.2 [9].

	Photon	Z^0	W^+	W^-
Mass(GeV)	$< 2 \times 10^{-25}$	91.1882 ± 0.0022	$80.35 \pm 0.33(stat) \pm 0.017(syst)$	

Table 2.2: *Masses of the Gauge Bosons in the SM*

To accommodate the Gauge Bosons, the SM of electroweak interactions starts with massless Yang-Mills particles, denoted by W^1, W^2, W^3 and B. The two neutral particles, W^3 and B mix to produce two physical particles, the photon (represented by the field A) and the Z:

$$\begin{cases} A &= \sin\theta_W W^3 + \cos\theta_W B \\ Z &= \cos\theta_W W^3 - \sin\theta_W B \end{cases}$$

θ_W is called the weak mixing angle; it indicates the degree of mixing of the W^3 and B bosons to generate the photon and the Z^0. It is a fundamental parameter in SM. Its experimental value is given by $\sin^2\theta_W = 0.2321 \pm 0.0010$ [9]. Other two fundamental parameters in the SM include the Fermi constant $G_F = (1.16639 \pm 0.00001) \times 10^{-5}\,\text{GeV}$ [9] and the QCD strong coupling α_s, which are energy dependent. At the Z^0 peak α_s has presently the value [9] $\alpha_s(M_Z^2) = 0.1192 \pm 0.0028$.

2.2 Z^0 Production in e^+e^- Collisions

The physical Z^0 and $W^\pm$ bosons were discovered at the SPS $p\bar{p}$ collider at CERN in the 1980's, in the UA1 and UA2 experiments [18]. Both their masses were measured to within $\sim$ 2–3 GeV [10]. From 1989 onward the LEP e^+ e^- accelerator was running at the centre of mass energy of the Z^0 peak ($m_Z = 91\,\text{GeV}$) and boosted the precision of the measurements of the properties of the Z^0 boson.

The collision between an electron and a positron forms an energy dependent mixture of photon or/and Z^0. Therefore, the total cross section, $\sigma^{tot} = \sigma^{tot}(e^+e^- \to f^+f^-)$, for the e^-e^+ annihilation in quarks and leptons is composed of three terms:

$$\sigma^{tot}(s) = \sigma^{\gamma}(s) + \sigma^{\gamma Z}(s) + \sigma^{Z}(s). \tag{2.7}$$

The first term (σ^γ) corresponds to the photon, the third (σ^Z) corresponds to the Z^0, while the second ($\sigma^{\gamma Z}$) corresponds to the interference between

the photon and the Z^0. At energies near m_Z, the Z^0 term is dominant because the photon cross section is approximately 3000 times smaller, so that the Z^0–γ interference term is very small. The interference term is positive and decreases towards m_Z, it vanishes even before the energy is equal to m_Z, because radiative corrections, and decreases further and is negative at energies larger than m_Z.

The Z^0 line shape is described by a Breit-Wigner distribution, characterized by m_Z and Γ_Z, the mean and the width of the distribution (see Equation 2.8). The electrons and positrons can emit initial–state photon radiation (ISR) before annihilating. This reduces the height of the Z^0 peak and makes the shape asymmetric. The total shape of the Z^0 resonance is determined by

- the relativistic term s/m_Z^2 present in the denominator, which takes ISR effects partly into account and modifies the Breit-Wigner distribution to have a s–dependent width;
- the interference term, not symmetric around m_Z.

The cross section is larger when $\sqrt{s}$ is above the peak m_Z than below it. The cross section for the process $e^+e^- \to Z^0$ at the center of mass energy $\sqrt{s}$ is [20]:

$$\sigma_Z = \frac{12\pi}{m_Z^2} \cdot \frac{s\Gamma(Z^0 \to e^+e^-) \cdot \Gamma_Z}{(s - m_Z^2)^2 + s^2\Gamma_Z^2/m_Z^2} \tag{2.8}$$

LEP collided e^+ and e^- beams with momenta opposite in direction and equal in magnitude. Therefore, the Z^0 was produced at rest in the laboratory frame. The Z^0 decays after a time of approximatively 10^{-24} s into quarks and leptons.

2.3 The Production of c-Quarks in Z^0-Decays

A Z^0 can either decay leptonically or into a pair of quarks (which is dominant mode). In this analysis $Z^0 \to c\overline{c}$ is the channel of interest, while the other decay channels into heavier quarks, $Z^0 \to b\overline{b}$, or lighter quarks, $Z^0 \to q\overline{q}$ with $q = u, d, s$, are background. The t quark is too heavy to be produced from a Z^0 decay (the quark masses are shown in Tables 2.1 and 2.2).

The SM makes very explicit predictions for the branching ratios of the Z^0. For a decay to a lepton and an antilepton one has

$$\Gamma(Z^0 \to l\overline{l}) = \frac{\sqrt{2}G_F m_Z^3}{6\pi} \cdot R_l, \tag{2.9}$$

while for a decay to a quark and an antiquark one has

$$\Gamma(Z^0 \to q\overline{q}) = 3 \cdot \frac{\sqrt{2}G_F m_Z^3}{6\pi} \cdot R_q \tag{2.10}$$

The values for the relative couplings $R_f = \frac{1}{4} + (\frac{1}{2} - 2|Q_f|\sin^2\theta_W)^2$, shown in Table 2.3, are functions of $|Q_f|$, the absolute value for the charge of the

lepton or quark, respectively. The factor of 3 which appears in Equation 2.10 is due to the three colours of the quarks.

According to the SM, the branching ratio of the Z^0 to $f\overline{f}$ ($f = l, q$) is

$$BR(Z^0 \to f\overline{f}) \quad = \quad \frac{\Gamma(Z^0 \to f\overline{f})}{\Gamma} \tag{2.11}$$

Here Γ represents the full width of the Z^0, including its decays to neutrinos:

$$\Gamma \quad = \quad \sum_{u,d,c,s,b} \Gamma(Z^0 \to q\overline{q}) + \sum_{\nu_e,\nu_\mu,\nu_\tau,e,\mu,\tau} \Gamma(Z^0 \to l\bar{l}) \tag{2.12}$$

The numerical results for the Z^0 branching ratios, obtained from the Equations 2.9, 2.10 and 2.11, are listed in the last column of Table 2.3.

Process	Relative coupling R_f	Branching ratio into each process
$Z^0 \to \nu_e\overline{\nu}_e,\ \nu_\mu\overline{\nu}_\mu,\ \nu_\tau\overline{\nu}_\tau$	$\frac{1}{2}$	6.8%
$Z^0 \to e^+e^-,\ \mu^+\mu^-,\ \tau^+\tau^-$	$\frac{1}{4} + (\frac{1}{2} - 2\sin^2\theta_W)^2$	3.4%
$Z^0 \to u\overline{u},\ c\overline{c}$	$3[\frac{1}{4} + (\frac{1}{2} - \frac{4}{3}\sin^2\theta_W)^2]$	11.8 %
$Z^0 \to d\overline{d},\ s\overline{s},\ b\overline{b},$	$3[\frac{1}{4} + (\frac{1}{2} - \frac{2}{3}\sin^2\theta_W)^2]$	15.2 %

Table 2.3: *The coupling and probability of the Z^0 boson to different final states [14].*

Formula 2.10 requires additional QED and QCD corrections. These include corrections due to photon radiation by the incoming (e^-, e^+) (ISR) and the outgoing (f^-, f^+) quarks or leptons (called FSR, final state radiation), and the variation of α_s with energy. The QED corrections are negligible, while the QCD corrections amount to an additional factor of 1.03. Further corrections are due to virtual top–mass contributions and fermion mass effects. These result in a total correction factor of 1.05 to the $BR(Z^0 \to c\overline{c})$. The theoretical computed BR

$$BR(Z^0 \to c\overline{c})^{th} \quad = R_c \times \tfrac{\Gamma_{had}}{\Gamma_Z} = \quad 12.02 \tag{2.13}$$

is in excellent agreement [20] with the experimental value [9]:

$$BR(Z^0 \to c\overline{c})^{exp} \quad = \quad 12.4 \pm 0.6\% \tag{2.14}$$

2.4 B–$\overline{B}$ Mixing

The B^0 and $\overline{B^0}$ mesons can mix with each other; this is possible for two distinct mesons: the non-strange $B_d^0 = \overline{b}d$ and the strange $B_s^0 = \overline{b}s$. This mixing occurs only via common intermediate states, to which both the B^0 and $\overline{B^0}$ can couple, for an example see Figure 2.1.

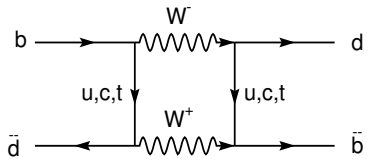

Figure 2.1: *The B mixing ($\overline{B}^0 \to B^0$).*

Mixing depends on both the quark masses and the CKM matrix. B mesons can oscillate during their lifetime and change the sign of the electrical charge of the constituent b quark. Thus the sign of the electrical charge of the associated lepton in an eventual leptonic decay is also changed. Since it is involved in the lepton selection (see Section 8.4), the b–mixing is taken into account when studying the systematic errors (see Section 9.2.4).

2.5 Hadronisation

In e^+e^- collisions at energies close to the Z^0 resonance ($\sqrt{s} = M_{Z^0} = 91.18\ GeV$), c–hadrons are produced due to the prompt $Z^0 \to c\overline{c}$ process, and non–promptly through $Z^0 \to b\overline{b}$ followed by $b \to cW$. To study the leptonic charm decay, it is necessary to use only the prompt charm-decays of the Z^0 and to eliminate the background from $b \to c$, which appears if non-prompt charm events are included in analysis.

As a part of the hadronic decay mode, R_c denotes the Z^0 hadronic branching fraction to c quarks. Its theoretical value, computed using the values of the branching ratios from Table 2.3, is:

$$R_c^{th} = \frac{\Gamma(c\overline{c})}{\sum_q \Gamma(q\overline{q})} = 17.05\% \tag{2.15}$$

which is within the uncertainty of the present experimental value [9]:

$$R_c^{exp} = 17.34 \pm 0.48\% \tag{2.16}$$

Z^0 production from e^+e^- and its decay into two quarks, is described by the electroweak theory. The subsequent production of gluons and more quarks from the Z^0 decay products is calculable in QCD using perturbation theory. However, the way quarks and gluons convert into hadrons cannot be exactly determined from perturbative QCD, because this transition occurs with small momentum transfer, where the coupling α_s is large. When the quarks produced by the Z^0 move further apart from each other, the colour field (see Section 2.1) (which acts among the gluons as well) increases linearly. The potential increases like $V(r) = \kappa r$, where κ is of the order of 1 GeV/fm. The strong color field is usually visualised by a string connecting two quarks, as illustrated in Figure 2.5. This string picture corresponds to a particular phenomenological model. Whether it is close to reality or not is subject of many QCD studies at LEP.

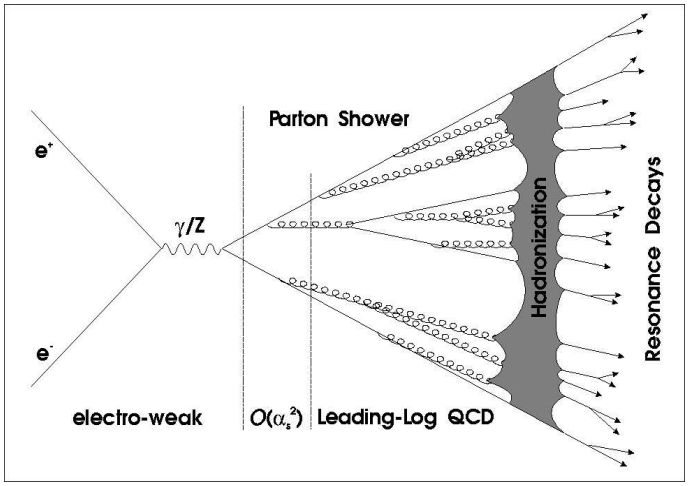

Figure 2.2: *The charmed hadrons' production mechanism. Mechanisms involved in the hadron production*

When the potential between the two initial quarks has reached a certain level because of the increased distance, the field breaks and a new quark antiquark pair is created from the vacuum. Due to this phenomenon, a cascade of $q\overline{q}$ pair production is generated. At the end they can be collected together to form the hadrons.

2.5.1 JETSET fragmentation model

Because the hadronisation phenomena cannot be treated using perturbation methods, phenomenological models have been developed in order to describe the data and make predictions. One of the best known algorithms for the simulation of hadron production is called JETSET [39], which is based on a model called string fragmentation.

A longitudinal axis is defined along the direction of the two initial quarks. The momenta $\vec{P}$ can be separated into a longitudinal component $\vec{P}_l$, and a transverse component, $\vec{P}_t$:

$$\vec{P} \;=\; \vec{P}_l + \vec{P}_t.$$

A transverse mass m_t can be defined as the invariant mass based only on the transverse component of momentum P_t:

$$m_t \;=\; \sqrt{E^2 - P_t^2}.$$

where

$$\begin{cases} E &= \textit{energy} \\ P_t &= \textit{transverse component of momentum} \end{cases}$$

In the string model the newly created hadron is given a fraction z of the variable $(E + P_l)$ from the initial quark:

$$z = \frac{(E + P_l)_{hadron}}{(E + P_l)_{initial\ quark}} \tag{2.17}$$

The remaining quark is left with the fraction $(1 - z)$ of $(E + P_l)_{initial\ quark}$, can further split into more hadrons.

The probability function (called the Lund fragmentation function), that the hadron takes the energy fraction z, for the light quarks u, d, and s, is :

$$f(z) = \frac{1}{z}\left(\frac{1-z}{z}\right)^a \exp\left(\frac{-bm_t^2}{z}\right) \tag{2.18}$$

The parameters a and b are determined by a fit to real data.

For the heavier charm and bottom quarks another fragmentation function is used, the so-called Peterson fragmentation [31].

2.5.2 The Peterson Model

Attaching a light anti-quark $\overline{q}$ to a heavy quark Q (or a diquark qq for baryon production) decelerates the heavy quark in the fragmentation process only slightly. Thus Q, $Q\overline{q}$, or Qqq should carry almost the same energy.

By using the approximation $m_H = m_Q$, the energy transfer ΔE for a fast moving quark Q fragmenting into a hadron $H = Q\overline{q}$ and a light quark q is:

$$\begin{aligned} \Delta E &= \sqrt{m_Q^2 + z^2p^2} + \sqrt{m_q^2 + (1-z)^2p^2} - \sqrt{m_Q^2 + p^2} \\ &\propto 1 - \tfrac{1}{z} - \tfrac{\xi_Q}{(1-z)} \end{aligned} \tag{2.19}$$

where

$$\begin{aligned} m_Q(m_q) &= \text{the mass of the heavy (light) constituent quark and} \\ \xi_Q &= {m_q}^2/{m_Q}^2. \end{aligned}$$

The proportionality relation in Equation 2.19 is obtained by considering

$$\begin{cases} m_Q \ll z \cdot p \\ m_q \ll (1-z) \cdot p \end{cases}$$

Taking a factor $1/z$ for longitudinal phase space, the momentum spectra of the heavy flavored hadrons (c- and b-hadrons) can be parametrized by the Peterson–fragmentation probability function:

$$f(z) = K\frac{1}{z \cdot (1 - (1/z) - \xi_Q/(1-z))^2} \tag{2.20}$$

The constant of normalisation K is fixed by summing over all hadrons containing Q, and depends on ξ_Q. Typical values for ξ_Q are $\xi_c = 0.04$ and

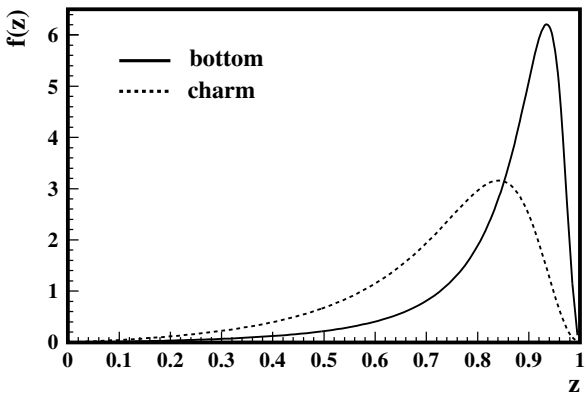

Figure 2.3: *The Peterson fragmentation function for the production of b-hadrons and c-hadrons*

$\xi_b = 0.0035$. In the Figure 2.3 the Peterson function is shown, for the particular case $\xi_b = 0.0045$ and $\xi_c = 0.03$, which are the values which result from fitting the ALEPH data, and are implemented in the Monte Carlo program used in this analysis.

Finally, once the parton–to–hadron transition is modeled, one can let the larger–mass hadrons decay into new particles. To describe these decays known branching ratios are used, except for most b–flavoured hadrons, where only very few branching ratios are known and JETSET uses some matrix approach to describe B–decays.

Other fragmentation models also exist, as for example HERWIG [33] (based on another approach, called cluster fragmentation). However, these are not described here, as they were not used for this analysis because JETSET gives a better modelling of the ALEPH data (see Figures 4.1 and 4.2).

2.6 Leptonic Decays of Charmed Hadrons

The coupling of all three leptons (e, μ, τ) to the Gauge Bosons (γ, Z^0, $W^{\pm}$) are equal due to the property of lepton universality, which would translate as equal branching ratios to all the three leptons. There are small differences between the branching ratios because of the differences in the lepton masses. However, they are small enough to be neglected in this analysis.

2.6.1 Correlation between the Charges of the Charm Quark and the Lepton

The emission of a leptons from a charm quark is described in the SM via a W boson decaying into a lepton, l^-, and an anti–neutrino, $\overline{\nu_l}$. Considering the fractional electrical charges of quarks, given in Table 2.1, and the electrical charge ± 1 of the W, the charm quark can couple in two different ways to the W:

- $c^{+\frac{2}{3}} \rightarrow W^+ s^{-\frac{1}{3}}$
- $c^{+\frac{2}{3}} \rightarrow W^+ d^{-\frac{1}{3}}$

The decay $c^{+\frac{2}{3}} \rightarrow W^+ b^{-\frac{1}{3}}$ is kinematically forbidden due to the quark masses (see Table 2.1). The coupling of the charm to W^- ($c^{+\frac{2}{3}} \rightarrow W^- q^{+\frac{5}{3}}$) is forbidden since it violates charge conservation (q with a charge of $+\frac{5}{3}$ has not been observed).

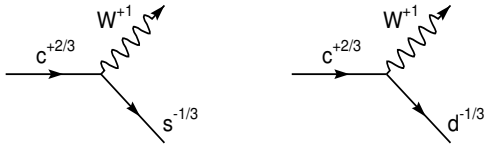

Figure 2.4: *The c decays via* W^+

If the W^+ decays as $W^+ \rightarrow l^+ \nu_l$, one has a positive lepton emission: $c \rightarrow l^+ + X$. For an anti–charm quark, of electrical charge $-2/3$, one follows the same argument and obtains $\overline{c} \rightarrow l^- + X$ (see Figure 2.4).

For $Z^0 \rightarrow c\overline{c}$ decays (see Section 5.1), when the anti–charmed ($\overline{c}$) particle decays, it corresponds to an emitted lepton with opposite electrical charge as its the detected charm (c) quark partner.

2.6.2 The Spectator Model and $BR(c \rightarrow l)$

A meson containing a charm quark (see Table 5.1) can be seen as a combination between a heavy c quark, which is active and decays, and a light q quark, which is passive and remains unchanged. This is called the *spectator model* – it considers that light quark constituents act as spectators which are assumed to play no role in the decay. Therefore, one can treat the semi-leptonic decays of hadrons containing a c quark in analogy with the decay of a free muon.

The decay of the charm quark is calculated via the W which can decay in two leptons (e and μ) and one pair of quarks ($u\overline{d}$, if one neglectes the decay into $u\overline{s}$). Since the u quark can exist in three colour combinations inside the D hadrons, there are three quark channels. This makes a total number of five open channels for the c quark decay. By rescaling the mass and counting the five open decay channels, one can infer the average charmed-particle lifetime

τ_c from the muon lifetime τ_μ which is [19]

$$\tau_\mu \quad = \quad \frac{192\pi^3}{{G_F}^2 {m_\mu}^5} = 2.18 \cdot 10^{-6} s, \tag{2.21}$$

thus supporting the spectator model approach. Assuming the mass of the charm quark to be $m_c = 1.5\,\mathrm{GeV}$, the inferred value τ_c is

$$\tau_c^{th} \quad = \frac{1}{5}(\frac{m_\mu}{m_c})^5 \tau_\mu \quad = 7 \cdot 10^{-13} s \tag{2.22}$$

This computed value τ_c is in very nice agreement with the experimentally measured value [23]:

$$\tau_c^{exp} \quad = \quad (7.7 \pm 1.2) \times 10^{-13} s$$

The width in the spectator model is given by the weak decay of the heavy quark, followed by the subsequent decay of the resulting virtual W boson. The weak decays of the charm quark can take place via (see Figure 2.5):

- an s quark ($c \to Ws$), characterised by the *CKM* matrix element $V_{cs} = 0.95$ [14] , or
- a d quark ($c \to Wd$), characterised by the *CKM* matrix element $V_{cd} = 0.23$ [14].

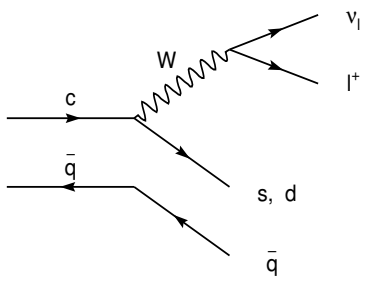

Figure 2.5: *Spectator model for c meson decay*

The $c \to b$ decay is forbidden by kinematics (see Table 2.1).

To get an order of magnitude estimation of the branching ratio one can first consider that all the quark masses have the same value and that the CKM matrix is equal to the identity matrix and, therefore, excludes the modes described by off-diagonal CKM elements (see Equation 2.2). For example, $c \to d$ is excluded by making the approximation $V_{cd} \ll V_{cs}$. Because of the three colours of quarks, the hadronic decay of the W to $u\overline{d}$ is three times as likely as the decay to $e\nu_e$, or $\mu\nu_\mu$. Therefore, one obtains:

$$BR(c \to l + X) = \quad \frac{1}{1+1+3} = \quad 20\%$$

If one takes into consideration the CKM matrix, one obtains:

$$BR(c \to l + X) = \quad \frac{1}{1+1+3\cdot(1+\frac{|V_{ud}|^2}{|V_{us}|^2})} = \quad 19\%$$

A more realistic approach is to take into account the different masses of the quarks. Then, the calculation for the semileptonic branching ratio becomes [19, 21]

$$BR(c \to l + X) \quad = \quad 12\% \tag{2.23}$$

where for the quark masses the lowest values in Table 2.1 are used.

Because the mass of the d, s and c quarks are only known within an error of about 40% (see Table 2.1), the question which effective masses should be used leads to uncertainties in the spectator model predictions for the branching ratios of more than 10% [19].

The present world average is $BR(c \to l + X) = (9.90 \pm 0.37)\%$ [9]. Thus it can be concluded that the semileptonic branching ratio of the charm quark can be accommodated in the spectator model (see Figure 2.6, case a), even if the predicted values for $BR(c \to l + X)$ are rather large. It is not possible [19] to obtain values of this branching ratio smaller than 10%.

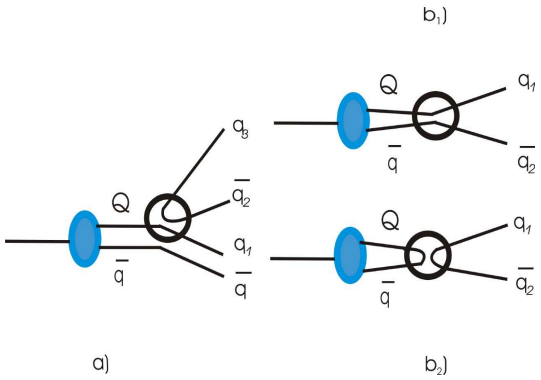

Figure 2.6: *Quark description of inclusive heavy-meson decay via a)spectator diagram, b_1) W exchange, b_2) weak annihilation. The empty circle symbolises the W boson.*

Non–spectator models also exist and they imply that both heavy and light quarks participate in the decay, for instance via W exchange as indicated in Figure 2.6 (cases b_1 and b_2), but these will not be discussed further here.

Chapter 3

The ALEPH Detection System

The CERN accelerator complex includes ten particle accelerators and colliders which can handle beams of electrons, positrons, protons, anti-protons and heavy ions. Before its shutdown in November 2000, the Large Electron Positron Collider [32] (LEP) at CERN was for 12 years the largest particle collider in the world. At Interaction Point 4 (PIT4) of the LEP complex, the ring passed through the ALEPH experimental zone. The acronym ALEPH stands for "Apparatus for LEp PHysics".

3.1 The Accelerator System

To produce the Z^0 boson a centre-of-mass energy of approximately 90 GeV is required. For a given beam energy, the highest center-of-mass energies are obtained using colliders and not fixed target machines. In an e^+e^- symmetric collider with e^+ and e^- having the same energy, a beam energy of approximately 45 GeV is needed, since electrons are elementary particles: all of their energy is available to produce new particles. In a proton–proton collider a beam energy of approximately 270 GeV is required, assuming that a quark in a proton carries about 1/6 of the proton energy. In addition, e^+e^- colliders have the advantages of a clean experimental environment that makes precision measurements much easier, because of a final state where almost all the particles are detected and of low backgrounds.

A view of the LEP ring is shown in Figure 3.1: It has a circumference of 27 km, is buried about 100 m underground with an inclination of 1.42 % because of geological and financial reasons. Bunches of unpolarized electrons and positrons raced round in opposite directions to be accelerated to produce centre-of-mass energies between 90 GeV up to 209 GeV.

For the LEP accelerator the electron beam was produced in two steps. Primary electrons were extracted from a metal surface (electron gun) to be injected into an electron cyclotron resonance (ECR), where the electron beam

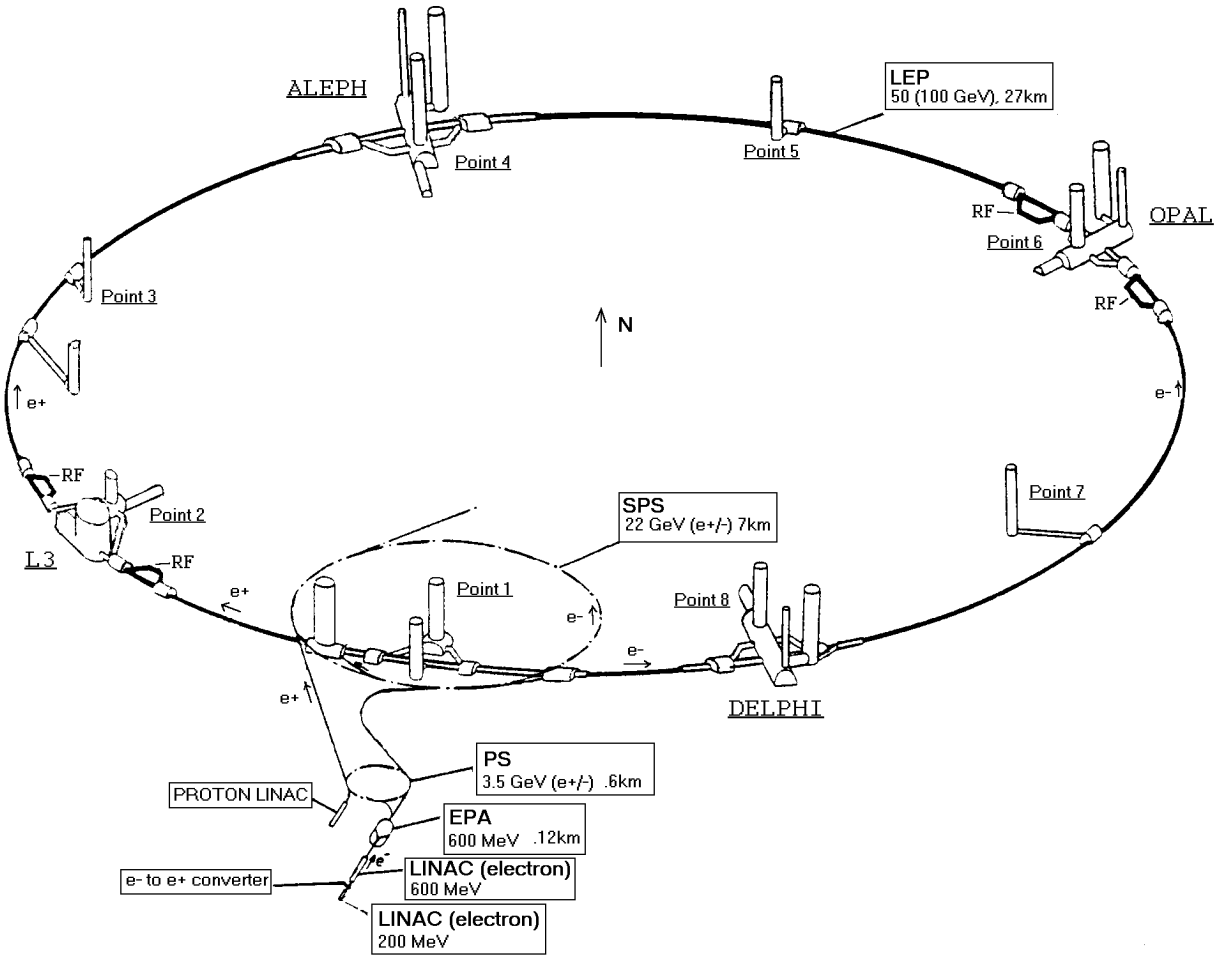

Figure 3.1: *The LEP accelerator complex at CERN*

was subsequently amplified. In order to reach the desired energy, the electrons and the positrons were accelerated through a set of four accelerators before finally reaching LEP.

The first stage of acceleration took place in a linear accelerator (Linac) where the final energy of electrons was 600 MeV, then stored in the Electron Positron Accumulator (EPA) ring. Positrons were produced via bremsstrahlung and γ–conversion by colliding an electron beam with a heavy metal target, which were then also stored in the EPA. The beams then passed through the Proton Synchrotron (PS), with a diameter of 200 m, injected into the larger Super Proton Synchrotron (SPS), with six km in circumference, and then passed to LEP for final acceleration.

At the Z^0 energy LEP worked with bunches each containing around 10^{11} particles to collide in the experimental areas (ALEPH, DELPHI, L3 and OPAL). The bunches of particles were focused using super-conducting quadrupole magnets to a transversal size of $10 \times 250\,\mu\mathrm{m}^2$.

On average, a fraction of about 10^{-8} of the bunch crossing produced the desired head-on e^+e^- collision. Typically the bunches circulated for hours, each bunch travelling round the ring in about 90 μs, and an average luminosity of $10^{31}\,\mathrm{cm}^{-2}\mathrm{s}^{-1}$ was achieved.

LEP began operation in the summer of 1989 and the collision energy of its electrons and positrons was designed to produce the Z^0. Data were taken at the peak 91.2 GeV and also taken slightly off-peak, to scan the Z^0 resonance, in the energy range of $86 - 96$ GeV. This first phase, 1989 until the middle of 1995, is called LEP 1. After autumn 1995, the energy was increased up to about one and a half its earlier value, reaching $130 - 136$ GeV (known as LEP 1.5). In the summer of 1996, LEP ran just above the threshold to produce pairs of the charged carriers of the weak force, the W^+ and W^- particles at 161 GeV, and continued searching for the Higgs boson. The running which took place from 1995 to 2000 is called LEP 2 and the energy was increased up to 209 GeV.

In the near future the LEP tunnel will host the Large Hadron Collider (LHC) machine. This will accelerate protons against protons and collide them at a center of mass energy of 14 TeV.

3.2 The ALEPH Detector

The ALEPH detector was a general purpose detector designed for a wide range of physics studies, from the Standard Model QCD and electroweak physics to beyond the SM searches for new particles. The ALEPH detector was built to measure the events created by the e^+e^- collisions at LEP. Z^0 bosons can decay hadronically with an average charged multiplicity $N_{ch} \approx 21$. This requires detailed tracking to reconstruct all tracks of charged particles. The rate of interesting events produced at the Z^0 peak was around 1 Hz. The ALEPH detector was therefore designed to be hermetic, fast and highly

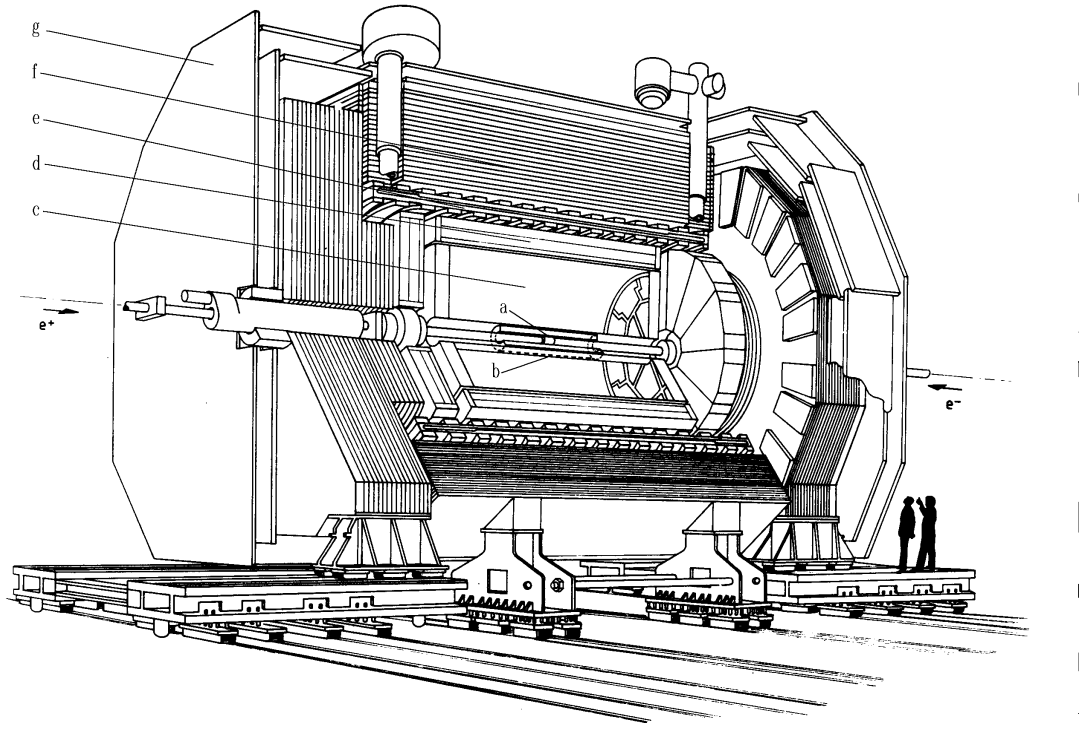

Figure 3.2: *View of the ALEPH detector. a:vertex detector, b:inner tracking chamber, c:time projection chamber, d:electromagnetic calorimeter, e:superconducting magnet coil, f:hadron calorimeter, g:muon detection chambers*

granular in order to collect as much information as possible for each of the events (see Figure 6.3).

In the following sections the different components of the detector are presented starting from the interaction point. ALEPH used polar coordinates, with origin at the interaction point and the positive z-axis along the e^- beam. A more detailed description of the ALEPH detector can be found in [34], and its performance in [36].

3.2.1 The Beam Pipe

The beam pipe in ALEPH had a diameter of 10.6 cm, was 5.5 m long and consisted of 1.5 mm thick aluminum. In order to hold the closest detector (VDET) a carbon-fiber tube was mounted around the beam pipe, over the interaction region.

3.2.2 The Silicon Vertex Detector (VDET)

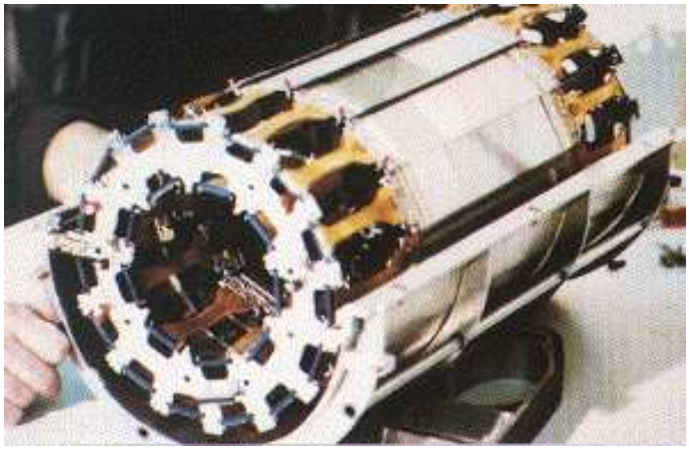

Figure 3.3: *The Vertex detector*

Installed in 1991, the vertex detector (a in Figure 6.3, Figure 3.3) provided high-precision measurements of the trajectories of charged particles close to the interaction point. This detector pioneered the use of double-sided silicon strip detectors, in order to achieve a three-dimensional vertex reconstruction capability. It consisted of 96 double-sided silicon wafers, each having dimensions of $5 \times 5 \times 0.03\,\mathrm{cm}^3$. These silicon wafers were arranged in two concentric cylinders around the beam, at radii of 6.3 cm for the inner and 10.9 cm for the outer layer. The detector covered an angular range down to $|\cos\theta| = 0.85$ for the inner layer and $|\cos\theta| = 0.69$ for the outer one.

Each wafer had 20 μm strips in both the $r\phi$ and rz plane. From near-normal incident hits of high momentum particles ($p > 2\,\mathrm{GeV}$) the average point resolution was measured to be 12 μm for both planes. For tracks with two space points in the VDET, and coming from $Z^0 \to q\overline{q}$ decays, the measured

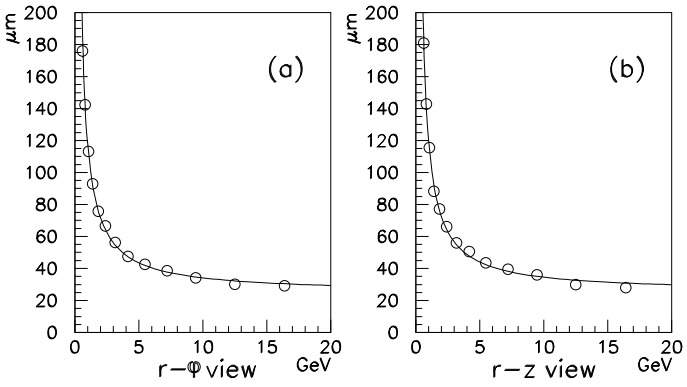

Figure 3.4: *Impact parameter resolution of tracks in $Z^0 \rightarrow qq$ events, where the points are data and the curve is MC simulated.*

impact parameter resolution (the impact parameter is the minimum radial distance of approach of a track to the beam position) could be parametrized as a function of the momenta of the tracks by:

$$\sigma = 25 + \frac{95}{p(GeV)} \ \mu\mathrm{m}$$

In Figure 3.4 the impact parameter resolution is shown for tracks with VDET hits in two layers as a function of their momentum.

Off-line reconstruction of the VDET data firstly involved reconstructing hit positions from the strip data and then adding those hits to improve the tracks already reconstructed in the TPC+ITC chambers of ALEPH (see below). In order to distinguish charm events, in particular from b-events, the capacity to separate the primary interaction points and secondary vertices played an essential role.

3.2.3 The Inner Tracking Chamber (ITC)

The ITC (*b* in Figure 6.3, Figure 3.5) had two functions.

1. It provided up to 8 tracking points in the $r\phi$ plane which were used in the reconstruction.
2. It provided the only tracking information used by the Level-1 Trigger.

The ITC was a multi-wire drift chamber providing precise spatial measurements of traversing charged particles. It was a cylindrical tube of 2 m length, with an inner radius of 128 mm and an outer one of 285 mm. It consisted of 960 gold-plated tungsten sense wires, with a diameter of 30 μm, which were strung parallel to the beam direction and had an operation potential of 2 kV. The wires were arranged in eight concentric circles around the beam pipe, with 96 wires in each of the four inner layers and 144 wires in each of the four outer layers. The drift cells of the ITC were hexagonal in the structure, with the sense wire being surrounded by six field wires of diameter 147 μm at

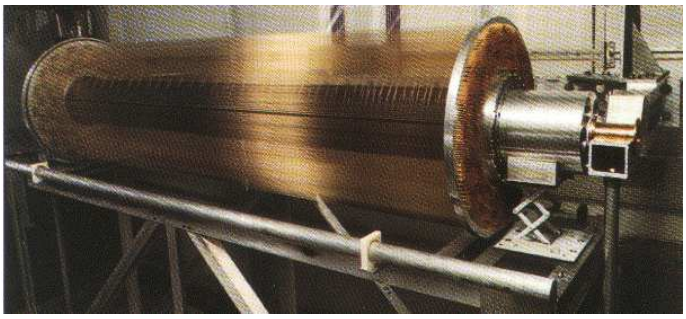

Figure 3.5: *The inner tracking chamber*

ground potential. The maximum drift distance varied between 4.7 mm (for the cells in the fifth layer) and 6.4 mm (for the cells in the fourth layer).

The coordinates of the incident particle in the $r\phi$ plane were measured using the drift time. The resolution in this plane was measured to be 150 μm. The z-coordinate was determined by comparing the arrival time of the pulse at both ends of the wire. The resolution in z was around 50 mm. The active region of the ITC extended from $R_{inner} = 160$ to $R_{outer} = 260$ mm.

3.2.4 The Time Projection Chamber (TPC)

The time projection chamber (c in Figure 6.3, Figure 3.6) measured the three-dimensional trajectory and the ionisation density dE/dx of traversing charged particles. The chamber was a gas filled cylindrical structure (4.4 m in length, $R_{inner} = 0.31$ m, $R_{outer} = 1.8$ m) with axis parallel to the beam pipe. It had a central membrane held at high negative potential, creating an electrical drift field parallel to the beam (11 kV/m), and had planar wire chambers at both ends. During the passage through the TPC, the charged particle induced ionisation in the Ar/CH_4 (91%/9%) gas mixture and the resulting electrons drifted, due to the applied electrical field, to one of the two end-plates mounted on each side of the chamber. On arrival at an end–plate the electrons induced an ionisation avalanche in one of 18 proportional wire chambers (sectors), which can be seen in Figure 3.6 arranged in a hexagonal fashion in the rϕ-plane (6 inner and 12 outer), thus provided a measured point in $r\phi$ via pads (see Figure 3.7) and z via arrival time.

The trajectory of a charged particle inside the TPC was helical due to the magnetic field produced by the solenoid (see Section 3.2.6). By measuring the sagitta of its arc projected on the end–plate gave the curvature radius, which was proportional to the inverse of the particle's momentum perpendicular to the magnetic field.

The TPC provided up to 21 three-dimensional points for $|\cos(\theta_{max})| = 0.79$, and a decreasing number of points for smaller angles. The relative accuracy of the reconstructed momenta was:

$$\Delta p/p \;=\; 1.2 \cdot 10^{-3}\,(\mathrm{GeV})^{-1} \cdot p \qquad (3.1)$$

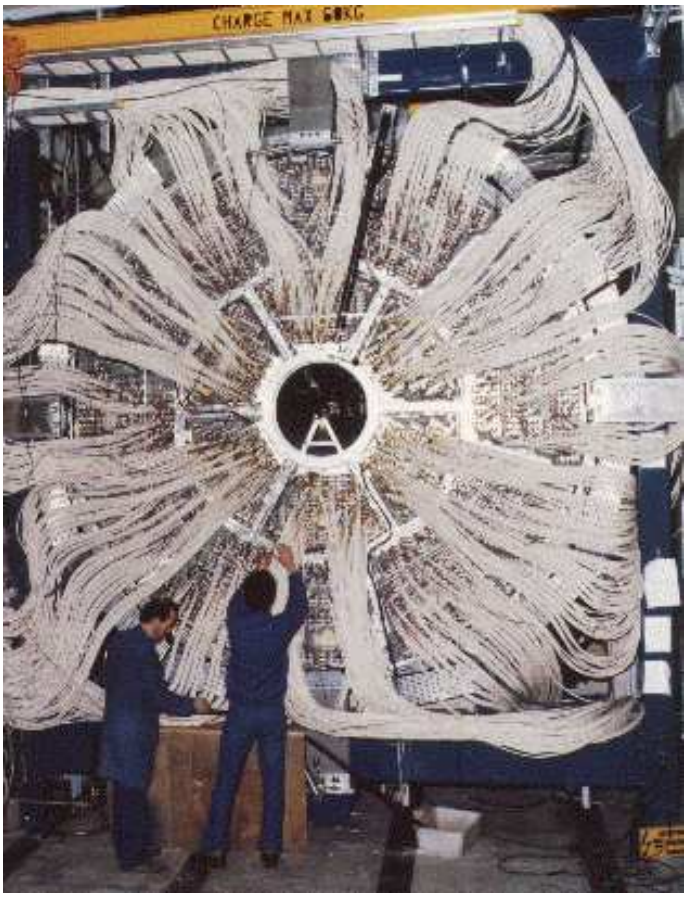

Figure 3.6: *The time projection chamber seen from the outside*

In combination with the ITC this resolution was then

$$\Delta p/p \;=\; 0.8 \cdot 10^{-3}\ (GeV)^{-1} \cdot p \tag{3.2}$$

For tracks measured by all the three devices (VDET, ITC and TPC) a momentum resolution of

$$\Delta p/p \;=\; 0.67 \cdot 10^{-3}\ (GeV)^{-1} \cdot p \tag{3.3}$$

was obtained for 45 GeV muons.

The ionisation density dE/dx of the particle track was measured via the wire–chambers sectors and permitted, for example, the separation of electrons, pions, kaons and protons over a limited momentum range. Up to 340 ionisation measurements were provided for each charged track, and the dE/dx resolution of 4.5% measured for Bhabha electrons. In Figure 3.7 the fitted dE/dx parameterisation is overlaid for electrons, muons, pions, kaons and protons.

The dependence of the mean dE/dx on the particle momentum was measured from the data. When a charged track was assumed to belong to a particular type of particle, the energy loss was computed based on the standard

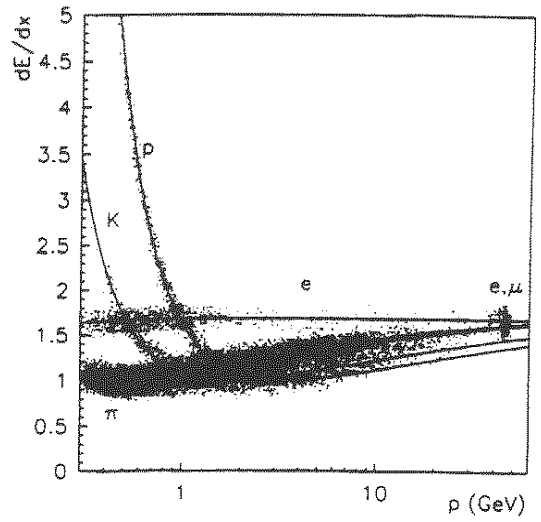

Figure 3.7: *The measured dE/dx versus particle momentum*

mass for that type. The energy loss distribution has a Landau shape; for the purposes of the measurement a truncated energy loss distribution was used. For each value p of the momentum, the truncated energy loss distribution had a approximately Gaussian shape, characterized by a standard deviation. The R_I estimator was defined as:

$$R_I = \frac{dE/dx - \langle dE/dx(T,p)\rangle}{\sigma(T,p)} \tag{3.4}$$

In Equation 3.4, $\langle dE/dx(T,p)\rangle$ is the theoretically expected energy loss for a specific type of particle T (electron, kaon, pion or proton), and $\sigma(T,p)$ is the standard deviation of the truncated energy loss distribution.

The typical separation, in standard deviations, between the particle species in hadronic events, was the most important parameter for particle identification. In the relativistic region ($p > 2\,\mathrm{GeV}$) the π-K separation was possible at about 2σ. In Figure 3.8 the average separation between electrons and pions, pions and kaons, and kaons and protons in hadronic Z^0 decays has been plotted.

3.2.5 The Electromagnetic Calorimeter (ECAL)

The Electromagnetic CALorimeter (ECAL), d in Figure 6.3, was designed to provide high angular resolution and good electron identification. It was a highly granular hermetic detector (97.8% of $4\,\pi$). ECAL consisted of three parts, the barrel in the central detector and two end-caps, which were all situated inside the solenoidal magnetic field of 1.5 T (see Section 3.2.6). Each of these parts was segmented into 12 modules, which covered a ϕ interval of 30° each. Furthermore, the end-cap modules were tilted by 15° with respect to the barrel ones.

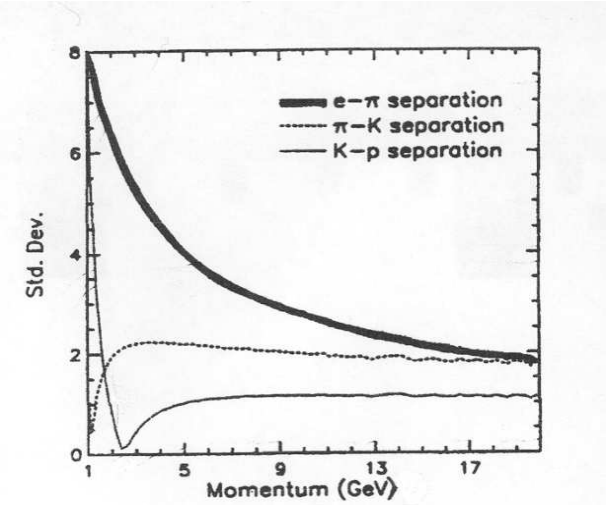

Figure 3.8: *The average R_I energy loss separation in standard deviations between particle types as a function of momentum*

Each module was formed by 45 alternating layers of lead absorber and proportional wire chambers, corresponding to 22 radiation lengths. The proportional wire chambers consisted of aluminum extrusions, containing 25 μm gold plated tungsten wires at the center, in a Xe/CO_2 gas mixture (80%/20%). The ionisation of an electromagnetic shower produced in the lead sheet was amplified in an avalanche around the wire (anode) and read out via cathode pads placed on the open side of the extrusion. The pads of consecutive layers formed projective towers with a mean aperture of $0.8^\circ \times 0.8^\circ$ pointing toward the interaction point.

A barrel module consisted of 4096 towers and an end cap module of 1024 individual towers, thus giving a total of 73728 towers for the whole electromagnetic calorimeter. The information of these towers was divided electronically into three longitudinal parts (stacks), corresponding to four radiation lengths (10 layers) for the first stack, nine radiation lengths for the second stack (23 layers) and for nine radiation lengths for the third stack (12 layers). Each charged track was extrapolated from the end of the TPC and a crossing point was computed in each of the three stacks of the ECAL. This allowed the determination, in each stack, of the four towers closest to the extrapolated track.

The R_T estimator, related to the transverse profile of the electromagnetic shower, was defined as:

$$R_T = \frac{E_4/p - \langle E_4/p \rangle}{\sigma_{E_4/p}} \tag{3.5}$$

where E_4 represents the energy deposit in the four leading towers, and p

represents the momentum of the charged track measured in the TPC.

$$E_4 = \sum_{i=1}^{4} \sum_{j=1}^{3} {E^j}_i \tag{3.6}$$

${E^j}_i$ is the energy deposited in the i^{th} selected tower of the j^{th} stack.

The R_L estimator, measuring the electromagnetic shower depth, was defined as:

$$R_L = \frac{X_L - \langle X_L \rangle}{\sigma_{X_L}}. \tag{3.7}$$

The quantity X_L is the inverse of the mean position of the longitudinal energy deposition of the shower:

$$X_L = \frac{E_4}{\sum_{i=1}^{4} \sum_{j=1}^{3} {E^j}_i S_j} \tag{3.8}$$

where S_j is the mean depth of the energy deposition in the j^{th} stack.

These two estimators exploited the ECAL capability for energy and spatial measurements to perform the particle identification in conjunction with Equation 3.4 (see Section 3.3).

The energy resolution was

$$\sigma(E)/E \approx \frac{18\%}{\sqrt{E(GeV)}} \oplus 0.9\%, \tag{3.9}$$

(where $\oplus$ means quadratically added) and the above–mentioned granularity gave a angular resolution of

$$\sigma_{\theta,\phi} \approx \frac{2.5}{\sqrt{E(GeV)}} \oplus 0.25(mrad) \tag{3.10}$$

3.2.6 The Magnet and Hadronic Calorimeter (HCAL)

The magnet system consisted of a fully instrumented iron yoke and a superconducting solenoid. The iron yoke (f in Figure 6.3) served three functions: closed the magnetic flux, supported most of the experimental subdetectors and was the absorber in the hadronic calorimeter (HCAL). It consisted of a central barrel and two end caps. It was 1.2 m thick in the radial direction and subdivided into layers for the insertion of plastic streamer tubes.

The superconducting solenoid (e in Figure 6.3) provided a uniform magnetic field of 1.5 T along the LEP beam direction. It was supported at both ends by the barrel part of the iron yoke and carried the weight of the ECAL and TPC.

HCAL was used in combination with the ECAL to measure the energy of neutral and charged hadrons produced in hadronic Z^0 decays.

Figure 3.9: *The magnet coil (during its transport to CERN).*

3.2.7 The Muon Chambers

At the periphery of the ALEPH detector (*g* in Figure 6.3) two layers of streamer tubes, called muon chambers, provided bi-dimensional information about particles which penetrated through the HCAL iron and were mostly muons. The digital information on individual strips in the HCAL was also used as a part of the muon detection.

3.2.8 The Trigger System

The triggering system of ALEPH served to initiate the recording of information as soon as an interesting event took place. The triggering was organized in a three-level trigger scheme to deal with the time between two beam crossings of the order of 22 μs.

The Level–1 trigger delivered a decision within 5 μs after a beam crossing. Its decision was based on charged track information from the ITC, as well as cluster energy information from ECAL and HCAL. Its purpose was to provide a preliminary decision whether the event should next use information from the TPC (see next paragraph), which would rendered the trigger system insensitive to further events during the aquisition time needed by the TPC, or whether it should be rejected, keeping the system active.

The Level–2 trigger used the TPC track information. Its decision was available within 50 μs after a beam crossing. In the case of a *no*, the data acquisition was stopped and reset, while a *yes* decision initiated the readout of the whole detector.

The Level–3 trigger decision was based on software processing information from all of the subdetectors. Its task was to reduce the amount of recorded data by eliminating background events before they were written to disk.

The trigger scheme was designed to work for Level–1 rates of about 50 Hz,

reduced to 10 Hz by Level–2 and 1 Hz by Level–3. But it was possible to set the subdetector trigger thresholds to values such that the interesting events caused a Level–1 trigger rate of a few Hz. In this case Level–2 and Level–3 triggers rejected only a small fraction of events.

Events flagged as interesting were written to disk and passed to the online displays in the ALEPH control room. The full event reconstruction was carried out after a "run" of about one hour duration was completed.

3.3 Particle Identification

The reconstruction of the events was performed in steps: reconstruction of particles, treatment of the energy deposits in the electromagnetic and hadronic calorimeter, and assignment of the energy deposit of the tracks and recognition of the different particles. This work was done with an ALEPH program package called JULIA.

The data collected between 1991 and 1995 around the Z^0 resonance were reprocessed during 1997–1998 using new and improved reconstruction algorithms. Special effort has been put in reconstructing the charged–particle information. The data presented in this analysis were passed through this reprocessing.

3.3.1 Charged Particles

Stable charged particles, i.e. charged particles with lifetimes longer than 10 ns, with average decay lengths which exceed the dimensions of the TPC, were identified by measuring the ionisation loss dE/dx. The reconstruction of the charged particle tracks started using three points in the TPC and fitting a helix through these points. Then further tracking points lying along the extrapolation of the helix were searched for. If no further points were found, this combination was rejected. Each time other points were found on the extrapolation, the parameters of the helix were reajusted.

Electrons were selected by the characteristic longitudinal and transverse development of their associated showers in ECAL. The dE/dx information provided by the TPC enhanced the hadron rejection power, while non-prompt electrons originating from photon conversions in the detector material were rejected based on their kinematic and geometric properties.

Muons were identified by their penetration pattern in HCAL. The additional three-dimensional coordinates measured in the two layers of external muon chambers helped in resolving the remaining possible ambiguities.

3.3.2 Neutral Particles

Photons and particles decaying to photons such as π^0s were measured with the ECAL. The neutral particles involved in the present analysis are these

neutral pions. Pairs of γs with a 4-momentum close to the π^0 invariant mass were assumed to be π^0.

Stable neutral particles are difficult to isolate and to measure in a multi-hadronic environment; they are seen as clusters in the hadron calorimeter.

3.3.3 Energy Flow

The simplest way to determine the total energy of an event recorded in the ALEPH detector might be to sum the raw energy found in all calorimetric cells (ECAL and HCAL) without performing any particle identification. For hadronic decays of the Z^0 this method gave a resolution a factor of two better than the one would obtain by using the ECAL or HCAL alone.

In order to increase the spatial and energy resolution, and to avoid double counting, an energy flow reconstruction algorithm [36] was developed making use of charged track measurements and taking advantage of the photon, electron and muon identification capabilities of the detector. The energy flow algorithm worked in two stages. In a first stage data were cleaned by rejecting false tracks which were due to noise, and in a second stage different subsystems were integrated and events were classified.

In the first stage tracks with at least four points in the TPC were selected and extrapolated to VDET and ITC. They had to be produced within a cylinder of radius of 2 cm and a length of 20 cm along the beam direction around the interaction point. If the tracks lay outside this cylinder a secondary vertex study was performed.

The second stage studied the deposits in the calorimeters. Correction for noise has been performed with the help of data from random triggers on bunch crossings containing no event. This permitted elimination of 98 % of the noise. Tracks which are reconstructed well were associated to the energy deposited in the electromagnetic and hadronic calorimeters. First electron identification was performed. If its energy deposit in the calorimeter exceeded that expected from the track momentum, a fraction of the deposited energy was associated to a neutral particle. The energy of objects identified as electrons, muons and photons were subtracted from the deposited energy. The remaining deposited energy was associated to a charged hadron, or to a neutral hadron, if no track was found.

The final piece of information was called an "energy flow object", and all such objects were assembled to describe the event that produced them.

The measured quantities were continuously compared to the ones simulated using Monte Carlo techniques. After generation, the events were processed through the detector simulation program to produce simulated raw data which were processed by the same reconstruction and analysis programs as used for the real data. The production of Monte Carlo simulated events is presented in the following chapter.

Chapter 4

The Monte Carlo Simulated Events

Monte Carlo (MC) simulations are numerical simulations of systems by making use of random numbers. The name "Monte Carlo" came because of the similarity of the statistical simulation to games of chance. Monte Carlo applications include e.g. econometrics, traffic flow, radiation–cancer therapy and elementary particle physics.

Event simulation in ALEPH is performed in two separate stages. In the first stage, the physical phenomena are generated independently of the detector. This is called the generator–level simulation, where the event properties are not distorted by detector effects. The second stage is produced by applying the detector simulation to the generator–level MC. This can then be treated in the same way as real data in order to understand the impact of the detection on the data.

The experimental data is then compared to the reconstructed Monte Carlo samples in order to search for new physics or to derive values for electroweak measurements. The original generator level information enables the user to know the exact physics of the Monte Carlo simulation.

In the following the MC methods are described in general terms, followed by the event generation and details of the detector simulation. The reconstruction software is then presented along with the final MC sample used.

4.1 Monte Carlo Events in ALEPH

A more general description of Monte Carlo methods is given in Appendix A. In this section one focuses on the ones used in simulating the events the present analysis is based on.

4.1.1 Event Generation

The colliding leptons, the electron and the positron, were theoretically mono–energetic and mono–directional, travelling down the z–axis and colliding at a given point. In modelling them one had to take into account that electrons traveled in bunches with fluctuating energy and their collision point was inside an ellipsoidal space within 8 cm of the interaction point along the beam direction, and 1.5 cm in the radial direction. This is usually not simulated by every of the experiment teams, but at the level of the team studying the LEP accelerator properties.

The generator used for the $e^+e^- \rightarrow Z \rightarrow q\overline{q}$ processes was PYTHIA 5.7 (The Lund Monte Carlo for High-P_T Physics) [37]. The inputs needed were:

- the coordinate frame of the experiment (colliding beams in the center of mass frame),
- the colliding particles (electron on positrons),
- the centre-of-mass energy ($\sqrt{s}$) and
- the minimum transverse momentum (p_t).

Also required were a random number generator and the gamma function.

The production of random numbers, which were generated by an algebraic algorithm, was in fact producing predictable, pseudo–random numbers. The random number generator RANMAR [41] was used. This was later adopted by the whole particle physics community, and incorporated in the CERN computing library package. The sequence of random numbers have been checked to ensure it was in the range 0 to 1, and that it was approximately uniformly distributed over its range. Successive pairs of numbers were checked to be statistically uncorrelated. It was used for particle physics event generation and a lot of care was taken to avoid generating the same events twice. To be sure that no duplication of events would be possible, a given convention has been defined for the initial seeds given to RANMAR to start the sequence.

The initial state particles were transformed to their centere-of-mass frame (for this case, the laboratory frame), and only then Z^0 production processes, subsequently decaying to quarks, were allowed. The quark q in the final state could be d, u, s, c or b, the flavor being random, according to the relative couplings implemented in the program. The simulation of initial (see Section 2.2) and final–state radiation (see Section 2.3) was included, because it can give large corrections to the overall topology of the events. This radiation is photon and/or gluon radiation, emitted because the process contained accelerated colored and/or charged objects in the initial, or final, state. The time period required to fully generate one event was approximately half a second.

Since no calculable theory exists for the hadronisation process (see Section 2.5), phenomenological models have been evolved, which fall into two broad classes: *string* fragmentation and *cluster* fragmentation. For this analysis, the hadronic decays of the Z^0 in ALEPH have been simulated using the JETSET

7.4 [37, 38] package. It is based on the string fragmentation model (see Section 2.5.1) and has adjustable parameters. These parameters can be fit to the observed data. The tuning of the parameters was specific for the ALEPH experiment, which are different from the default JETSET parameters.

The determination of model parameters was based on the comparison with measurable quantities such as:

- event–shape distributions (thrust, sphericity),
- charged particle inclusive momenta distributions (momenta, transverse momenta) and
- inclusive energy spectra for different mesons (η, ρ^0, etc).

The process of tuning involved an iterative comparison of data and Monte Carlo distributions [43]. Among the most important parameters tuned were (see Section 2.5.1)

- ξ_c and ξ_b, controlling the momenta of fragmentation particles from hadrons containing c and b hadrons,
- the shower cut–off, below which a parton is not allowed to radiate, and
- the scale Λ_{QCD}, defining the energy below which non–perturbative QCD has to be considered.

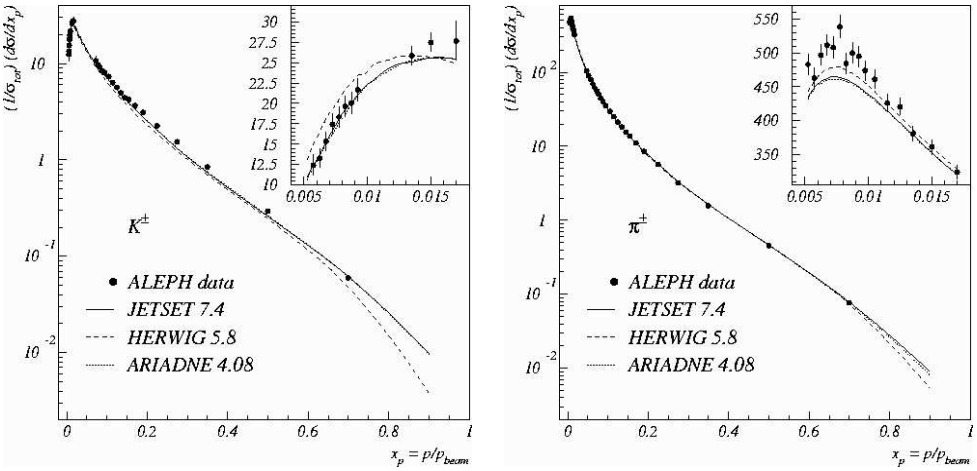

Figure 4.1: *ALEPH kaon and charged pion momentum distributions in data versus MC (p_{beam} =49 GeV) [43].*

Individual examples of the tuning are shown in the plots from Figure 4.1, where a good agreement in the differential cross sections from MC and data is found. Since the range of momenta of charged pions used in this analysis does not lie at the beginning of the $\pi^{\pm}$ spectrum, the discrepancy present there does not affect the present result. The present measurement of $BR(c \to l+X)$ is based on reconstructing charged kaons, as well as charged and neutral pions. For the π^0 spectrum the ALEPH measurements are also in agreement with the predictions of JETSET 7.4 (see Figure 4.2). However, the neutral pion data has not been used in the tuning of the MC parameters.

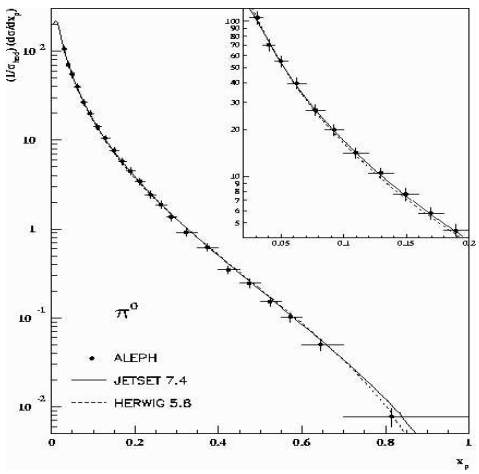

Figure 4.2: *ALEPH data versus MC simulated π^0 data [43]. Here p_{beam} =49 GeV.*

4.1.2 Detector Simulation and Event Reconstruction

The response of the ALEPH detector to physical processes had to be simulated in order to obtain MC events comparable to real data. Thus, the generator level events were passed through the ALEPH simulation program, called GALEPH. This made use of three programs: GEANT, GHEISHA and TPCSIM.

The GEANT package, version 3.15 [40], was used to simulate the passage of elementary particles through matter, taking into account the detector geometry. The parameters affecting the geometry included: shape (acceptance and thickness), complex material configurations (changes in radiation length) and gas/electrical parameters. In the tracking simulation, detector effects were simulated with a detailed 3–D model of the material and detector response.

Tracks of momenta p were followed through the detection system, in the magnetic field, and their direction was modified after traversing each layer of material of d radiation length thickness. This allowed for random multiple scattering by an angle θ, chosen from a Gaussian distribution. GEANT also permitted the simulation of phenomena due to other interactions, for example energy loss through ionisation and decays of particles using MC techniques. Furthermore, electromagnetic interactions, such as bremsstrahlung, were described. Noise and smearing effects were also considered, the particle position produced by each detector being modified in the range of the detectors resolutions.

The electromagnetic interaction with the material of the calorimeter and the hadronic showers were simulated using the shape of showers depending on parameters such as: deposited energy, particle momentum, type of incident particle, number of secondary particles and detector area (active or dead area).

The TPCSIM package performed the TPC digitisation. This included sim-

ulation of the ionisation energy loss, drift time, electron diffusion, avalanche formation and detection (with appropriate smearing and noise).

After full detector simulation the results were passed through the same reconstruction program (JULIA) as the real data. This provided fully reconstructed simulated data. The reconstruction steps were the following:

- reconstruction of the charged tracks,
- treatment of the dE/dx information from the TPC,
- reconstruction of the primary vertex,
- clustering of the energy deposited in the calorimeters,
- energy flow analysis,
- particle identification.

Therefore, two sets of information were available to represent the simulated data. The first set was the generator level (truth) Monte Carlo, with no detector or reconstruction inefficiencies to distort the information. The second set was the reconstructed Monte Carlo, which was the generator level events passed through detector simulation and reconstruction. This latter type of Monte Carlo ought to represent the real data.

The connection between the reconstructed track and MC truth track, was performed via an ALPHA routine, which established the best match based on the number of shared hits between the MC truth and MC reconstructed track. If there was more than one matching candidate in the MC truth database, the charged track with the larger number of shared hits was taken.

For this analysis, not only the reconstruction of the final particles was important, but also of their D meson mothers. The charged tracks used were kaons and pions. Their momenta were determined by measuring their curvature in the magnetic field. The complete set of measured coordinates of the tracks are MC simulated and used to extract the momentum. In Figure 4.3 one can see a reasonably good agreement between the estimated momentum and the known input value, where the arrows show the cuts applied on the respective momenta in this analysis. The figures show that the ALEPH detector loses information in a very minor way, and the shape of the momentum distribution is preserved in the reconstruction, according to the MC simulation of the detector. In other words, the good agreement from Figures 4.3 indicates that the design of the ALEPH detector was successful, and that the knowledge of the detector is very good.

The detector simulation was also important in order to track the influence of any mis–aligned parts of the detector system. Because of running at the Z^0 peak, the calibration of the detector was continuously checked. This is in contrast to later periods, when LEP was running at higher energies. There were dedicated periods, at the beginning of the data–taking periods, to check the calibration of the detector by running at the Z^0 center–of–mass energy.

The reconstruction of a decaying D particle involves the reconstruction of its 4–momentum. All the tracks are, by default, assumed to have the pion mass. For the particular case of kaons, their mass had to be assigned in

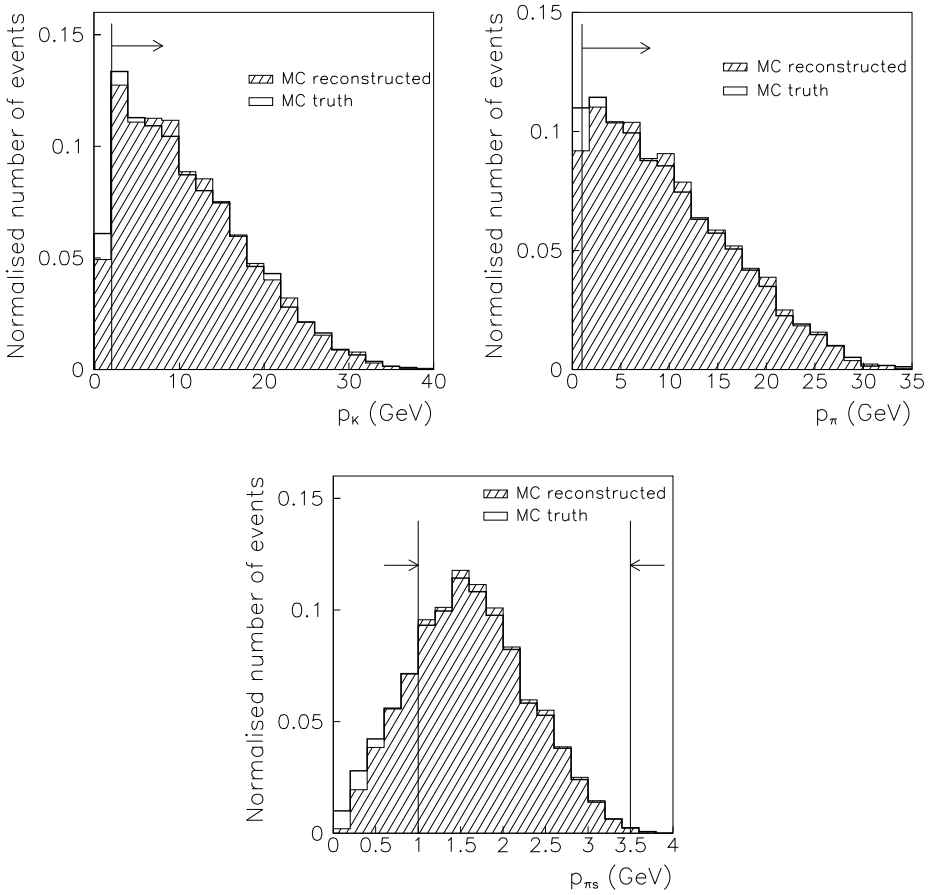

Figure 4.3: *Kaons, pions and soft pions momenta in MC, at the truth and at the reconstructed level. The arrows indicate applied cuts.*

order to compute the energy based on their 3–momentum. After this stage, two possibilities were available in order to compute the mass of the decaying particle:

- to add the reconstructed 4–momenta of the decay products, obtaining m_{rec}
- to perform a D vertex fit, obtaining m_{fit}.

In the first case, to reconstruct the momenta of the decay products, both for real data or MC data, one considers all configurations of the momentum vectors of the D particle and chooses the one which is closest in least–squares value to the observed sets of hits. In the second case, one associates a track to the D meson, characterised by a fitted momentum which can slightly differ from the sum of the decay products of the reconstructed 4–momenta. One obtains improved (over the first class) estimates of the momenta, because of extra information of energy and momentum conservation, and because extra constraints regarding the interaction region.

As observed in Figure 4.4, the masses obtained with the two methods can be seen to be compatible. During this analysis, the mass of the D mesons

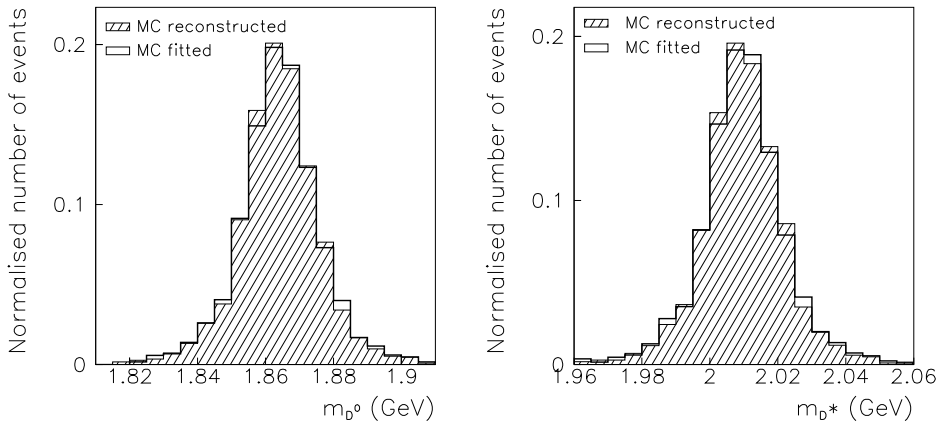

Figure 4.4: *Masses of D^0 and D^* mesons, directly reconstructed and as resulting from the D^0 and D^* mesons fitting*

obtained from D vertex fitting was used. As seen in Figure 4.4, the reconstruction of the particle momenta worked very well in ALEPH. The particle momenta of the D mesons (D^{*+}, D^0 or D^+), the kaon and the soft pion were used as inputs for the NN (described in Chapter 6).

4.2 MC–Data Consistency Checks

The distinction between the c sigmal and the uds/b background made by the NNs is based on 11 variables (see Section 7.2). Their influences are not clearly separated. However, as one can see in Figures 4.5 to 4.10, all the different variables used by the NN have similar behavior for data and MC. Therefore, all the numbers used by the NN are assumed to be correctly simulated by the Monte Carlo.

As a consequence, the outputs from the NN also have similar behaviour for data and MC (see Figure 4.11).

Because the final cuts are made in the mass spectra of the D meson candidates, the good agreement between data and MC regarding the D mass spectra (see Figures 4.12) plays an important role.

One can conclude that a very good agreement exist between real and MC simulated data samples. The MC simulation is, therefore, reliable, and the data extracted from it reflects the reality.

4.3 The MC Dataset Used

The Monte Carlo sample used in this analysis consisted of 11,033,000 $Class$ 16 events (see Section 5.3), representing the sum of 8,685,000 $q\overline{q}$ and 2,348,000 $c\overline{c}$ events (see Table 4.1). The amounts generated for each year was dependent on the number of real data events available for that year.

Year	1991	1992	1993	1994	1995	Total
Data	238	629	670	1672	721	3930
$q\overline{q}$ MC	487	1549	1342	3443	771	8685
$c\overline{c}$ MC	146	390	604	771	437	2348

Table 4.1: *Monte Carlo events available in ALEPH for this analysis. The numbers represent thousands of Class* 16 *events*

The Heavy Flavor group of ALEPH was focused on studying the properties of the heavy quarks produced at LEP: the charm, c, and the bottom, b, quarks. It used MC events were subdivided into four classes:

- $q\overline{q}$ events: This sample was approximatively twice as large as the $q\overline{q}$ real data sample. Here, one attempted to generate the $q\overline{q}$ events in the same proportion, and with the same decay modes, as in reality.
- $c\overline{c}$ events: This sample consisted of charm quarks only, $q = c$ (the other types of quarks being neglected).
- $b\overline{b}$ events: This sample consisted of bottom quarks only, $q = b$.
- $B_s \to l\nu X$: This sample involved only those Z^0 decays where a B_s was produced, which subsequently decayed to a lepton.

These four classes were independently generated samples of events. The number of events of the last two classes are not shown in Table 4.1, because they

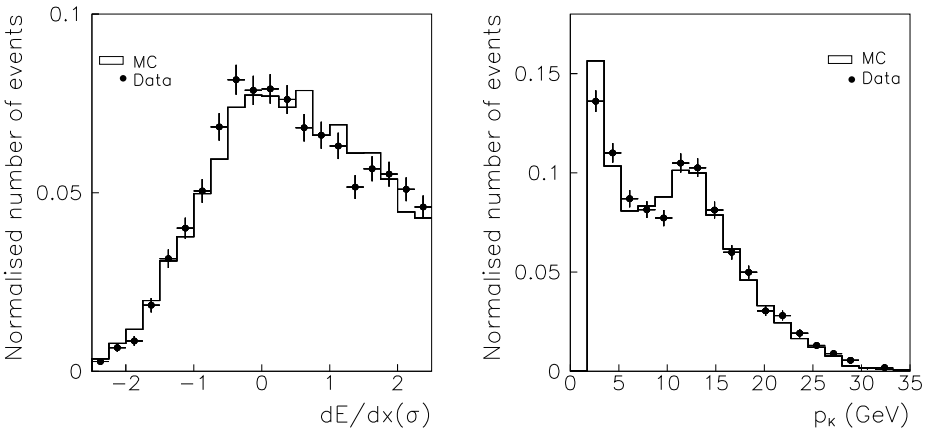

Figure 4.5: *The relative energy loss for the final decay products tracks and the momenta of the kaon candidates, in MC and data*

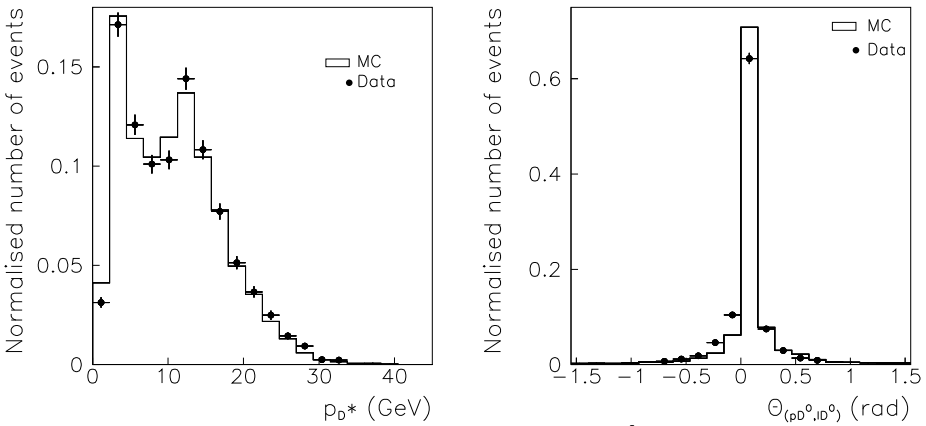

Figure 4.6: *D^* momenta and the angles between the D^0 momentum and the direction of the track of the D^0 candidate, in MC and data*

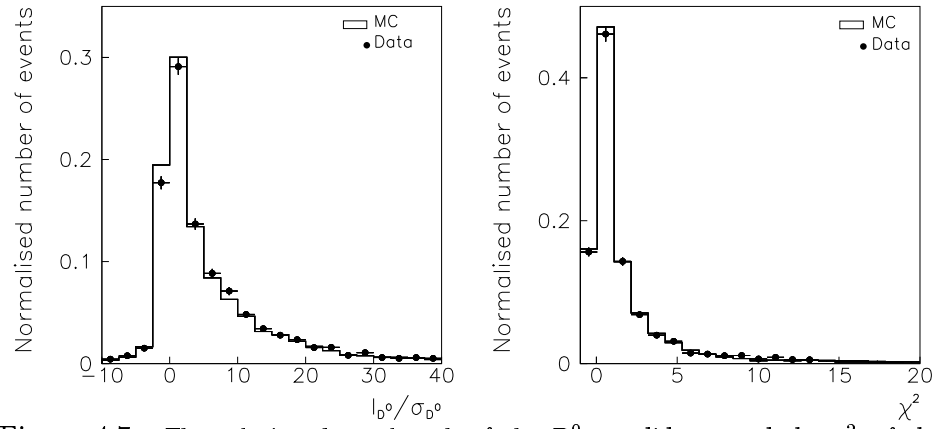

Figure 4.7: *The relative decay length of the D^0 candidates and the χ^2 of the D vertex fit, in MC and data*

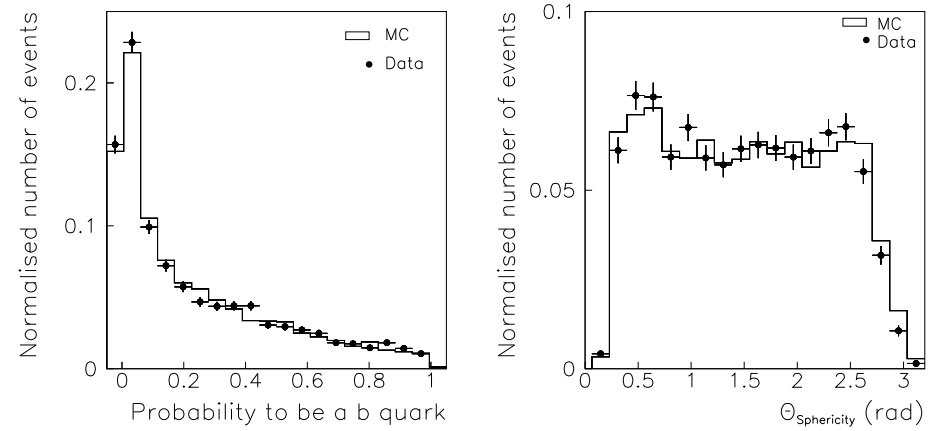

Figure 4.8: *The probability of the charmed quark candidate to come from a b quark and the value of the sphericity angle (see Section 7.2) of the event, in MC and data.*

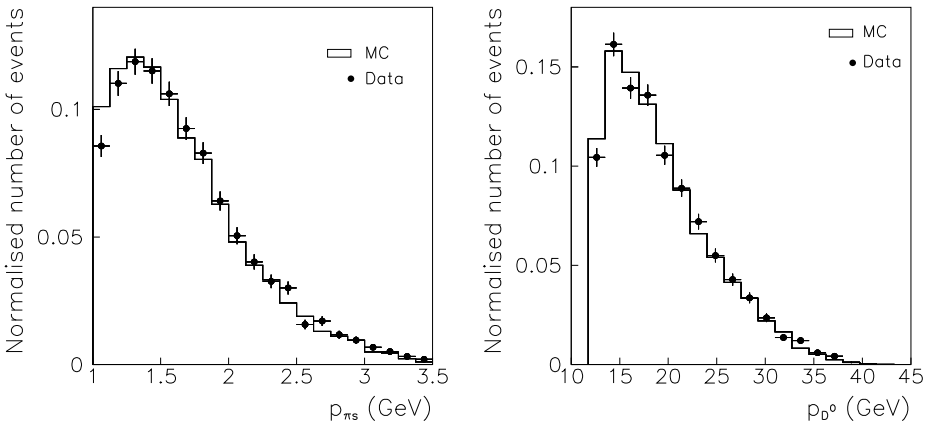

Figure 4.9: *Momenta of the soft pion and the D^0, and the difference between the reconstructed masses of D^* and D^0, in MC and data*

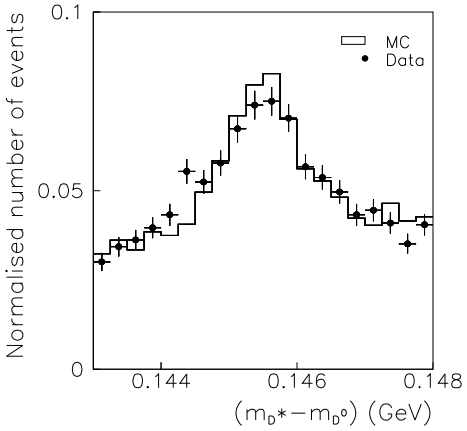

Figure 4.10: *The difference between the reconstructed masses of D^* and D^0, in MC and data*

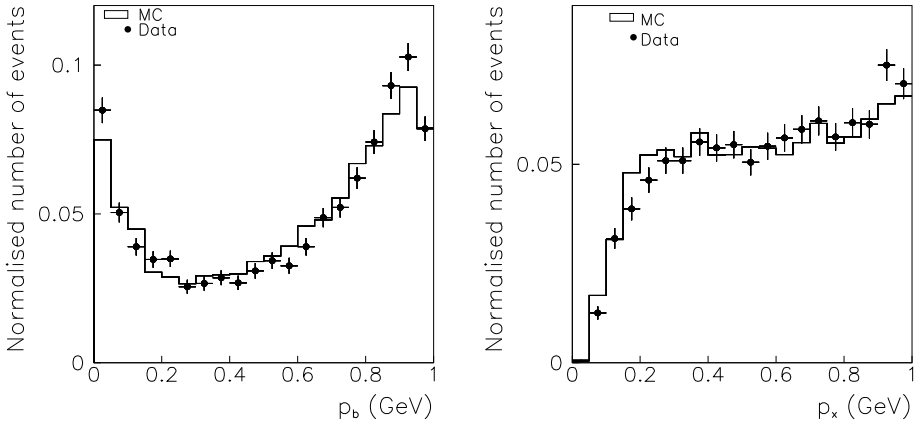

Figure 4.11: *The NN outputs.*

were not used in the present analysis.

The number of the generated events was limited by the computational

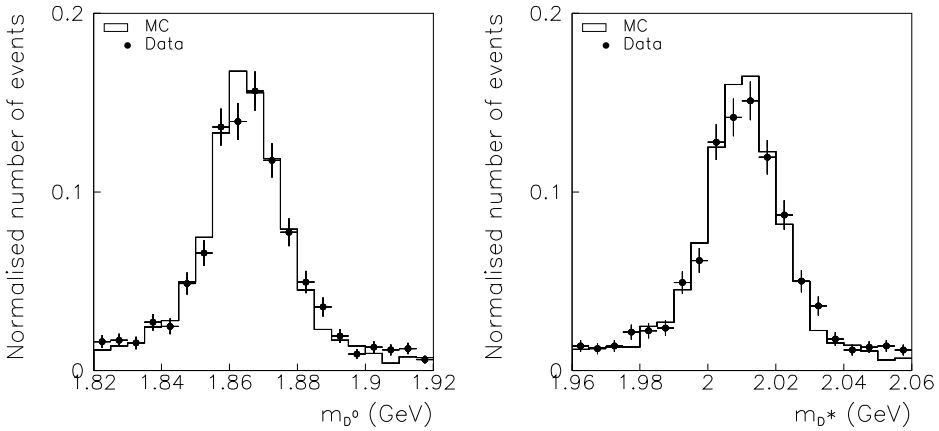

Figure 4.12: *The D meson candidates mass peaks*

power available at the time. Also, in order to simulate particular types of events with a higher level of accuracy, dedicated MC samples of events were generated, as shown in table 4.1. In this analysis, the $c\overline{c}$ dedicated MC was used for the NN training, to extract the properties accompanying the presence of a charm signal. This is described in Section 6.4.

One can conclude that the particles spectra, on which the present branching ratio study is based, are correctly reproduced by the MC.

Chapter 5

Analysis Principle and Initial Dataset

The purpose of this analysis is to compute the fraction of charm quarks decaying via a lepton. Firstly the analysis method is presented and the different sources of background are explained. This is followed by a description of initial data and Monte Carlo samples and the preselection routines.

5.1 Method

An ALEPH internal feasibility study has been performed for this analysis [48] and shown that this measurement can be done. The method used relies on counting two quantities: how many charm quarks have been produced (see Chapter 7) and how many of them decayed via a lepton (see Chapter 8). The searching procedure is shown in Figure 5.1.

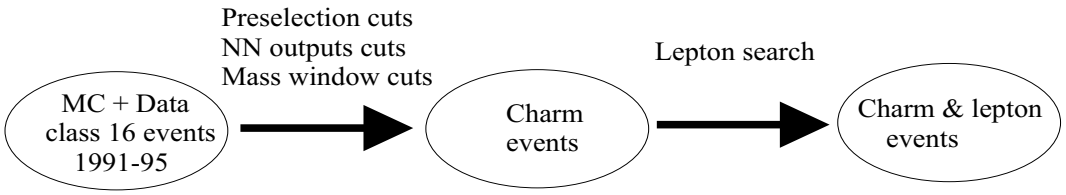

Figure 5.1: *Schematic view of the searching procedure*

One begins the event selection by calculating, for each event, the thrust axis. This is defined as the direction, $\vec{e}$, which maximizes the sum of the longitudinal components of all the detected particle momenta $\vec{p_i}$:

$$\max \sum_i |\vec{e} \cdot \vec{p_i}| \tag{5.1}$$

The charm quark has to be identified in a way that is independent of its decay modes. When a charm quark c was produced, due to $Z^0 \to c\overline{c}$, it was not produced alone but in pairs with its anti-particle, $\overline{c}$. The two quarks were

Meson	D^0	$\overline{D^0}$	$D^{\star+}$	$D^{\star-}$	D^+	D^-
Charm content	$c\overline{u}$	$\overline{c}u$	$c\overline{d}$	$\overline{c}d$	$c\overline{d}$	$\overline{c}d$

Table 5.1: *Charm quark content of the D-candidates*

produced back to back in the Z^0 rest frame, which roughly corresponds to the direction of the thrust axis. By dividing the event into two hemispheres, using a plane perpendicular to the thrust axis, one charm quark was placed in one hemisphere and its anti-particle was placed in the second hemisphere.

The particles searched for in this analysis are D mesons which contain a charm quark. The charm selection is based on D^0, D^+ and $D^{\star+}$ decay modes (together with their anti-particles, $\overline{D}^0$, D^- and D^{*-}), the charm content of which is given in table 5.1.

The decay channels chosen have high production branching ratios and are easily reconstructed by ALEPH. They are:

Channel			Channel number
$D^{\star+}$	$\rightarrow$	$D^0\,\pi_s^+$	
		$\hookrightarrow K^-\,\pi^+$	(a)
		$\hookrightarrow K^-\,\pi^+\,\pi^0$	(b)
		$\hookrightarrow K^-\,\pi^+\,\pi^-\pi^+$	(c)
D^0	$\rightarrow$	$K^-\,\pi^+$	(d)
D^+	$\rightarrow$	$K^-\,\pi^+\,\pi^+$	(e)

Table 5.2: *Channels of D decays which are used by the present analysis*

The first three of the channels in Table 5.2 ((a) to (c)) are based on the decay of D^{*+} via a D^0 and a pion with a low momentum in the D^{*+} reference frame, π_s. The presence of π_s, along with the D^0 candidate, improves the quality of the signal when reconstructing the D^0 channels. The $D^0 \rightarrow K^-\pi^+$ decay has the cleanest signature, in comparison to all the other decay possibilities. Because of this reason, it has been chosen to be reconstructed alone, in channel (d), without the help of the additional π_s.

To improve the c–event statistics, two other decay channels can be used (see Table 5.3). In both of channels (f) and (g) one particle escapes detection. In channel (f) the particle that escapes is a π^0. In channel (g) the neutrino ν_l, associated to the lepton l ($l =$ electron or muon), could not be detected. Even if the mass of the D mesons, therefore, is not a good discriminating variable between signal and background, the mass difference $m_{D^{\star+}} - m_{D^0}$ is

Channel			Channel number
$D^{\star+}$	$\rightarrow$	$D^0\,\pi_s^+$	
		$\hookrightarrow K^-\,\pi^+\,(\pi^0)$	(f)
		$\hookrightarrow K^-\,l^+\nu_l$	(g)

Table 5.3: *Channels of D decays which might be further used for this analysis*

only weakly affected. This is because one particle is missing both from the $D^{\star+}$ and the D^0 reconstruction, such that $m_{D^{\star+}} - m_{D^0}$ continues to peak at low values in the case of signal events. These two channels ((f) and (g)) needed a different fitting procedure than channels (a) to (e), and were not used by the present analysis.

Once a D meson had been found in one of the two hemispheres it also means that a partner charm quark had been produced in the other hemisphere. The total number of events where a D meson has been found is denoted as N_D^c. The number of selected events where a D meson together with a lepton in the opposite hemisphere is denoted $N_{D,l}^c$. These are the events where the charm quark decayed into a lepton. A sketch of the searching procedure is shown in Figure 5.2.

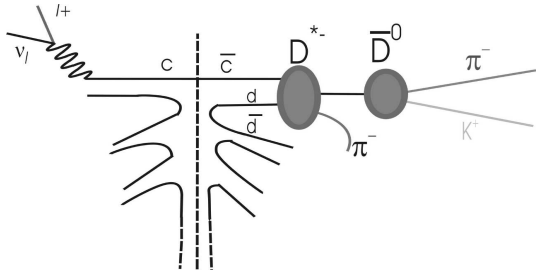

Figure 5.2: *Schematic view of an event containing a D^0 and a lepton*

A more realistic view of how a charm event looked in the ALEPH detector is presented in Figure 5.3. Here a $\overline{D}^0$ meson is identified from a π^- and a K^+ track.

If the efficiency $\varepsilon_{c\rightarrow l}$ for identifying a lepton from a $c \rightarrow l$ decay, opposite to a charm candidate, is known, the $BR(c \rightarrow l + X)$ can be extracted as follows:

$$BR(c \rightarrow l + X) \quad = \quad \frac{1}{\varepsilon_{c\rightarrow l}} \cdot \frac{N_{D,l}^c}{N_D^c} \tag{5.2}$$

Therefore, an advantage of this method is its independence of the D-detection efficiency ε_D, as this parameter drops out in the ratio $N_{D,l}^c/N_D^c$. The method by which the N_D^c and $N_{D,l}^c$ numbers were measured is described in Section 5.2, and in Chapters 7 and 8.

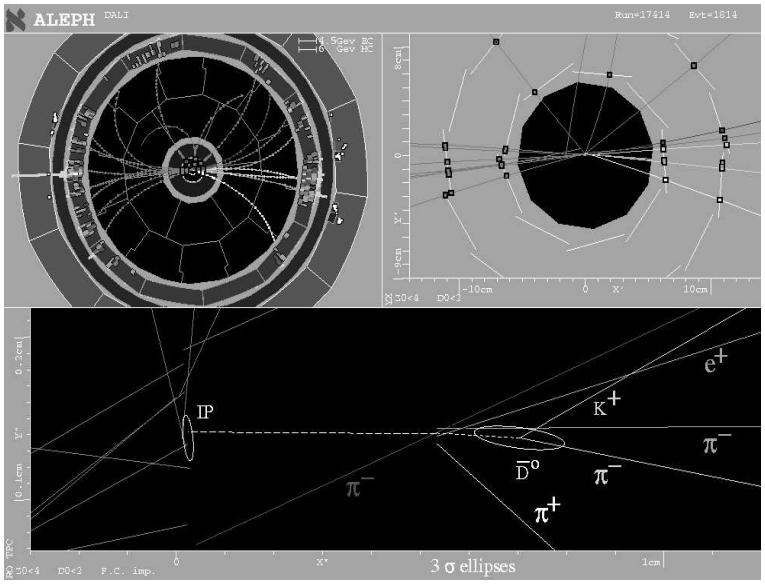

Figure 5.3: *D^0 event, as viewed by the ALEPH detector. Here the D^0 candidate is identified by a π^-– and a K^+–track.*

The efficiency $\varepsilon_{c\to l}$ was calculated using the Monte Carlo data. A branching ratio of $BR_{MC} = 0.102$, close to the previous experimentally determined values for $BR(c \to l + X)$ [9], was implemented in the MC event generator (PYTHIA). MC simulated data were universal for all the ALEPH investigations, where the number of leptons due to charm decays was needed. However, the implemented value of BR had no importance for this particular analysis, because a correction to $BR(c \to l + X)$ is performed. Using equation (5.2):

$$\varepsilon_{c\to l\,MC} = \frac{N^c_{D,l|MC}}{N_{D^c|MC}} \cdot \frac{1}{BR(c \to l + X)_{MC}} \tag{5.3}$$

Assuming that the efficiency is correctly modeled in the MC, such that one can assume $\varepsilon_{c\to l} = \varepsilon_{c\to l\,MC}$, one finds:

$$BR(c \to l + X) = \frac{N^c_{D,l}}{N^c_D} \cdot \frac{N^c_{D|MC}}{N^c_{D,l|MC}} \cdot BR(c \to l + X)_{MC} \tag{5.4}$$

A branching ratio can then be computed for each of the five channels (a)–(e), listed in Section 5.1. The final $BR(c \to l + X)$ is a result of combining these five branching ratios, weighted based on the estimated errors one obtains in each of the channels, and taking correlations into account (see Section 9.4).

5.2 Background Reduction

In this study one is interested in D meson candidates from the direct $Z^0 \to c\bar{c}$ decays, N^c_D. However, a D meson could also have been produced from a

cascade decay, for example $Z^0 \to b\bar{b}$ followed by a decay of one of the b quarks $b \to c$. For this measurement D mesons from cascade decays were considered background. These D mesons were, in both cases, *true* ones, denoted by the D subscript in (5.5).

There was also combinatorial background, where one reconstructed *fake* D candidates from events originating from initial quarks with all the possible flavours (c, b or u, d, s). The fake D candidates were random combinations of π and K mesons, or even particles wrongly identified as π and K, which passed the cuts selecting D candidates. These fake D mesons are denoted by the subscript F in (5.5).

Following this, the number of hemispheres N_h, containing a charm candidate, can be decomposed as follows:

$$N_h \quad = \quad N_D^c + N_D^b + N_F^c + N_F^b + N_F^{uds} \tag{5.5}$$

Leptons were searched for in the hemisphere opposite to the one where a D meson candidate had been found. These leptons could be either true leptons, denoted by the subscript l in (5.6), or fake or true non-prompt leptons. The latter two are denoted by the subscript f in (5.6). A *prompt* lepton is a lepton arising directly from the charm-quark and not from an intermediate decay. The number of events $N_{h,L}$, with a $c \to D$ candidate in one hemisphere, and a lepton candidate L, in the opposite hemisphere, can be written as the sum of all the possible combinations of true(D)/fake(F) D mesons and true(l)/fake(f) lepton candidates:

$$N_{h,L} \quad = \quad N_{D,l}^c + N_{D,f}^c + N_{D,l}^b + N_{D,f}^b + N_{F,l}^c + N_{F,l}^b + N_{F,f}^{c,b,uds} \tag{5.6}$$

As suggested in the feasibility study [48], the selection of D candidates with high charm purity with respect to the charm efficiency was performed in the present analysis using Neural Net (NN) (see Chapter 6). This has been shown to provide a substantial improvement in the number of selected charm events, while maintaining comparable sample purity. The variables used to train the NN differed slightly between the charm signal and the uds- or b-background, as simulated in the Monte Carlo data. The NN were trained so that the output lay close to 1 for signal and 0 for background. By cutting on the output at high values, close to 1, one was confident of obtaining a high charm purity of the selected events. An additional cut was performed in the mass of the detected D^0 meson, for channels (a) to (d), or of the D^+ meson, for case (e). The selection is discussed in detail in Chapter 7 along with the estimate of the signal purity.

The lepton identification was performed separately for both electrons and muons. It is presented in Chapter 8, along with the estimate of the composition of the $N_{h,L}$ sample.

5.3 Data Samples

This work analysed hadronic events, so-called *Class 16* events, which have been preselected to be used in different analysis by ALEPH. Therefore, these type of events have been already extracted from the total data sample, to form a *Class 16* data set and a *Class 16* Monte Carlo data set.

The $q\overline{q}$ events that are defined as *Class 16* have the following features:

- At least 5 TPC tracks satisfying the following cuts:
  - The distance from the interaction point along the z axis, z_0, and the radial distance, d_0, must satisfy $|z_0| < 10\,\text{cm}$ and $|d_0| < 2\,\text{cm}$. This is to ensure reconstructed tracks originate from the interaction point.
  - At least 4 TPC coordinates per track to ensure that the track curvature can be accurately determined.
  - The angle θ with respect to the beam direction (the z direction) should satisfy $|\cos\theta| < 0.95$. This is to ensure good event containment in the detector, such that one has a complete number of particles, and, therefore, a complete event reconstruction.
- The total energy $E(\textit{charged track})$ of all TPC tracks satisfying the cuts above should be larger than 10% of the center of mass energy $\sqrt{s}$, $E(\textit{charged track}) \geq 0.1\sqrt{s}$. This suppressed the $\gamma\gamma$ events, present in an amount comparable to the one of *Class 16* events.

However, the $\gamma\gamma$ events may affect the measurement of $BR(c \to l + X)$ due to charm quarks produced in a collision of two photons. But because this sort of c quarks have low energy they are, therefore, not selected in the present analysis, based on detecting high energetic D mesons.

On and near the Z^0 resonance the ALEPH detector collected data from 1990 until 1995. This analysis uses only data collected from 1991 until 1995, since the VDET was installed in 1991 only and good primary and secondary vertex reconstructions became possible. A basic classification of the data by the trigger was the separation of the purely leptonic events, $Z^0 \to l^+l^-$, from the others, based on the multiplicity of the charged tracks. One was then left with $3,961,651$ hadronic events, which is the sample the present study is based on. Out of these events most of the $\gamma\gamma$ background has been already rejected by the *Class 16* cuts.

In order to derive the final results, for each year Monte Carlo samples were generated. The Monte Carlo samples used by this analysis consisted of 8.6 million $Z^0 \to q\overline{q}$ plus 2.35 million dedicated $Z^0 \to c\overline{c}$ events, as described in Chapter 4.

5.4 Preselection

In order to improve the quality of the analysed event sample preselection cuts are used in the data and Monte Carlo samples to reject events which are not

of interest in this analysis.

To ensure that one has VDET hits for tracks, and, therefore, a precise secondary vertex reconstruction, the angle θ between the event thrust axis (5.1) and the beam direction is constrained to be:

$$1. \quad |\cos\theta| \quad < \quad 0.7$$

Cuts based on the energy loss of charged particles were also applied in order to identify kaons and pions. To verify if a track of a charged particle came from a certain type of particle, one assigned the mass m_T of that type of particle (m_K, m_π) and extracted the corresponding average energy loss $\langle dE/dx(T,p)\rangle$ and standard deviation of the energy loss $\sigma(T,p)$. The ionisation loss of the particle, measured by the TPC, was compared to the expected distribution of the ionisation loss for the mass m_T. In this analysis a mass m_T was assigned to a track of a particle if, for the momentum p of the track, its differential mean energy loss $dE/dx(T,p)$ was within 2.5σ of the expected mean distribution, as shown in Figure 3.8:

$$2. \quad \frac{|dE/dx(m) - \langle dE/dx(T,p)\rangle|}{\sigma(T,p)} \quad < \quad 2.5$$

If the particle satisfied the above condition it was assigned an identity of type T.

In order that the D^0 and D^+ vertices could be accurately reconstructed, the decay particles of a D meson candidate had to produce at least 2 tracks with at least 2 vertex-detector hits each:

$$3. \quad N_{VDEThits} \geq 2$$

The charm flavoured D mesons were reconstructed from K and π candidates via their decays in 5 channels, (a) – (e) (see Section 5.1). At this point of the analysis some of the events could have been classified in more than one channel.

The next preselection cuts, based on the invariant mass of the reconstructed D mesons, were applied in order to lower the uncertainty on the K and π identification. For these cuts a distinction between two main classes of events is done:

- (I) Two D mesons are reconstructed per event: a D^* meson and a subsequent D^0, together with a soft pion π_s (channels (a) – (c))
- (II) Only one D meson (either a D^+, or a D^0) is reconstructed (channels (d) and (e)).

Class I cuts:

In this first class of decays (channels (a), (b) and (c)), the assigned kaon, K, or pion, π, should have momentum satisfying:

$$4.I. \quad p_K > 2\ GeV \quad , \quad p_\pi > 0.4\ GeV$$

The condition that a track can be associated to a low momentum π_s and the conditions related to the m_{D^*} and m_{D^0} invariant masses of the D candidates are:

$$5.I. \quad \left\{ \begin{array}{lccccc} 1. & 1\ GeV & < & p_{\pi_s} & < & 3.5\ GeV \\ 2.a. & M_{D^0} - 0.5\ GeV & < & m_{D^0} & < & M_{D^0} + 0.5\ GeV \\ 3.a. & 0.143\ GeV & < & m_{D^*} - m_{D^0} & < & 0.148\ GeV \end{array} \right.$$

where $M_{D^0} = 1.864\,\mathrm{GeV}$ is the MC-implemented D^0 mass reference.

The case where a π^0 is reconstructed (channel (b)) as one of the D^0 (and therefore the D^*) meson decay products, the D mesons invariant mass resolution becomes worse than in the other cases. This is because the resolution in reconstructing the π^0 from two photons is worse than the resolution for reconstructing a K or a $\pi^\pm$, and because of the influence on the errors in reconstructing the angle between the two γ. Therefore, in this case, the last two conditions above, $5.I.2.a$ and $5.I.3.a$, are relaxed, such that the m_{D^*} and m_{D^0} invariant masses of the D candidates have to satisfy:

$$5.I. \quad \left\{ \begin{array}{lccccc} 2.b. & 1.0\ GeV & < & m_{D^0} & < & 2.5\ GeV \\ 3.b. & 1.5\ GeV & < & m_{D^*} & < & 3.0\ GeV \end{array} \right.$$

Class II cuts:

For the second class of decays, channels (d) and (e), when only one D meson candidate is reconstructed, the minimum momenta allowed for a charged track to be assigned as a kaon K or as a pion π are changed to:

$$4.II. \quad p_K > 1\ GeV \quad , \quad p_\pi > 1\ GeV$$

while the mass conditions regarding the D candidates are, for channel (d),

$$5.II.a. \quad 1.54\ GeV < m_{D^0} < 2.19\ GeV$$

and, for the decay channel (e),

$$5.II.b. \quad 1.0\ GeV < m_{D^+} < 2.5\ GeV$$

The events which belong to either channel were retained at this stage of the analysis in all the channels. The events which did not belong to any channel were discarded from the sample.

5.5 Selection of the Charm Events

The event selection occurs event by event by searching through the tracks of charged particles which passed the preselection cuts described above. The tracks are assigned as a kaon or a pion, in all possible combinations which are allowed with respect to the decay channel. Therefore, if a charged track fulfills the cuts 1 to 5 for being assigned both as a pion and a kaon, both possibilities are considered for further analysis.

The algorithm for the $D^0, D^+, D^{\star+}$ search is applied independently to each hemispheres, separated by the plane perpendicular to the thrust axis (see Equation 5.1). An event could pass the cuts for more than one decay channel and, therefore, be present in multiple channels as a candidate. The analysis proceeds further and the event is uniquely assigned to one of the channels at the end, based on the Neural Nets (NN) outputs.

The final selection of events containing D candidates made use of two NN which ranked them in order to discriminate between c/uds and c/b decays. They were trained to distinguish the signal from background for each of the channels. However, the NN were used to choose only one candidate per event. When one event passed the conditions to belong to more than one channel, all these channels were presented to the NN. For each combination of tracks the NN provided two discriminants, p_{uds} and p_b, for the event not to be assigned to a *u, d, s* or to a *b* initial quark, but to a *c* quark. The candidate chosen was the one which had the greatest sum $p_{uds} + p_b$.

At the end of the event selection one was left with events which may have initially been compatible with more than one channel, but which now are assigned to an unique channel.

5.6 Selection of the Charm Events Leptonically Decaying

The event selection searches through the events containing a D meson candidate to identify those also containing a lepton candidate. The two candidates, the meson and the lepton, are searched for in opposite hemispheres.

The number of selected events containing charm quarks leptonically decaying is not heavily dependent on the MC simulation. It is approximately equal to the difference between the number of lepton candidates having a charge opposite to the charge of the D meson candidate and the ones having the same charge as the D meson candidate. This number is corrected based on the MC simulated data to get eliminate this approximation. This correction implies a detailed analysis of the leptonic sample, in relation with the analysis of the D meson sample (see Section 8.4). Then, numbers extracted from the MC are extrapolated to the data.

Chapter 6

The Neuronal Nets

The imitation of the brain's data processing architecture in computing science (Neuronal Network [49]) has been mainly driven by the hope to find solutions to problems where conventional algorithms failed or to analyse complex situations, for example visual pattern recognition and remote coordination. These networks are large collections of interacting entities with emergent properties. They are systems which can design themselves with relatively little external guidance.

When experimental data is analysed in high energy physics the standard procedure is to make various cuts in the N-dimensional space of observed kinematic variables, $\{n_k\}_{k=1..N}$, in order to single out desired features. But high energy physics data analyses often imply non-linear modeling problems, where the use of linear cuts (selection of a rectangular N-dimensional shape) is inadequate. For such cases Neuronal Nets (NN) can be powerful tools, allowing the selected region of interest to have a more complicate shape - usually difficult to parameterize.

In the following a short introduction to neural networks in biology is given along with a discussion of the theory of NN's in computing. The NN were used in this analysis to distinguish between signal and background. In the end of this chapter the NN implementation and the adjustment of its parameters are explained.

6.1 Analogy to Biological Neural Networks

The theory of neural networks in modern computing is closely related to the level of understanding of neurology - a branch of biology studying the reaction mechanism of nerves. An analogy can be made with the connections between different units of a NN in computing and the synapses between different neurons in the brain. Inside the brain information of different types are processed and a reaction to them is found. Finding the adequate reaction can not be obtained from the first attempt, but needs a number of iterations. The brain-procedure of iterating the incoming information, in order to find

the adequate reaction, is called learning.

The human brain is a biological neural network containing approximately 10^{11} neurons. It is governed by electrical impulses between the parts found at different electrical potential. The neurons are knots, where the sum over the incoming signals from synapses produces chemical processes and induces an electrical potential difference. Once the sum over the signals is higher than a certain level (the activation level), the summed signal is sent over the outgoing synapses to the next neurons.

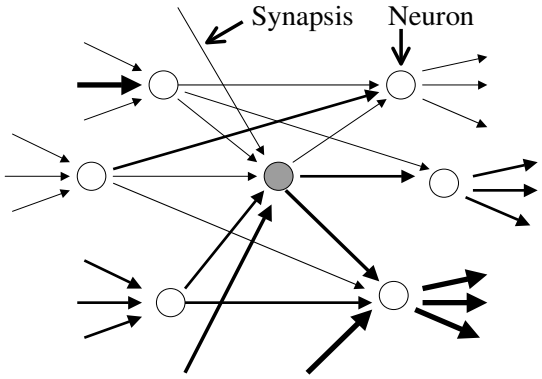

Figure 6.1: *A schematic view of neurons and synapses in biology*

The synapses themselves each have a given weight, which can be compared to the resistivity parameter in electronics. Furthermore, the brain adapts itself permanently to the external world, by changing the architecture of the inter-neuron connections.

In a first approach, the brain can be considered as a large collection of interacting entities with emergent properties, a system which can design itself with relatively little external guidance. From the previous simplified model of the human brain, one can see that the learning process is a permanent readjustment of various parameters, for example: the activation level inside the neurons, the weight of each incoming synapse and the architecture of the outgoing connections to the next neurons.

6.2 Multilayer Perceptron

The adjective *neural* is used because much of the inspiration for neural networks comes from neuroscience, where one neuron is literally connected, if not directly, with all the other neurons. But in order to software-implement the above basic description of biological neuronal network architectures, one has to proceed with some simplifications. The number of neurons and the number of synapses have to be reduced, taking into account the level of complexity of the given problem and the memory and power of the available computer.

There is a large variety of neuronal networks used in computer science. However, the following description limits itself at describing the multilayer-perceptron combined with a learning algorithm (see Section 6.2.3) called Resilient Propagation (RPROP). This is the one used to build the NN used for this analysis purpose.

6.2.1 Architecture and Mathematical Description

The multilayer perceptron network (Figure 6.2) consists of consecutive k layers of neurons, $n_i^{(k)}$, each of them in a state $n_i(t)$ at a given time t. The left most layer in Figure 6.2, $n_i^{(0)}$, represents the layer containing the input neurons, where the external information is fed in. After having treated the information, the input neurons send their signals to the next layer, $n_j^{(1)}$, which performs the same procedure. The last layer is the output layer and it gives the response of the system. The intermediate layers between the input and the output layer, which are not visible to the final user, are often called hidden layers. In Figure 6.2 a NN architecture identical to the one used in this analysis – with only one hidden layer – is presented.

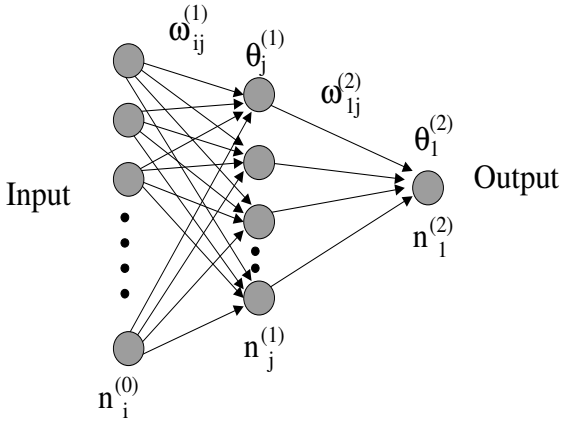

Figure 6.2: *A schematic view of a multilayer-perceptron. Here the processing direction goes from left to right and the output layer consists of only one neuron.*

A weight, $\omega_{ij}^{(k+1)}$, describes the synapses between the neurons $n_i^{(k)}$ and $n_j^{(k+1)}$. The weight is used by the receiving neuron $n_j^{(k+1)}$ to sum up its incoming signals. Furthermore, each neuron has an activation level θ_i. The response of the neuron is modeled by an activation function depending on the sum of the weighted incoming signals minus its activation level. The

activation function could be described by a step function, such as:

$$f(x) = \begin{cases} 0 & , \quad x \leq 0 \\ 1 & , \quad x > 0 \end{cases}$$

However, in order to have differentiation capabilities, the commonly used function has the form

$$f(x) = \frac{1}{1 + e^{-2x}} \tag{6.1}$$

and is called the sigmoid function (see Figure 6.1).

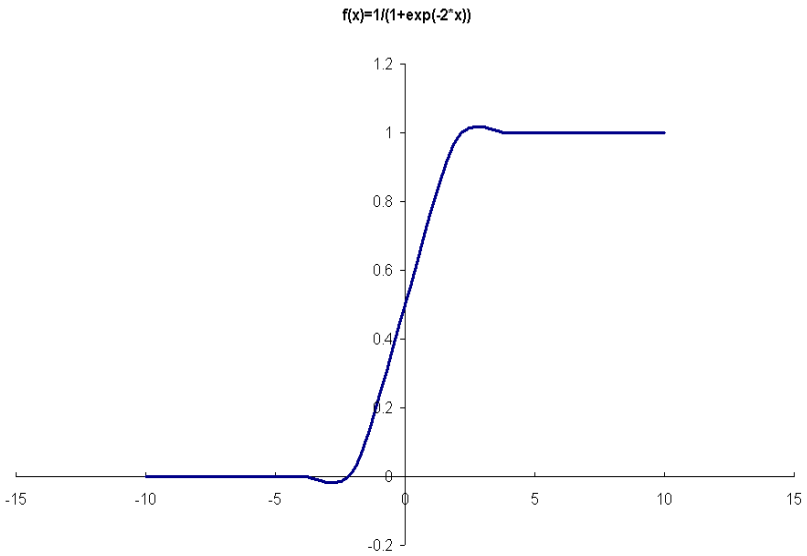

Figure 6.3: *The sigmoid function.*

In the multilayer perceptron model no connections between the neurons of the same layer are allowed. The multilayer perceptron consists of the input layer of neurons, the output layer and one or more hidden layers. The output layer can consist of one or more output neurons. In Figure 6.2 a multilayer perceptron model is shown, consisting of three layers (an input layer, a hidden layer and an output layer), with one output neuron in the output layer. In this example, for each vector $n_i^{(0)}$ of dimension N (N being the number of input variables given to the system which is equal to the number of input

neurons), a response $n_j^{(1)}$ and $n_k^{(2)}$ is calculated in the following way:

$$n_j^{(1)} = f(\textstyle\sum_i \omega_{ij}^{(1)} \cdot n_i^{(0)} - \theta_j^{(1)})$$

$$n_k^{(2)} = f(\textstyle\sum_j \omega_{jk}^{(2)} \cdot n_j^{(1)} - \theta_k^{(2)})$$

with f being the sigmoid function (equation (6.1)).

The output of the three layer system is therefore:

$$F(\vec{x}) = f(\sum_j \omega_{j1}^{(2)} f(\sum_i \omega_{ij}^{(1)} x_i - \theta_j^{(1)}) - \theta_1^{(2)}) \tag{6.2}$$

For the purpose of this analysis it was sufficient to use only one output neuron, the output of which is trained to be 1 for signal events and 0 for background. In practice, the output number has a continuous range of values, between 0 and 1, but peaking at 1 for signal and 0 for background.

One can visualize a Multilayer Perceptron and its training by taking an example of a simplified NN. One could have two input neurons in the first layer and one neuron in the output layer Figure 6.4.*c*. The NN has to distinguish between two classes of events: the signal, represented in Figure 6.4.a and 6.4.b as filled circles, and the background, represented in the same figure as empty circles. The computations of the neurons in the hidden layer of the NN can be modeled as a coordinate transformation. For each point of the input space, $\{x_1,\ x_2\}$, the two neurons of the hidden layer each compute an output value, $\{y_i,\ i = 1, 2\}$.

$$\begin{aligned} y_1 = n_1^{(1)} &= \textstyle\sum_i (\omega_{i1}^{(1)} \cdot n_i^{(0)} - 0) \\ &= \omega_{11}^{(1)} \cdot x_1 + \omega_{21}^{(1)} \cdot x_2 \\ y_2 = n_2^{(1)} &= \textstyle\sum_i (\omega_{i2}^{(1)} \cdot n_i^{(0)} - 0) \\ &= \omega_{12}^{(1)} \cdot x_1 + \omega_{22}^{(1)} \cdot x_2 \end{aligned}$$

These output values can be interpreted as the coordinates of a point in the input space of the output neuron. The output neuron then computes its output value from the transformed coordinates. After being trained with these events, the NN will give an output equal to 1 for a certain class of inputs which are above a certain line, or equal to 0 if the given inputs are below the same line in the transformed space of coordinates $\{y_1,\ y_2\}$.

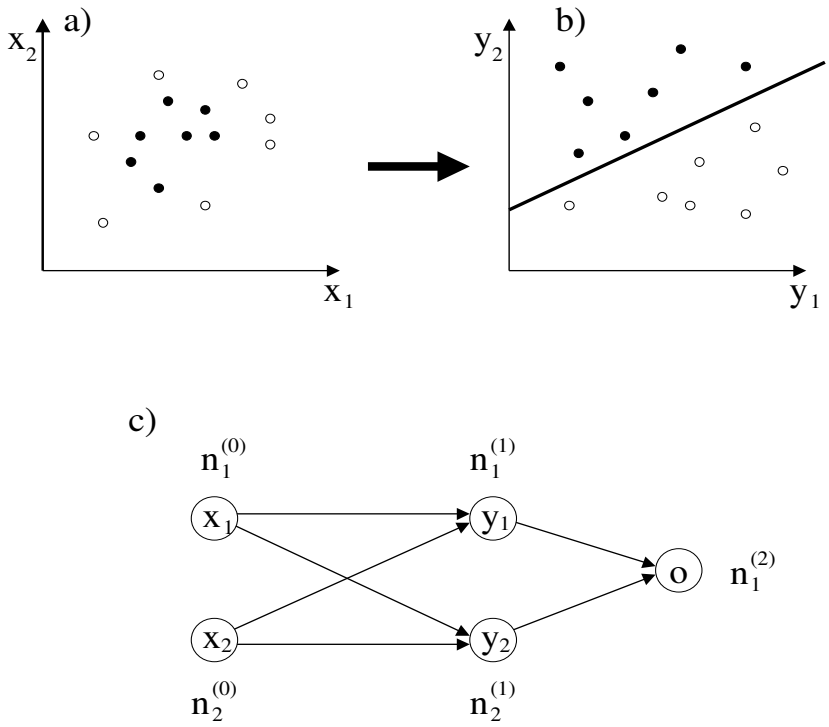

Figure 6.4: *An intuitive view of the training process of multilayer perceptron NN*

6.2.2 The Process of Training

In order to get the desired answer as an output, the neural network has to be trained. This means that the weights $\omega_{ij}^{(k)}$ and the activation levels $\theta_i^{(k)}$ have to be iteratively changed in order to get the answer one wants, in this case, the single output neuron.

The training is usually done with a Monte Carlo data set, where the amount of signal and background events has to be the same, such that the NN is not frequently trained to better distinguish the particular class of events being more often shown to the net. A rule of thumb is that the Monte Carlo dataset used for training should have approximately 10 times more input vectors than the number of free parameters of the NN. Once the training is completed the NN should be able to distinguish the desired signal in a data sample which it has never seen before.

The training is done by minimizing the mean squared error, defined as:

$$E(\omega_{ij}^{(1)}, \theta_j^{(1)}, \omega_{j1}^{(2)}, \theta_1^{(2)}) = \frac{1}{2}(S - {n_1}^{(2)}) \tag{6.3}$$

where S is the value of the desired feature, issued from the Monte Carlo, and ${n_1}^{(2)}$ is the value output by the NN. The simplest method to minimize the mean square error during the learning phase is the so-called error back-propagation (BP) method.

Within the BP method, free parameters are changed with gradient descent bycalculating, for each Monte Carlo vector, the mean squared error and to use this information to induce the correction which will be applied to the free parameters:

$$\begin{aligned} \omega_{p+1} &= \omega_p + \Delta\omega_p \\ \theta_{p+1} &= \theta_p + \Delta\theta_p \end{aligned}$$

where the index p means the p-th set of input vectors (which can consist of one or more Monte Carlo vectors). The corrections are calculated the following way, where the factors α and η are further described:

$$\begin{aligned} \Delta\omega_p &= \eta\frac{\delta E_p}{\delta\omega} + \alpha\omega_p \\ \Delta\theta_p &= \eta\frac{\delta E_p}{\delta\theta} + \alpha\theta_p \end{aligned} \tag{6.4}$$

Thus, the correction consist of a gradient descent term and a momentum term to stabilize the learning. The gradient descent term is weighted by a factor η, which is chosen to be small ($\eta << 1$) in order to avoid unacceptably large changes induced by one outlying learning input vector (or set of input vectors). The momentum term depends on α which connects the $p+1$-th correction to the p-th correction in order to avoid giving a weight that is too large to a single input vector (or set of input vectors).

The gradient descent method, like the BP method, assumes that the learning rate is the same in all directions of the ω space. Other corrections can also be used, which take into account the curvature information and are known as second order methods (i.e. Newton method) [46]. For pattern recognition problems in high energy physics these methods do not offer better performance than the BP method, which is simple to implement.

6.2.3 The RPROP Method

In the standard BP method with dynamic learning parameters (when the optimal learning rate η varies during the learning phase, as explained in the next subsection), one disadvantage is that the weight step $\Delta\omega_p$ does not only depend on the learning rate η, but also on $\frac{\delta E_p}{\delta\omega}$. Thus, an unexpected behaviour of the derivative can perturb the learning rate. A method which is independent of the size of the derivative is the Resilient Propagation (RPROP)

method, where the correction $\Delta\omega_p$ (see eq.(6.4)) is summed the following way:

$$\Delta\omega_p = \begin{cases} \eta^+\Delta\omega_{p-1} & ,if \quad \frac{\delta E_p}{\delta\omega}\cdot\frac{\delta E_{p-1}}{\delta\omega} > 0 \quad and \quad \frac{\delta E_p}{\delta\omega} < 0 & (I) \\ -\eta^+\Delta\omega_{p-1} & ,if \quad \frac{\delta E_p}{\delta\omega}\cdot\frac{\delta E_{p-1}}{\delta\omega} > 0 \quad and \quad \frac{\delta E_p}{\delta\omega} > 0 & (II) \\ -\eta^-\Delta\omega_{p-1} & ,if \quad \frac{\delta E_p}{\delta\omega}\cdot\frac{\delta E_{p-1}}{\delta\omega} < 0 & (III) \\ -\Delta\omega_{p-1} & ,if \quad \frac{\delta E_p}{\delta\omega}\cdot\frac{\delta E_{p-1}}{\delta\omega} = 0 \quad and \quad \frac{\delta E_p}{\delta\omega} > 0 & (IV) \\ \Delta\omega_{p-1} & ,if \quad \frac{\delta E_p}{\delta\omega}\cdot\frac{\delta E_{p-1}}{\delta\omega} = 0 \quad and \quad \frac{\delta E_p}{\delta\omega} < 0 & (V) \\ 0 & , \quad otherwise & (VI) \end{cases}$$

with $0 < \eta^- < 1 < \eta^+$.

This algorithm implies that as long as the minimum ($\frac{\delta E_p}{\delta\omega} < 0$) is approached, without the changing of the sign of the partial derivative (case I), the learning rate (η^+) is strongly encouraged. When the minimum ($\frac{\delta E_p}{\delta\omega} > 0$) is left, without a change in the sign of the partial derivative (case II), the learning rate is discouraged by the same amount ($-\eta^+$). When the minimum is over-jumped (change of sign of the partial derivative), the learning is discouraged by a smaller amount ($-\eta^-$), taking into account that one might just pass a locally insignificant perturbation. In the last three cases, one is zero or one step away from the minimum.

As it can be seen from this algorithm, the magnitude of the partial derivatives is never used, but only the information of their signs. The advantages of RPROP are: easy implementation, robustness and reduced number of learning steps.

6.2.4 Dynamic Learning Parameters

The name of *dynamic learning parameters* comes from the fact that the optimal leaning rate η varies during the learning phase. At the beginning, the learning rate should be large, to quickly reach way the zone close to the minimum. After getting close to the minimum, the learning rate has to become smaller and smaller, in order to settle the network properly.

For achieving these requests, one can connect the learning rate to the mean square error:

$$\eta_{p+1} = \begin{cases} \eta_p \cdot \gamma & if \ E_{p+1} > E_p \\ \eta_p \cdot (1 + \frac{1-\gamma}{10}) & if \ E_{p+1} \leq E_p \end{cases}$$

The scale factor γ should lie between 0 and 1. Using this method, η decreases when the mean square error increases, which means that the network is leaving

the zone where the minimum lies. The learning rate increases when the NN gets closer to the minimum.

The important point is that the learning rate decreases faster when leaving the minimum than it would increase by approaching it. As an example, one chooses $\gamma = 0.8$ and for a given (set of) input vector, of index p, one would have $\eta_{p+1} = 0.8 \cdot \eta_p$ in the first case, but $\eta_{p+1} = 1.02 \cdot \eta_p$ in the second one. As a result, the network has the tendency to get closer and closer to the minimum over the whole learning process.

6.2.5 End of Training

A method of checking if the training has reached its end is to use a second Monte Carlo data set. This second sample, called the validation data set, has to be independent of the first one. It is not actually used for learning purposes, but for monitoring the performances of the trained network on unknown data.

After having done a complete learning iteration on the first dataset, one calculates the sum of all mean squared errors for the validation data set:

$$\langle E \rangle = \frac{1}{N} \sum_{p=1}^{N} E_p \tag{6.5}$$

In the case where the $\langle E \rangle$ is deteriorating after having reached a minimum, the network has over-learned and the learning process should be stopped.

In principle one can simulate any complicated function analytically if one has enough input vectors to do the training. When the shape of the function is too complicated the variety of the input vectors will be insufficient to adjust the weights. Since the available information used to train the NN is not unlimited, one has to use several (hundred) times the same sample events, ideally with a different order in which they are presented to the net. By presenting the same events to the net too many times, as samples for how a signal event and how a background event should look like, the weights of the net are trained to make an almost perfect selection of the showed inputs. It therefore becomes rigid and fails to distinguish between events it has never seen before. In such a situation one says that the net has over-learned the examples, or that it became over-trained.

6.3 Implementation in JETNET

The Neural Net JETNET 3.0 [46] uses the FORTRAN language to implement its algorithms. It is a NN commonly used by the high energy physics community and was developed by the physics department of the University of Lund (Sweden). One has the possibility to choose between a number of algorithms with optional features.

In this analysis the multilayer percepton neural network architecture shown in Figure 6.2 was used. The first layer corresponds to sensor variables x_k and the top layer outputs the features o_i (the feature functions F_i) of the event so that it is a charm-signal or a background event. The hidden layer enables non-linear modeling of the sensor data.

The learning algorithm was chosen to be RPROP. This choice was based on a benchmark test on a medical data set reported in [45] RPROP to outperform all other learning algorithms, both in speed and quality. RPROP is an improved version of the back-propagation algorithm. BP itself is a very commonly used learning algorithm because it is simple to implement and it has good performance.

The NN used by this analysis had only one hidden layer.

6.4 Neuronal Nets Used

The c-quark mass lies between the light u-, d- and s-quark masses and the heavy b-quark mass. This makes the kinematic properties of the signal charm-events to have intermediate characteristics when compared to the kinematic values of the two sorts of background: uds and b. This was the physics reason why the approach used here consisted in training two different NN; one to distinguish uds-events from the c-events, and the other to distinguish b-events from the c-events. The kinematic variables were different for each of the five channels that were analysed, such that two NN were built for each channel. One NN with five times the input nodes was not used, because one would have to compute additional weights, linking the input neurons of each NN with the remaining four NN.

The two NN had their weights adjusted separately, despite the fact that both of them used the same sample of charm signal events for training.

By comparing the uds- and the b-background events separately one can optimize the p_{uds}- and p_b-cuts on the two NN outputs, and make a finer tuning of them, with respect to the total error, then by having the two backgrounds merged. This is because, out of the largest systematic uncertainties, some come from the uds-component and some from the b-component. By treating both these components as a single background variable, the cut on it is optimal from systematic uncertainty point of view, but not from statistical error one.

Also using two NN has the advantage that one obtains distributions with more distinct difference from the charm distributions than when one compares the charm distribution to the global (mixed) uds- and b-distributions. As a visual example, one can associate the red color to the distributions coming from uds-events, the yellow color to the distributions coming from b-events, and the intermediate orange color to the distributions coming from c-events. It is intuitively easier to distinguish separately between orange and red and, separately, between orange and yellow, than to distinguish between orange and the mixed combination of red and yellow, which is also orange in the

first approximation. By deciding from the beginning to use separate NNs for separate classes of background one minimizes the time necessary to train the NN. This step can be theoretically justified by the "Divide et Impera" algorithm, used in sorting.

The training sample was divided into two equal subsamples:

- One subsample was used to calculate the weights (to do the training itself)
- The other subsample was used to check the output separation obtained between the signal and background (as explained in Section 6.2.5).

The doubled numbers showed in Table 6.1 are intended to highlight this fact.

Out of the total sample of MC data, roughly 10% was used to train the NN. For some channels this percentage was not sufficient to find a large number of true D meson candidates. This is because the MC data used here were produced for general ALEPH purposes and not particularly for this analysis. The quantity of events available in MC was proportional to the production rates of each of the five (a)–(e) decay channels listed in Chapter 5. The differences in the decay branching ratios of D^0 mesons via the first three channels ($BR(D^0{}_{(a)}) = 3.85\%$, $BR(D^0{}_{(b)}) = 13.9\%$, $BR(D^0{}_{(c)}) = 7.6\%$) made the number of events one had available to train the NN to vary from channel to channel, as a function of production rates rather than a function of the number of neurons present in the net. In order to complete the sample of MC training events, events from the dedicated $c\overline{c}$ MC were used, in addition to the 10% from the general $q\overline{q}$ MC (see Table 4.1).

As one can see in Table 6.1 for the first channel (channel (a)), a small number of events ($2 \cdot 2200$) was used for training compared to the b- and c-channels. With 11 input neurons, one output neuron and 25 intermediate neurons, a number of 300 weights (free parameters) had to be determined. The use of 2200 events made the number of input vectors a factor of 7.3 larger than the number of free parameters. Even if less than the accepted empirical value of 10, this number of training events was enough, because channel (a) was, from the topological point of view, a very clean channel. When trying to minimize the number of neurons in the intermediate layer, it was found that the CPU time needed to train the NN was not critical and the same number of hidden neurons was chosen as for the other $D^* \to D^0\pi_s$ channels.

Regarding the number of events available for training, the situation in Table 6.1 was the opposite, for channel (b). One could use $2 \cdot 252000$ background and c-events for training, but the time required for training became excessively large, compared to other channels. A number of $2 \cdot 32000$ events was chosen, which preserved the proportion between the MC data from the 1991 to 1995 period and the corresponding real data. However, this large number of input vectors also had to be chosen because of the reconstruction of the π^0. In the case of the π^0 more parameters are needed to describe its final state than

it was the case for a charged pion. Therefore the training of the NN takes longer and the effect of over-training begins later. The number of events used for the training was therefore increased, from 10 to 100 times larger than the number of weights to be computed.

For the channels (c), (d) and (e), all the events available for training have been used.

Channel	training events	epochs	input nodes
a).$D^{\star+} \to D^0 \pi_s^+$ $\hookrightarrow K^- \pi^+$	$2 \cdot 2200$	300	11
b).$D^{\star+} \to D^0 \pi_s^+$ $\hookrightarrow K^- \pi^+ \pi^0$	$2 \cdot 32000$	300	11
c).$D^{\star+} \to D^0 \pi_s^+$ $\hookrightarrow K^- \pi^+ \pi^- \pi^+$	$2 \cdot 27000$	300	11
d).$D^0 \to K^- \pi^+$	$2 \cdot 28800$	300	8
e).$D^+ \to K^- \pi^+ \pi^+$	$2 \cdot 18000$	300	8

Table 6.1: *Values of the parameters for the events used to train the NNs*

When calculating the weights, the order of succession for the training events, whether they are signal or background, was chosen to be random. All the available samples of training events is given during what is called an epoch. Then the same events are repeatedly presented, in the same order, roughly a couple of hundreds epochs per training. Even if the number of events contained by one epoch varied, affecting the needed CPU time, the number of epochs was kept the same.

The NNs, used to decide if an event belongs to one of the channels a-c, contains 11 input neurons, fed with the eleven variables ($NN-1$ to $NN-11$) described in Chapter 7. For channel d and e only the first eight ($NN-1$, $NN-8$) variables were used. The number of training epochs was chosen to be 300 because the NNs were saturated for this number in all the five channels. The saturation means that further training, on a larger number of epochs, doesn't improve the NN performances.

Before being presented to the NN the input variables are rescaled, such that they all lie approximatively in the same region: [0, 1]. This rescaling

could have been done by the NN themselves; the algorithm doesn't need an implementation depending on the range of the input variables. However, it would take a significant longer time for training because the number of operations to be performed increases.

Because a final cut is performed on the mass of the D candidate, the NNs were trained to distinguish between the charm signal and the two types of background in a larger D mass range. By training the NNs only in these mass-windows a better separation would have been obtained in this regions between the signal and non-signal events. But the uds-background mass distribution has to be subtracted from the events selected as charm. This distribution would not be a polynomial one anymore, and would contain a dip inside the window used for training. This irregularity would have to be parametrized relying completely on the MC information, and it would destroy the feature of the analysis which is to extract the background directly from the data. This would increase the systematics uncertainty on the background subtraction and therefore training on the D mass window is not performed.

Chapter 7

The Charm Selection

Before the preselection cuts were applied, the data sample contained with 6986 thousand Monte-Carlo and 3961 thousand real data hadronic events. In order to compare the MC predictions to data, the number of available MC events is rescaled at the number of available data, the scaling factor for the MC data being 0.567.

An event is considered as belonging to a channel if the reconstruction can produce at least one D candidate for that channel. At this stage, a D candidate is defined only by the presence of a minimum number of particles

Channel	(a)	(b)	(c)	(d)	(e)
1. $cos(\theta)$	< 0.7	< 0.7	< 0.7	< 0.7	< 0.7
2. R_I	< 2.5	< 2.5	< 2.5	< 2.5	< 2.5
3. $N_{VDEThits}$	> 2	> 2	> 2	> 2	> 2
4. $p_K[GeV]$	> 2.0	> 2.0	> 2.0	> 1.0	> 1.0
$p_\pi[GeV]$	> 0.4	> 0.4	> 0.4	> 1.0	> 1.0
5.1. $p_{\pi_s}[GeV]$	$1.0 - 3.5$	$1.0 - 3.5$	$1.0 - 3.5$	-	-
5.2. $\lvert m_{D^0} - M_{D^0}\rvert$[GeV]	< 0.5	-	< 0.5	-	-
$m_{D^0}[GeV]$	-	$1.0 - 2.5$	-	1.54–2.19	-
m_{D^+}[GeV]	-	-	-	-	1.0–2.5
5.3. $m_{D^*} - m_{D^0}$[GeV]	0.143–0.148	$1.5 - 3.0$	0.143–0.148	-	-

Table 7.1: *The cuts applied for the preselection. The cuts 1, 2 and 3 are applied before the event is assigned to a decay channel.*

that could be assigned as decay products for that channel. This cut in the multiplicities is easily fulfilled because of the high number of tracks typically produced in a Z^0 decay (see Section 3.2). All the applied preselection cuts, described in chapter 5, are summarised in Table 7.1.

7.1 Reconstruction of D-Decays

7.1.1 Particle Identification

For each event the selection of $D^0, D^+, D^{\star +}$ decay modes started by identifying which of the charged tracks can be assigned to a K and which ones to a π particle. The combinatorial background, due to false particle type assignments, was reduced by identifying charged particles using dE/dx measurements in the TPC.

A particle of momentum p was assigned to be a kaon if its measured value of ionization loss, dE/dx, was close to the value expected for a kaon K (cut 2):

$$\begin{aligned} \frac{|dE/dx(K,p) - <dE/dx(K,p)>|}{\sigma(K,p)} &< 2.5 \\ K &= \textit{kaon} \\ p &= \textit{momentum of the kaon} \end{aligned} \tag{7.1}$$

A particle of momentum p was assigned to be a pion if its measured value of

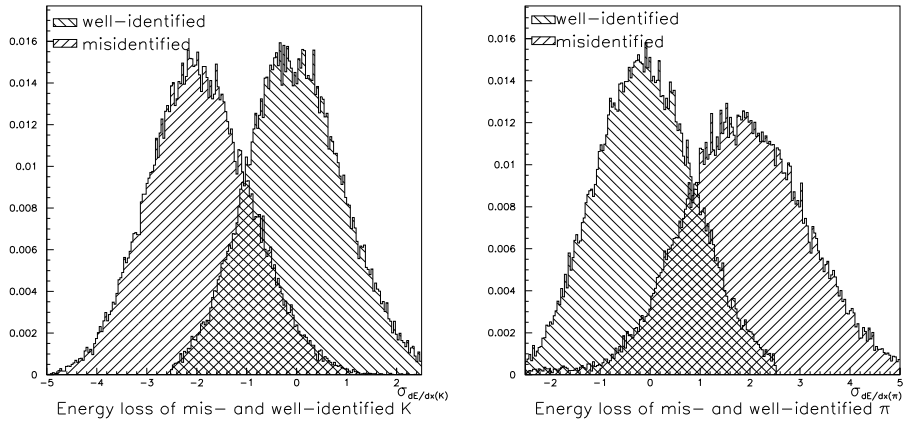

Figure 7.1: *Energy loss, in deviations from the average energy loss, for kaons and pions in the momentum ranges given in Table 7.1*

ionisation loss, dE/dx, was close to the value expected for a pion π (cut 2).

$$\begin{aligned} \frac{|dE/dx(\pi,p) - <dE/dx(\pi,p)>|}{\sigma(\pi,p)} &< 2.5 \\ \pi &= \textit{pion} \\ p &= \textit{momentum of the pion} \end{aligned} \tag{7.2}$$

In Figure 7.1 one can see that about one third of the false assigned tracks (K misidentified as π, and π misidentified as K) were rejected by this cut.

When there are two possible assignments for the same particles, the event is considered under both hypotheses further in the analysis.

7.1.2 Channel Identification

To compute the number of charm candidates decaying leptonically one needs to know the charge of the charm quark. As shown in Section 2.6.1, the charge of the lepton is opposite to the charge of the decaying charm quark. Therefore, for this analysis, the correct identification of the charge of the initial charm quark is very important. Since, in the decay channels considered, this charge is directly correlated with the charge of the reconstructed kaon, one starts the identification of the decay products by identifying the kaon.

The details of the procedure are the following: The reconstructed tracks from charged particles are sorted into a list. In the procedure of identifying the decay channel one takes each charged track out of this list and assumes it is a kaon if it satisfied Equation 7.1. The remaining charged tracks are searched for reconstructed pion candidates (satisfying Equation 7.2), which in combination have to have a charge to match the electrical charge of the kaon and the searched decaying D. Then one tests, until all the possibilities are exhausted, every combination of K and π candidates to identify the decay channel, allowing for multiple assignments.

The D^{*+} was reconstructed in the channels (a), (b) and (c), as noted in Section 5.3, through its decay mode $D^{*+} \to D^0\pi_s$. Since the mass difference $M_{D^{*+}} - M_{D^0} = 145\,\mathrm{MeV}$ is slightly higher than the mass of the pion $m_\pi = 139\ MeV$, the pion π_s produced by the decay $D^{*+} \to D^0{\pi^+}_s$ has a small momentum in the D^{*+} rest frame (soft pion). In order to reconstruct the D^{*+}, once a D^0 candidate was found, a pairing with an additional (low transverse momentum) track, collinear with the D^0, was made.

After applying the preselection cuts (see Section 5.4 and Table 7.1) good agreement is maintained between the total number of events selected in MC and in data (see Table 7.2), the presented discrepancies being explained in Section 7.5. The first three columns, giving the decomposition per flavour classes, already show a slight enhancement of the percentage of events coming from primary charm quarks.

For channels (a) and (b) the minimum momentum cuts, shown in Table 7.1 – row 4, were imposed in order to reduce the combinatorial background due to pion/kaon interchange. Because the D^0 is neutral one requires that the combination of the initial K and π candidates be neutral also.

A large fraction of the combinatorial background, which increases with the number of tracks produced from the D-meson decay, was also reduced by the following selection criteria. The invariant mass of a system combining 2 tracks ($D^0 \to K^-\pi^+$) or 4 tracks ($D^0 \to K^-\pi^+\pi^-\pi^+$) was required to be within 0.5 GeV from the D^0 mass (cut 5.2.). The D^0-meson is reconstructed only via its decay products. Its movement is not physically detected, before decay,

Channel	c_{MC}	uds_{MC}	b_{MC}	Total$_{MC}$	Total$_{Data}$
$D^{\star+} \to D^0 \pi_s^+$ $\hookrightarrow K^- \pi^+$	42%	24%	34%	25159± 159	28109 ± 168
$D^{\star+} \to D^0 \pi_s^+$ $\hookrightarrow K^- \pi^+ \pi^0$	19%	58%	24%	2348167±1532	2322899±1524
$D^{\star+} \to D^0 \pi_s^+$ $\hookrightarrow K^- \pi^+ \pi^- \pi^+$	31%	30%	39%	174232± 417	180285 ± 425
$D^0 \to K^- \pi^+$	15%	67%	18%	1088818±1043	1138898±1067
$D^+ \to K^- \pi^+ \pi^+$	18%	62%	20%	3149090±1775	3282286±1812
Total	25%	48%	27%	6785466±2605	6952477±2637

Table 7.2: *Number of candidates selected in MC and in Data after preselection cuts and before the cuts in the NN outputs and in the mass of the D meson. The numbers of Class* 16 *events in MC are rescaled to the corresponding one found in the initial data samples. The quoted errors are statistical only.*

but the candidate tracks of its decay can be fitted to a common vertex with a D^0-mass constraint in the fit. After an artificial track is made for the D^0-candidate, one searched through the remaining charged tracks to find a π_s (low transverse momentum pion) candidate which satisfies the cut 5.1. in Table 7.1. This new track was added to the reconstructed D^0-candidate of 2 or 4 tracks, and a D^{*+} candidate was kept if the mass difference $\Delta M = m(D^0\pi_s) - m(D^0)$ lay within the given limits (cut 5.3).

D^0 mesons alone (channel (d)) were selected by reconstructing the decay mode $D^0 \to K^-\pi^+$, which has the clearest signature among all the possible D^0 decay channels. A track with a momentum greater than 1 GeV, assigned the kaon mass, was combined with a track of opposite sign with a momentum greater than 1 GeV, assumed to be a pion (cut 4). The combination of these two tracks is retained if its invariant mass, m_{D^0}, satisfies cut 5.2.

The $D^\pm$ meson is reconstructed through the decay mode $D^\pm \to K^\mp\pi^\pm\pi^\pm$ (channel (e)). All triplets of charged tracks containing a kaon, with a total charge of ± 1, are considered.

7.2 Application of NN to Charm Selection

In order to eliminate as much as possible the non-charm events and the combinatorial background, two discriminating variables, $p_{\overline{uds}}$ and $p_{\overline{b}}$, were built for each channel. These are designed to separate the b and uds contributions from charm. They range between (0, 1) and reach unity when a charm event has been found. For example, $p_{\overline{uds}} = 1$ when there is a charm event which is definitely not coming from u, d, s and $p_{\overline{b}} = 0$ when there is no charm event, but a b one.

Two NN are needed, each specialised in the choice of one variable (as explained in Chapter 6). The output of the NN provides a single number, summarising all the properties discriminating the characteristics of charm compared to bottom or light flavour events. One can use the two outputs of the NN to optimise performance and to make maximal use of correlations between the two types of background. Even if the input variables for the NN are different for each of the channels, their outputs have the same discriminating meaning, independent of channel, and help to make a global overview on the entire analysis. The NN exploit the kinematic differences between the signal and the background. The inputs are:

- $NN-1$. The momentum p_D of the reconstructed D meson, which is on average higher for c than for b and uds. If the charm came directly from the Z^0 it carries a larger momentum. In this case the average fraction of the beam energy carried by a D meson in a $Z^0 \to c\overline{c}$ event was about half the energy of the beam: $\langle E_D \rangle \approx 0.5$. However, when there was a charm quark from a $Z^0 \to b\overline{b}$ decay, the initial momentum was split because of the additional decay partner. The average fraction of the beam energy carried by the D in this second case was reduced to approximatively one third, $\langle E_D \rangle \approx 0.3$, where the W takes a part of the b-hadron energy in the decay $B \to WD$. In the third case, when a uds event is produced, the momentum of the fake D-candidate tends to be lower than for charm events (see Figure 7.2).

- $NN-2$. The probability P of the track with highest impact parameter significance to come from a b particle (see Section 3.2.2), in the hemisphere not belonging to the reconstructed meson (see Section 5.1). It is high for b, compatible with zero for c (if properly reconstructed, with the charge of the charm quark correctly assigned) and uds (see Figure 7.3). This is the main discriminating variable against non-prompt charm events, because of the presence of the secondary vertex of the b–particle.

- $NN-3$. The energy loss $dE/dx(K,p)$ of the reconstructed kaon candidate. How this variable differs for the c, uds and b events is shown in Figure 7.4. In fact the variable one actually uses is $R_I(K)$ defined in

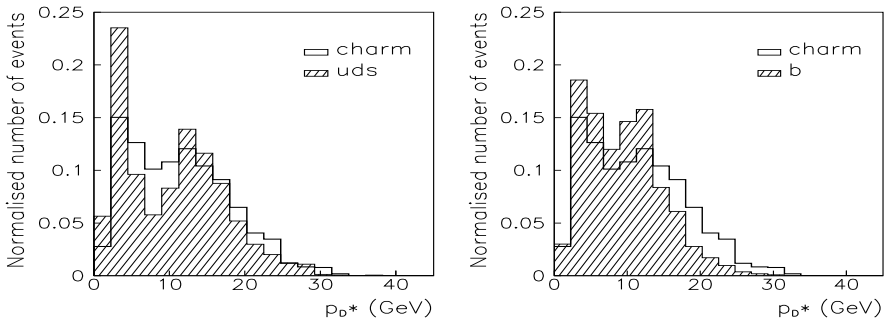

Figure 7.2: p_{D^*} *distribution, here for channel* (a)

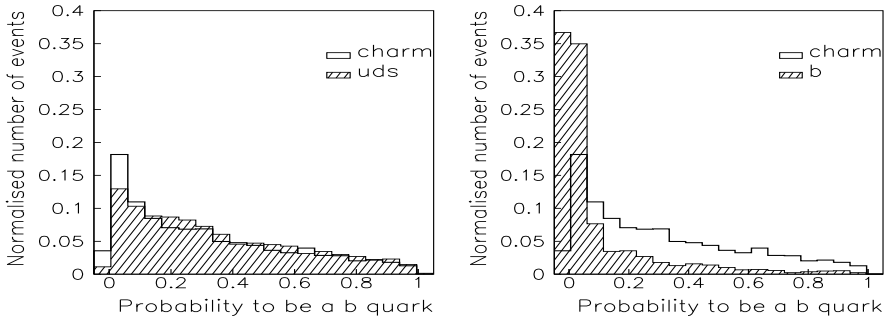

Figure 7.3: *Distribution of the probability* P *that the* D *meson came from a* b *quark, here for channel* (a)

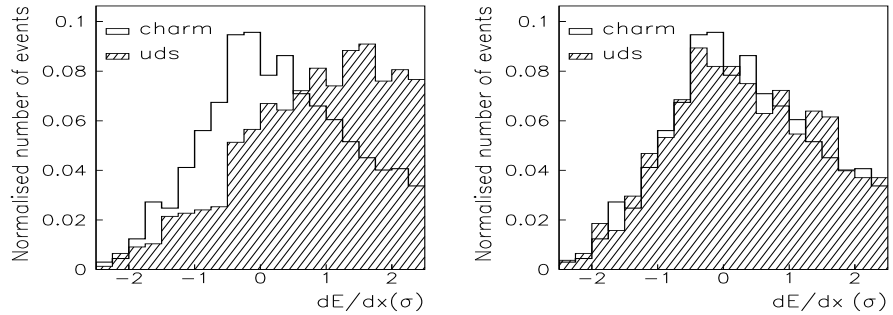

Figure 7.4: *Distribution of the energy loss,* $dE/dx(K)$*, here for channel* (a)

Equation 3.4, where dE/dx is the combined measured ionisation, from wires and pads (see Section 3.2.4). Because in the *uds* events there are pions misidentified as kaons, the energy loss distribution of the kaon candidates is similar to the energy loss distribution of misidentified pions in Figure 7.1.

- $NN-4$. The K momentum, p_K (see Figure 7.5). For the *uds* events the kaon candidate was misidentified with a high probability. The kaon candidates truly coming from a D decay are boosted along the D direction of flight, together with the resulting momentum of the other D decay products. The randomly assigned fake kaon candidates from the

uds events might have momenta opposite to the particles assigned as the rest of the D decay products, and would therefore be smaller than the true kaon candidates. However, the leading kaon in $s\overline{s}$ events tends to have a rather high momentum.

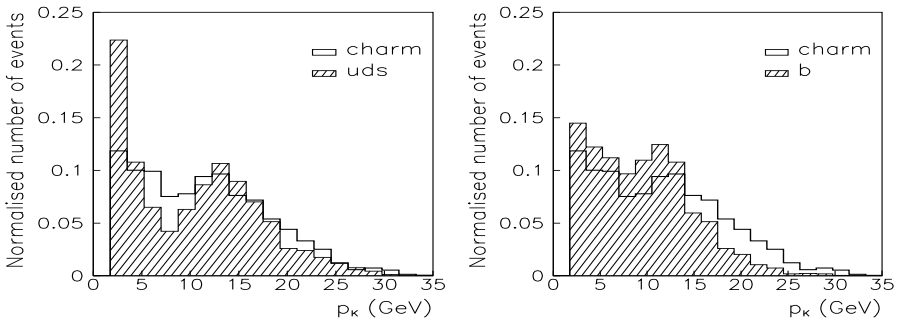

Figure 7.5: *Distribution of the kaon momentum, p_K, here for channel (a)*

- $NN-5$. The decay length significance l_D/σ_{l_D} of the reconstructed D meson candidate (see Figure 7.6). Here l_D stands for the decay length of the D candidate, while σ_{l_D} is the standard deviation of this length measurement.

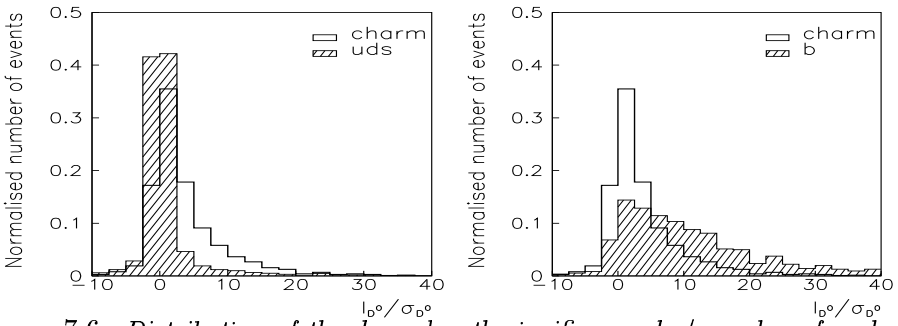

Figure 7.6: *Distribution of the decay length significance, l_D/σ_{l_D}, here for channel (a)*

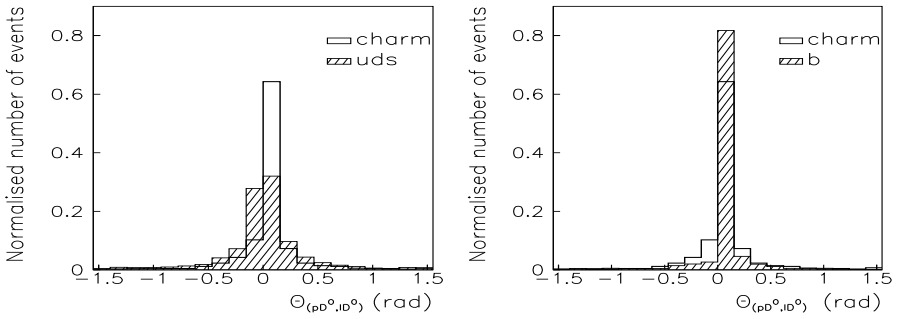

Figure 7.7: *Distribution of the angle θ_{p_D,l_D}, between the D directions in momentum and spatial coordinates, here for channel (a)*

- $NN-6$. The angle $\theta_{\overrightarrow{pD},\overrightarrow{l_D}}$ between the direction of the momentum of the D-candidate and the direction of the track of the D-candidate (see Figure 7.7), to compare the directions in momentum and spatial coordinates. For combinatorial *uds* background the two directions are not correlated and there is a uniform distribution in $\cos(\theta_{\overrightarrow{pD},\overrightarrow{l_D}})$. For properly reconstructed c and b events the two directions are close to each other.

- $NN-7$. In the D mass frame the sphericity axis of the decay products is calculated. The sphericity axis is defined as the direction which minimises the sum of the squared transverse momentum components. (For the case of two-body decays it coincides with the direction of one of the particles.) Then the angle between the sphericity axis and the meson line of flight is calculated. This angle has a flat distribution for properly reconstructed particles because D^0 and D^+, which are scalar, have a uniform distribution in the cosine of its decay angle and no direction particularly enhanced, whereas the background peaks in the forward and backward direction (see Figure 7.8).

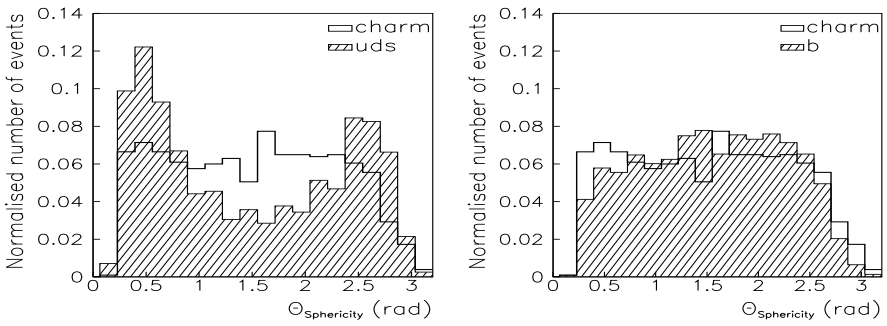

Figure 7.8: *The decay angle distribution of the D, with respect to sphericity axis, here for channel (a)*

- $NN-8$. The $\chi^2(D)$ for the D-vertex fit (Figure 7.9). For channels (a)–(d), the fit concerns the D^0 meson, while for channel e it is performed for the D^+ meson. In both of the cases the D meson is expected to have a non-vanishing decay length. The χ^2 is computed based on:
  - the 4-momenta of fitted tracks ,
  - the particle masses assigned to the tracks,
  - the vertex position,
  - the 4-momenta covariance matrix,
  - the vertex covariance matrix,
  - the correlation between the vertex and the momenta.

  A significant discriminating power does not exist between signal and background, but it is a control variable, influencing the behavior of the other variables used as input to the NN, because it gives a hint how

reliable the other variables are (events characterised by larger values of $\chi^2(D)$ should weight less than those characterised by small values).

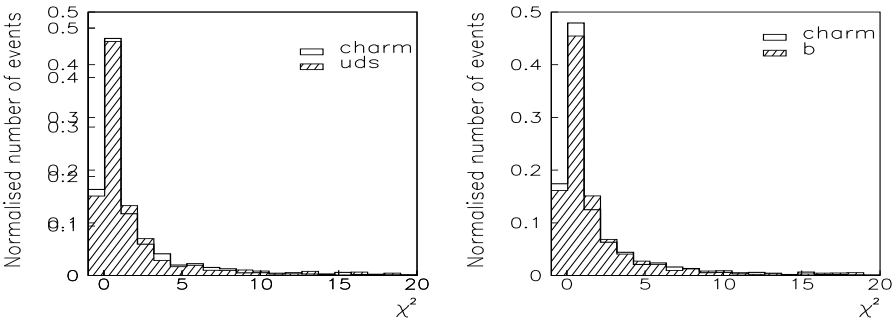

Figure 7.9: $\chi^2(D)$, *here for channel* (a)

- The following only applies for $D^{\star+}$ channels: $D^{\star+} \to D^0\pi_s$ (channels (a), (b) and (c)).
  - $NN-9$. The mass difference between the D^{*+} and the D^0 candidates, $m_{D^{*+}} - m_{D^0}$ (see Figure 7.10). The two distributions on which the NN is trained to distinguish between the c signal and the b background are almost identical because the selected D mesons come from non-prompt charm quarks, this variable having a good discrimination power only against the *uds* background.

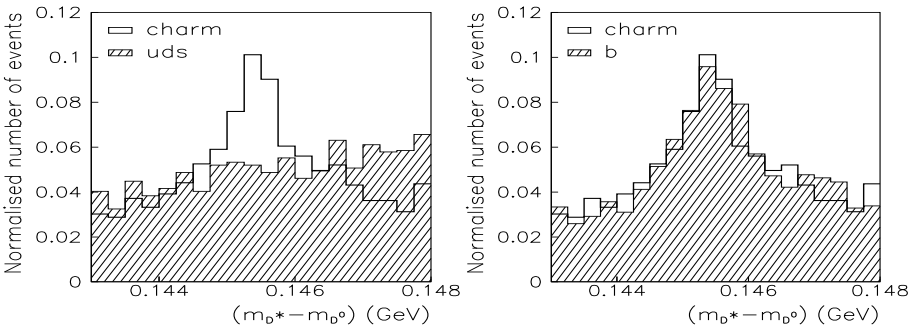

Figure 7.10: $m_{D^{*+}} - m_{D^0}$, *here for channel* (a)

  - $NN-10$. The momentum of the soft pion, p_{π_s} (see Figure 7.11)
  - $NN-11$. The momentum of the D^0-candidate, p_{D^0} (see Figure 7.12)

  In these channels, the mass m_{D^0} of the reconstructed D^0 candidate is kept for the final mass cuts, in order to judge the component of background. The mass difference $m_{D^{*+}} - m_{D^0}$, which is very close to the rest mass of the π_s, peaks at low values for properly reconstructed $D^{\star+} \to D^0\pi_s$ decays which originate from both b– and c–quarks.

A detailed description of the NN training is given in Chapter 6.

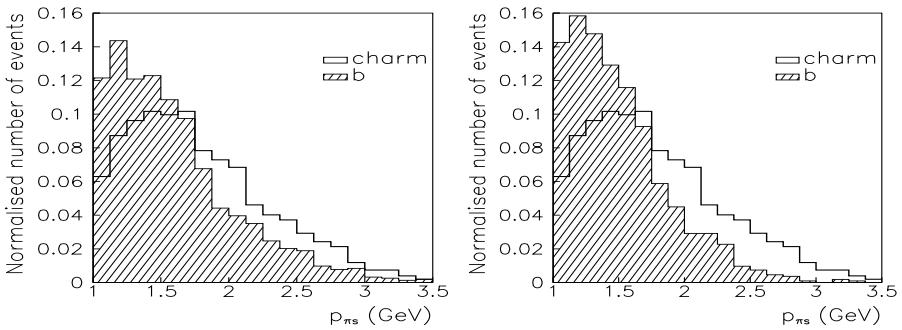

Figure 7.11: *π_{soft}' momentum, here for channel (a)*

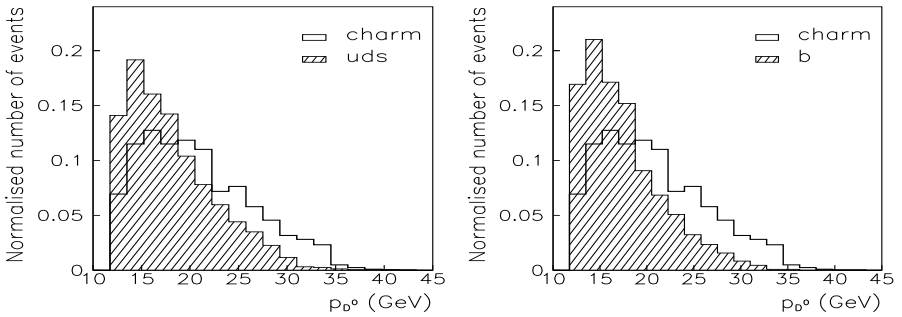

Figure 7.12: *p_{D^0} momentum distribution, here for channel (a)*

7.3 The Working Point

The charm selection is based on three final cuts: one cut on the mass of the D^0 or D^+ meson, and two cuts in the NN outputs, $p_{\overline{uds}}$ and $p_{\overline{b}}$. These three cuts have been applied in order to increase the signal to noise ratio. This point in the analysis, where the cuts in the mass window and NN outputs are fixed, is called the working point. A study has been made on the Monte Carlo sample in order to establish this working point.

7.3.1 Mass Window Cuts

The final charm selection is made by placing constrains on the mass of the reconstructed D meson, so that it lies within the expected range. The allowed range of the mass of the D meson candidate, in each channel, is shown in Figures 7.13 to 7.17. In these figures reconstructed mass spectra of the D meson candidate is shown before and after the cuts in the NN outputs. The plots on the left side have a larger number of events, because there are more candidates per channel before the NN cuts than after them. In all the channels the signal purity is enhanced, after cutting in the NN outputs, with the price of a large loss in statistics.

The mass window cuts were calculated using two steps: In the first step narrow preliminary cuts in the mass window were defined. After having ap-

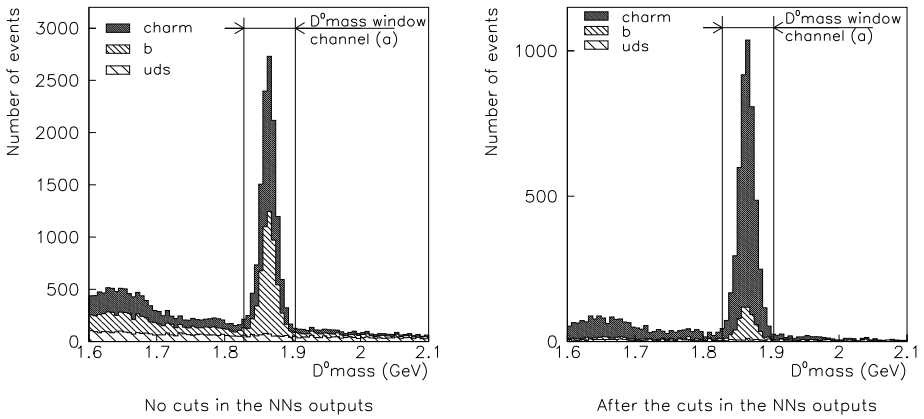

Figure 7.13: *Influence of NN on D^0 mass spectra, in channel $D^{*+} \to D^0\pi^+, D^0 \to K^-\pi^+$, with the decomposition into the flavour classes taken from MC.*

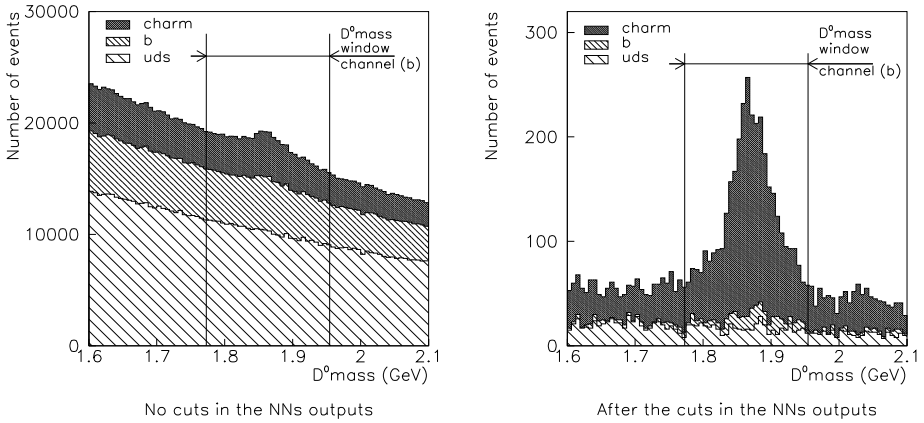

Figure 7.14: *Influence of NN on D^0 mass spectra, in channel $D^{*+} \to D^0\pi^+, D^0 \to K^-\pi^+\pi^0$, with the decomposition into the flavour classes taken from MC*

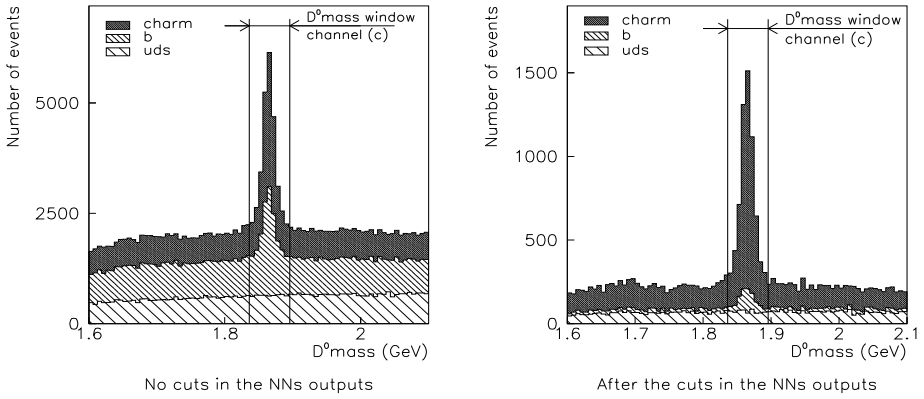

Figure 7.15: *Influence of NN on D^0 mass spectra, in channel $D^{*+} \to D^0\pi^+, D^0 \to K^-\pi^+\pi^-\pi^+$, with the decomposition into the flavour classes taken from MC.*

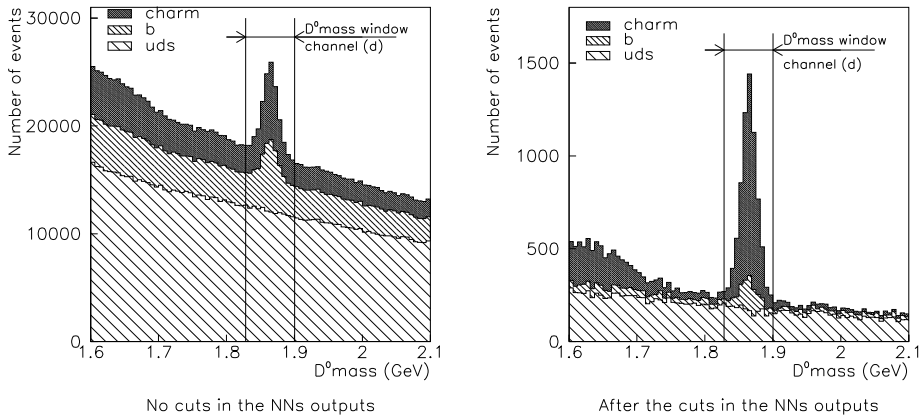

Figure 7.16: *Influence of NN on D^0 mass spectra, in channel $D^0 \to K^-\pi^+$, with the decomposition into the flavour classes taken from MC.*

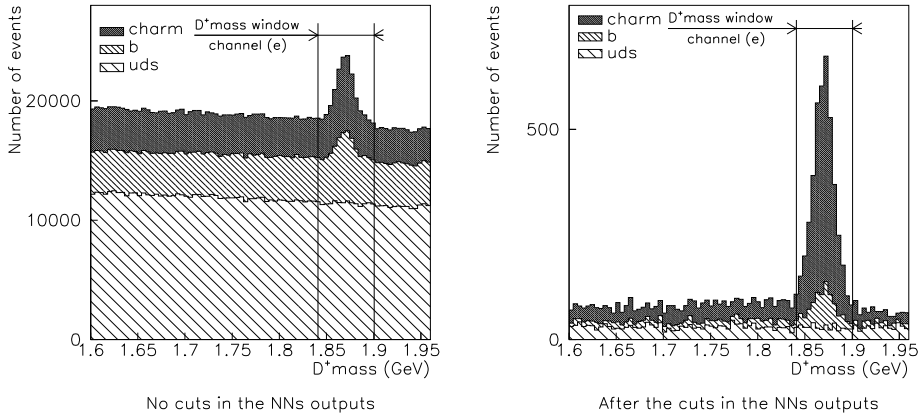

Figure 7.17: *Influence of NN on D^+ mass spectra, in channel $D^+ \to K^-\pi^+\pi^+$, with the decomposition into the flavour classes taken from MC.*

plied the cuts in the $(p_{\overline{uds}}, p_{\overline{b}})$ plane (defined hereafter), one was left with a preliminary data sample of selected events. Using this sample, a Gaussian fit over the signal was applied. This allowed a clean determination of the mean value m_D, and variance σ of the signal. The final cuts for the mass window were then chosen to be $m_D \pm 3\sigma$ (see Table 7.3).

7.3.2 NN Output Cuts

The cuts on the NN outputs, $p_{\overline{uds}}$ and $p_{\overline{b}}$, can be chosen independently. The efficiency and purity of the final charm selection can be in this way optimised separately for the two types of background, taking into account their statistical significance. By using the MC data, to study the influence of the different quark flavour, appropriate cuts on the NN outputs were derived (see Table 7.3). In this analysis the cuts have been chosen such that in each channel

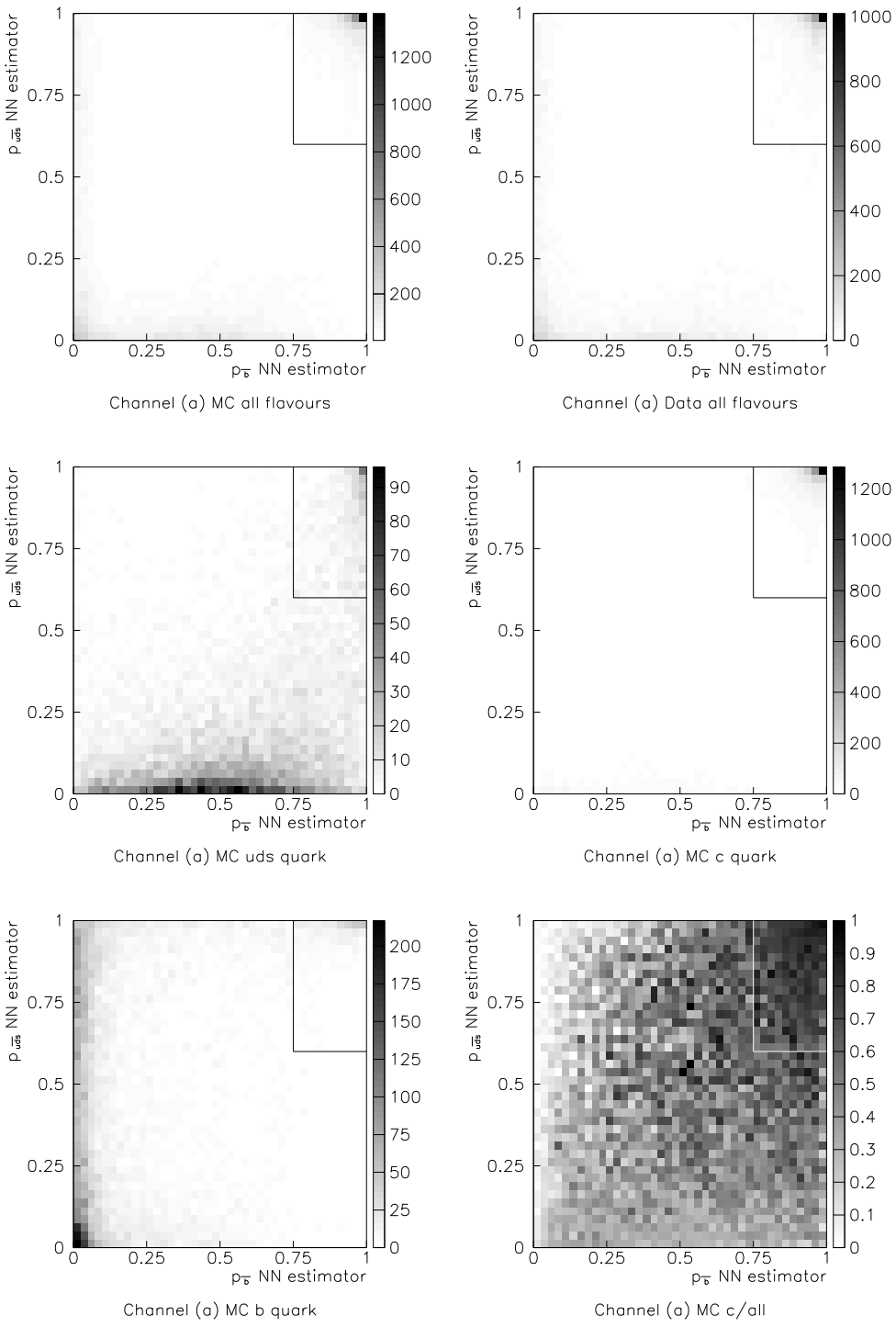

Figure 7.18: *Upper-left (1): all MC data. Upper-right (2): all experimental data. Middle-left (3) MC generated uds events. Middle-right (4) MC generated charm events. Lower-left (5): MC generated b events. Lower right (6): Histogram generated by dividing histogram (3) by (1). The box indicates the cuts which have been applied for the final selection.*

Channel	fitted m_D	fitted σ	mass window	$p_{\overline{uds}}$	$p_{\overline{b}}$
(a)	1.8645	0.0118	1.8291−1.8999	0.600	0.750
(b)	1.8722	0.0295	1.7837−1.9607	0.960	0.940
(c)	1.8647	0.0091	1.8374−1.8920	0.600	0.850
(d)	1.8627	0.0115	1.8282−1.8972	0.880	0.955
(e)	1.8694	0.0106	1.8376−1.9012	0.960	0.980

Table 7.3: *The final cuts applied on the NN outputs, $p_{\overline{uds}}$ and $p_{\overline{b}}$, and on the mass of the D meson.*

the b– and uds–contamination is less than 10% each.

In Figures 7.18 $p_{\overline{uds}}$–$p_{\overline{b}}$ diagrams are plotted, displaying for channel (a) the principle behind the NN output cuts. Similar plots, for the rest of analysed channels, are given in Appendix B (Figures B.2 to B.5). The influence of the b– and uds–contamination before and after the NN cuts on the D-mass signal are shown in Figures 7.13 to 7.17. The discrimination power of the NN can be seen by looking at the number of overlapping events in the selected D-mass window without cuts applied on the NN outputs. This is shown in Tables 7.4 and 7.6.

Channel	(a)	(b)	(c)	(d)	(e)
(a)	7187	174	33	5351	62
(b)		297964	998	5857	12889
(c)			19031	352	478
(d)				134225	3574
(e)					152528

Table 7.4: *MC event numbers (rescaled to data), before NN cuts and after mass window cuts.*

Channel	(a)	(b)	(c)	(d)	(e)
(a)	2628	2	1	685	1
(b)		2010	10	1	16
(c)			3890	0	0
(d)				4302	2
(e)					2498

Table 7.5: *MC event numbers (rescaled to data), after NN and mass window cuts*

The same events, after being subject to NN cuts, are presented in Tables 7.6 and 7.7. In these tables the number for MC and data are not directly comparable, because one has to keep in mind that after the preselection cuts 6.986 million MC events have been generated and used, while only 3.961 million real events are available.

Channel	(a)	(b)	(c)	(d)	(e)
(a)	7541	165	28	5569	70
(b)		283206	1000	5718	12325
(c)			19389	381	471
(d)				141083	3670
(e)					155886

Table 7.6: *Data event numbers, before NN cuts and after mass window cuts*

Channel	(a)	(b)	(c)	(d)	(e)
(a)	3027	0	1	786	1
(b)		2998	9	0	11
(c)			4549	0	2
(d)				5019	1
(e)					3324

Table 7.7: *Data event numbers, after NN and mass window cuts*

One can discuss the influence of the cuts in the NN outputs on the statistics, by comparing the total number of events selected in the MC and real data, shown in the last two columns of Tables 7.2 and 7.8. The influence on the percentage of selected charm events is discussed based on the values c_{MC} from these two tables.

The clearest NN discrimination between charm quarks and the uds/b background is achieved for channel (a) (see Figure 7.18), meaning that loose cuts can be applied. This is the reason why the signal to noise ratio, which is about 87% (see Figure 7.13), is the highest for channel (a). However, a non negligible b quark contamination could not be avoided (Figure 7.18, bottom left figure). Furthermore, for channel (a) the total number of events selected before and after the NN cuts is only decreasing by a factor 5 (see Table 7.4 and Table 7.5), while the percentage of selected charm events increases by a factor 2.

For channel (b), a large contamination of uds and b quarks exists before the

application of the NN cuts (see Figure 7.14) . Looking at the $p_{\overline{uds}}$–$p_{\overline{b}}$ plane (Figure B.2) one can see that a large number of the MC generated charm quarks lies in the same region as the *uds* and *b* quarks. Narrow cuts have to be applied, decreasing the number of reconstructed charm quarks by a factor 400 (see Table 7.4 and Table 7.5), while the percentage of selected charm events increases by a factor 3.5.

For channel (*c*), the charm quark region in the $p_{\overline{uds}}$–$p_{\overline{b}}$ plane (Figure B.3) is very close to the *uds* quark region. A cut at $\mathrm{p}_{\overline{uds}} > 0.6$ seemed to be a good compromise, avoiding a large contamination of the signal. The selected number of events decreased by a factor 9, while the percentage of selected charm events increases by a factor 2.

As expected (because channel (*d*) contains the type of events of channel (*a*)) the $\mathrm{p}_{\overline{uds}}$–$\mathrm{p}_{\overline{b}}$ diagrams for channel (*d*) (see Figure B.4) are behaving like the diagrams for channel (*a*): same features, same *b* quark contamination (see also Figure7.16). Channel (*d*) has slightly more noise than channel (*a*), due to the missing information carried by the π_s. Therefore, in order to reduce the *b* quark contamination, a very tight cut in $p_{\overline{b}}$ has been applied ($p_{\overline{b}} > 0.955$). The selected number of events decreased by a factor 500, while the percentage of selected charm events increases by a factor 2.

The feature of the $p_{\overline{uds}}$–$p_{\overline{b}}$ diagrams for channel (*e*) which is the most striking is that the *uds* quarks are contaminating the whole plane. A non-negligible contamination due to *b* quarks also exists (upper line in the middle right Figure B.5). Therefore, for this channel very narrow cuts had to be applied. The selected number of events decreased by a factor 200, while the percentage of selected charm events increases by a factor 3.

The numbers on the diagonal of Table 7.5 are very different from the ones in Table 7.4, given that the D^0 branching ratios are of the same order of magnitude: $BR_{D^0_{(a)}} = 3.85\%$, $BR_{D^0_{(b)}} = 13.9\%$, $BR_{D^0_{(c)}} = 7.6\%$. The large difference is due to the hard cut in $p_{\overline{uds}}$, to eliminate the non–*uds* events, as one can see in Figures 7.13 to 7.17.

7.3.3 Channel Selection

When the NN cuts are applied one can see that the interference between different channels was almost eliminated, with the exception of the interference between channels (*a*) and (*d*), where only about half of the overlap is maintained after the cuts in the NN outputs. This is expected, since both of them contain events from a $D^0 \to K^-\pi^+$ decay. The events common to the channels (*a*) and (*d*) are events where both a $D^{\star +} \to D^0\pi_s^+$ and a $D^0 \to K^-\pi^+$ decay are reconstructed.

If one event is selected in more than one channel, the channel with the highest purity is preferred (see Table 7.14) when subtracting the overlapping events:

$$
\begin{array}{lllll}
 & D^{\star +} & \rightarrow & D^0\,\pi_s^+ & \\
 & & & \hookrightarrow K^-\,\pi^+ & \text{(a)} \\
 & D^+ & \rightarrow & K^-\,\pi^+\,\pi^+ & \text{(e)} \\
\text{!bb} & D^{\star +} & \rightarrow & D^0\,\pi_s^+ & \\
 & & & \hookrightarrow K^-\,\pi^+\,\pi^-\pi^+ & \text{(c)} \\
 & & & \hookrightarrow K^-\,\pi^+\,\pi^0 & \text{(b)} \\
 & D^0 & \rightarrow & K^-\,\pi^+ & \text{(d)}
\end{array}
$$

This does not yield a bias, as long as the overlapping of the channels is negligible with respect to the total number of events reconstructed in each of the overlapping channels.

Finally, in Figures 7.19 to 7.23 the D-mass is plotted for both the MC and the data samples, before and after the NN cuts.

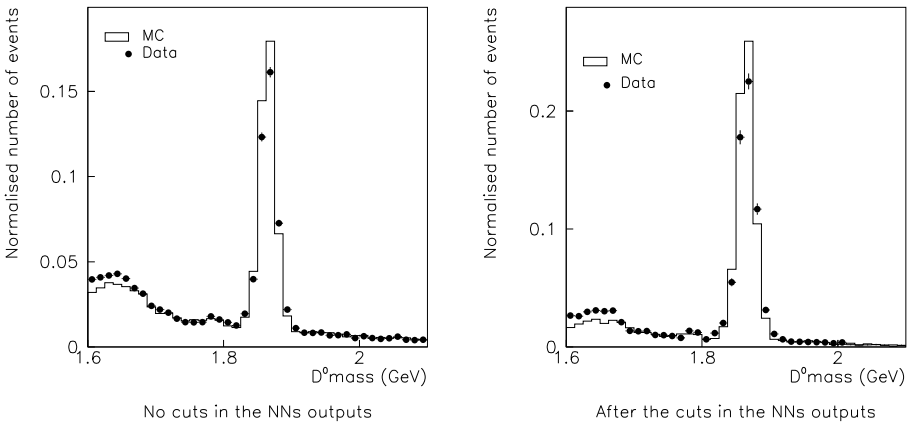

Figure 7.19: *Channel (a): Normalised D^0 mass distribution before and after the NN cuts for MC and data*

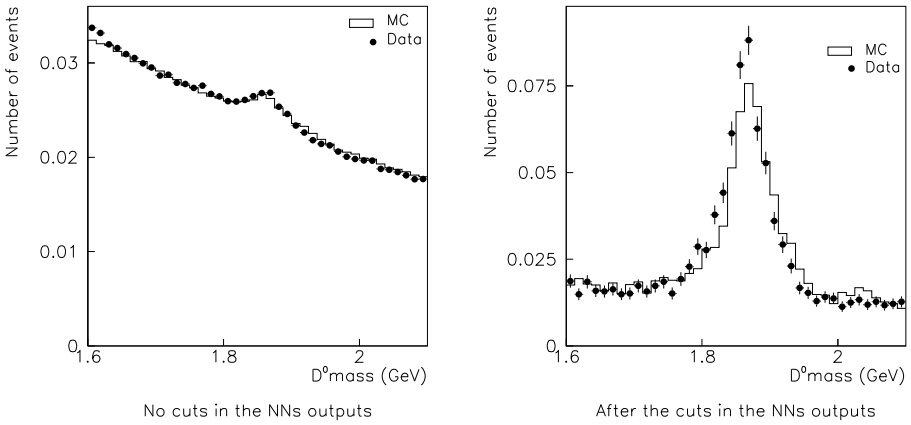

Figure 7.20: *Channel (b): Normalised D^0 mass distribution before and after the NN cuts for MC and data*

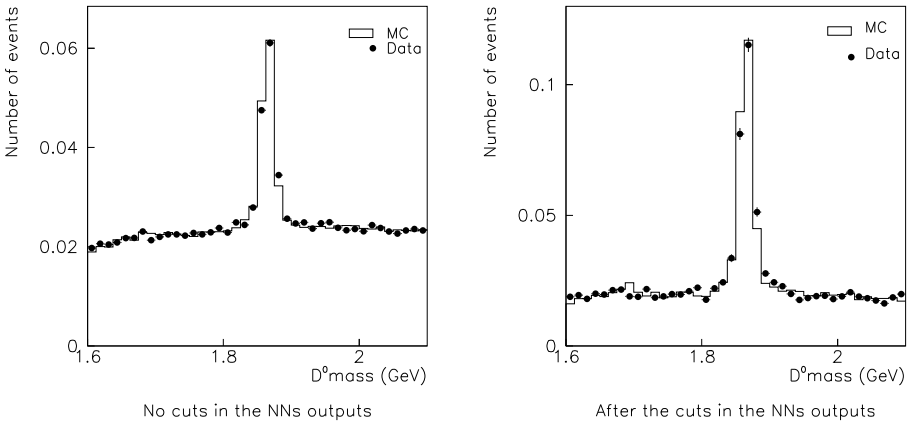

Figure 7.21: *Channel (c): Normalised D^0 mass distribution before and after the NN cuts for MC and data*

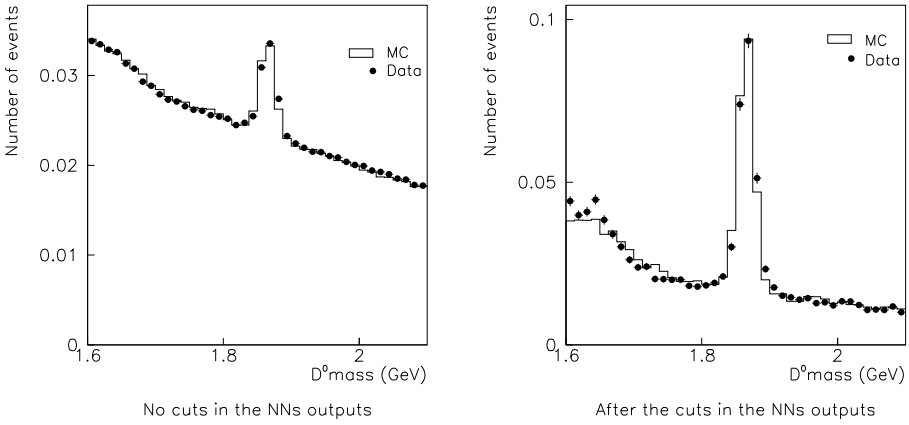

Figure 7.22: *Channel (d): Normalised D^0 mass distribution before and after the NN cuts for MC and data*

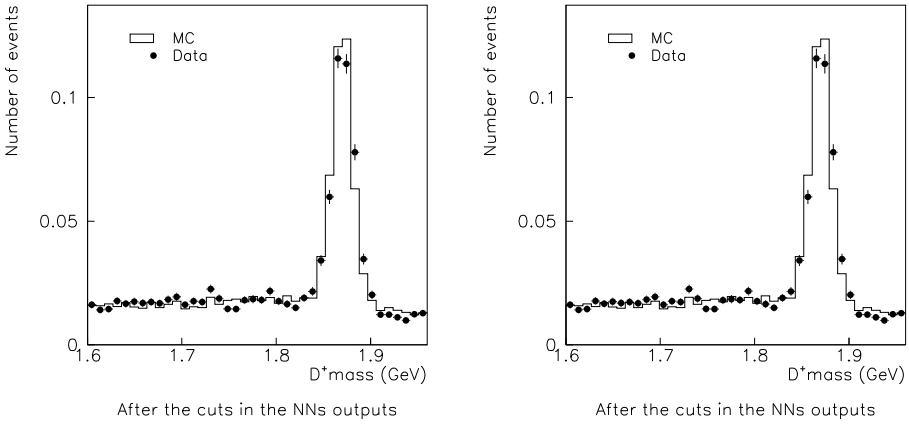

Figure 7.23: *Channel (e): Normalised D^+ mass distribution before and after the NN cuts for MC and data*

Resonable agreement exist (see Tables 7.8 and 7.9) for both data and MC in all the five channels and is improved after the reweighting of the MC data is done, as explained in the next section.

Channel	c_{MC}	uds_{MC}	b_{MC}	Total_{MC}	Total_{Data}
$D^{\star+} \to D^0 \pi_s^+$ $\hookrightarrow K^- \pi^+$	80%	10%	10%	4837 ± 70	5892 ± 77
$D^{\star+} \to D^0 \pi_s^+$ $\hookrightarrow K^- \pi^+ \pi^0$	67%	27%	6%	5748 ± 76	7437 ± 86
$D^{\star+} \to D^0 \pi_s^+$ $\hookrightarrow K^- \pi^+ \pi^- \pi^+$	62%	28%	10%	20035 ± 142	23893 ± 155
$D^0 \to K^- \pi^+$	33%	56%	10%	19548 ± 140	22667 ± 151
$D^+ \to K^- \pi^+ \pi^+$	50%	33%	17%	14219 ± 119	17616 ± 133
Total	58%	31%	11%	64387 ± 254	77505 ± 278

Table 7.8: *Number of candidates selected after NN and before mass window cuts. The number of MC events is rescaled to the corresponding one found in data. The quoted errors are statistical only*

Channel	c_{MC}	uds_{MC}	b_{MC}	Total_{MC}	Total_{Data}
$D^{\star+} \to D^0 \pi_s^+$ $\hookrightarrow K^- \pi^+$	87%	2%	11%	2628 ± 51	3027 ± 55
$D^{\star+} \to D^0 \pi_s^+$ $\hookrightarrow K^- \pi^+ \pi^0$	80%	12%	8%	1982 ± 46	2996 ± 48
$D^{\star+} \to D^0 \pi_s^+$ $\hookrightarrow K^- \pi^+ \pi^- \pi^+$	80%	10%	10%	3889 ± 62	4546 ± 67
$D^0 \to K^- \pi^+$	70%	18%	12%	3616 ± 60	4233 ± 65
$D^+ \to K^- \pi^+ \pi^+$	76%	9%	15%	2497 ± 46	3311 ± 50
Total	78%	12%	11%	14612 ± 120	18113 ± 134

Table 7.9: *Number of candidates selected after NN and mass window cuts. The number of MC events is rescaled to the corresponding one found in data. The quoteded errors are statistical only*

7.4 MC Reweighting

As one can observe in Table 7.2, the numbers are higher in data than in MC for all the channels. This discrepancy can not be explained due to statistical fluctuations.

Charm and bottom fragmentation were simulated in the Monte Carlo of the ALEPH experiment using the Peterson model (see Section 2.5.2). The momentum shapes of the c and b flavored mesons are controlled by the parameters ξ_c and ξ_b. These shapes are adjusted in the MC to reproduce the measured values of the mean scaled energies of weakly decaying c, and b hadrons, respectively.

Fitting the experimental curves observed by ALEPH, values of $< \xi_c >= (3.6 \pm 0.7) \cdot 10^{-2}$ and $< \xi_b >= (3.8 \pm 0.1) \cdot 10^{-3}$ have been extracted. The MC simulation has used larger values, $\xi_c^{MC} = 5.0 \cdot 10^{-2}$ and $\xi_b^{MC} = 4.5 \cdot 10^{-3}$. By reweighting the spectra, with a event-by-event weighting factor, the total number of events selected in the MC increases, as shown in Table 7.10. The new values are in good agreement with the ones from data.

Channel	MC events before reweighting	MC events after reweighting for ξ_c, ξ_b (N_D)	c_{MC}
(a)	2628 ± 52	3009 ± 55	78%
(b)	1982 ± 45	2307 ± 48	73%
(c)	3889 ± 62	4122 ± 64	75%
(d)	3616 ± 65	3975 ± 63	53%
(e)	2497 ± 46	2816 ± 53	67%
Total	15065 ± 122	16229 ± 127	68%

Table 7.10: *Number of D candidates selected before and after reweighting the MC sample. The percentage of charmed quarks selected is shown in the last column. The quoted errors are statistical only.*

In the case of the (b) channel, where the biggest discrepancy between MC and real data is observed, one makes a selection around the π^0 peak based on functions which depend on the 4-momentum, describing both the energy of and the angle between the two reconstructed photon candidates. The energy of the neutral pion played an important role also because only at energies below 10 GeV the two photon clusters were well separated in the calorimeter, with the error on the $\gamma\gamma$ opening angle being small compared to the error on the photon energies. Also, the form of the functions might not be accurate, i.e. the width of the signal and the position as a function of energy. When reconstructing the π^0 from the two γ's, differences between topologies in MC

and data could appear (merged or separate reconstructed daughter photons).

However, as long as the quark composition of the final selected sample is extracted directly from the data, for this analysis the number of produced D mesons is not important, only the percentage of D mesons decaying leptonically.

7.5 The Final Selection

One could use the Monte-Carlo information at the truth level, on the contamination of the signal to extract the number N_D^c. Another method has been applied for this analysis, which relies on the mass distribution shape of the signal.

The number of hemispheres, N_h, in the sample where a D meson candidate has been detected can be split (see Equation 5.6) in true D meson candidates, N_D, consisting of D mesons coming from prompt and non prompt charm quarks,

$$N_D = N_D^c + N_D^b \tag{7.3}$$

and fake D meson candidates, N_F, consisting of candidates coming from all the possible flavours:

$$N_F = N_F^c + N_F^b + N_F^{uds}. \tag{7.4}$$

The mass spectrum consists of a D-resonance plus background. The evaluation of the composition of the selected sample has to be made in two steps:

Firstly, the mass distribution gives the estimate of the combinatorial background channel by channel. This background is due to all present flavours: b, c and uds (see Figure B.5). A Gaussian fit is performed to the values observed in the chosen range ${M_D}^{min}$ to ${M_D}^{max}$, and a second order polynomial fit is performed to the combinatorial background (see Figure B.5).

The combinatorial background ($A_1 + A_2$, see Figure B.5) is parameterised by a second order polynomial function, and subtracted using a sideband analysis. A_1 is the combinatorial background lying under the D resonance. It is assumed to be smooth inside and outside the mass window, as seen in Figures 7.13 to 7.17. Integrating the fitted second order polynomial, between ${M_D}^{min}$ and ${M_D}^{max}$, one finds out the number of events A_1.

$$\begin{aligned} N_F &= A_1 \\ &= N_F^c + N_F^b + N_F^{uds}. \end{aligned} \tag{7.5}$$

A_3 is the fraction of events between ${M_D}^{min}$ and ${M_D}^{max}$ due to the resonance. Making a cut between ${M_D}^{min}$ and ${M_D}^{max}$, one remains with a number of events

$$\begin{aligned} N_h &= A_1 + A_3 \\ &= (N_D^c + N_F^c) + (N_D^b + N_F^b) + N_F^{uds}. \end{aligned} \tag{7.6}$$

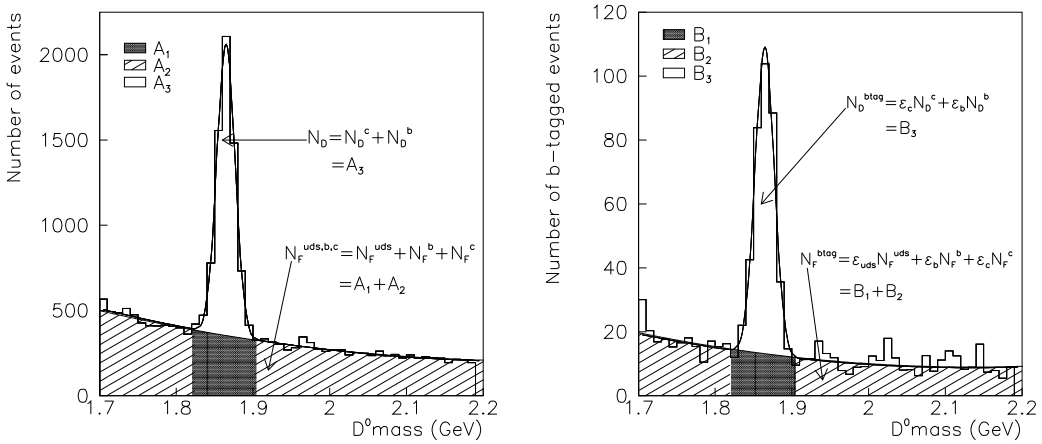

Figure 7.24: *Combined gaussian and second order polynomial fit in the D mass window (here channel d) to determine the background, for events without and with b-tagging. The histograms represent MC data.*

Subtracting Equation 7.5 from Equation 7.6, yields:

$$\begin{aligned} N_h - N_F &= A_3 \\ &= N_D^c + N_D^b. \end{aligned} \tag{7.7}$$

In the second step a loose lifetime b tag is applied in the opposite hemisphere. Using the lifetime tag, known in ALEPH software literature as QIPBTAG [51], the following efficiencies are expected:

$$\epsilon_c \approx 0.004 \quad \epsilon_{uds} < 0.001 \quad \epsilon_b \approx 0.20. \tag{7.8}$$

The number of candidates with the opposite hemisphere tagged by QIPBTAG can be written as:

$$\begin{aligned} N_h^{btag} &= B_1 + B_3 \\ &= \epsilon_c \times (N_D^c + N_F^c) + \epsilon_b \times (N_D^b + N_F^b) + \epsilon_{uds} \times N_F^{uds} \end{aligned} \tag{7.9}$$

which is dominated by the b contribution, as it should be for a b–tag selection. In this equation h stands for one hemisphere tagged. ϵ_c and ϵ_b are computed using MC modelling, and, based on previous ALEPH studies [52], they are assumed to be known at the level of 7% and 0.5% respectively.

As for the sample containing all the signal events, a combined Gaussian and second order polynomial fit is performed, which gives the combinatorial contribution in the b tagged sample:

$$\begin{aligned} N_F^{btag} &= B_1 \\ &= \epsilon_c \times N_F^c + \epsilon_b \times N_F^b + \epsilon_{uds} \times N_F^{uds} \end{aligned} \tag{7.10}$$

Subtracting Equation (7.10) from Equation (7.9), yields:

$$\begin{aligned} N_h^{btag} - N_F^{btag} &= B_3 \\ &= \epsilon_c \times N_D^c + \epsilon_b \times N_D^b. \end{aligned} \tag{7.11}$$

The system of Equations 7.7 and 7.11 can now be solved for N_D^b and N_D^c. The results presented in Tables 7.11 and 7.12 and the numbers of D candidates agree within the statistical errors.

$$N_D^b = \frac{(N_h^{btag} - N_F^{btag}) - \epsilon_c \times (N_h - N_F)}{\epsilon_b - \epsilon_c} \tag{7.12}$$

$$N_D^c = \frac{\epsilon_b \times (N_h - N_F) - (N_h^{btag} - N_F^{btag})}{\epsilon_b - \epsilon_c} \tag{7.13}$$

Channel	$N^c_{D\|MC}$	$N^b_{D\|MC}$	$N_{F\|MC}$
(a)	2585 ± 67	330 ± 54	94 ± 5
(b)	1308 ± 36	45 ± 48	954 ± 34
(c)	2580 ± 79	290 ± 45	1252 ± 25
(d)	2126 ± 79	374 ± 49	1475 ± 32
(e)	1780 ± 62	290 ± 36	746 ± 16
Total	10379 ± 149	1329 ± 105	4518 ± 56

Table 7.11: *Number of D candidates in MC (rescaled to data), after the final selection. The quoted errors are statistical ones, computed as described in Section 9.1.1.*

Channel	$N^c_{D\|Data}$	$N^b_{D\|Data}$	$N_{F\|Data}$
(a)	2690 ± 80	174 ± 53	163 ± 7
(b)	1784 ± 100	105 ± 76	1106 ± 26
(c)	2738 ± 103	351 ± 61	1456 ± 37
(d)	2267 ± 101	405 ± 60	1561 ± 41
(e)	2140 ± 82	331 ± 50	840 ± 23
Total	11619 ± 209	1366 ± 136	5126 ± 66

Table 7.12: *Number of D candidates in real data, after the final selection. The quoted errors are statistical ones, computed as described in Section 9.1.1.*

One can look at information from the MC, at the truth level (see Section 4.1.1), and trace the good reconstruction of the decay channel in each given event. The flavors of initial quarks from the $Z^0 \to q\overline{q}$ decay are also available. In Table 7.13, raw numbers of events selected in MC are presented. Presented

in the first column of Table 7.13 are values extracted when looking at the truth information in MC, $(N^c_{D|MC})_{truth}$. The second column of Table 7.13 shows calculated values of true D charm candidates, $N^c_{D|MC}$, following the same procedure as in real data. The good agreement between the two types of values is an argument for the correctness of the charm selection procedure.

Channel	$(N^c_{D\|MC})_{truth}$	$(N^c_{D\|MC})_{calculated}$	$(N^b_{D\|MC})_{truth}$	$(N^b_{D\|MC})_{calculated}$
(a)	4025 ± 63	4070 ± 106	519 ± 23	455 ± 74
(b)	2611 ± 51	2060 ± 121	235 ± 15	79 ± 86
(c)	4217 ± 65	4064 ± 124	456 ± 21	499 ± 78
(d)	3624 ± 60	3348 ± 124	589 ± 24	570 ± 75
(e)	2946 ± 54	2803 ± 98	457 ± 21	504 ± 63
Total	17423 ± 132	16345 ± 257	2256 ± 47	2107 ± 168

Table 7.13: *Number of c and b true D candidates in MC (before rescaling to data), after the final selection. For values extracted from the truth level, the quoted statistical errors are computed as square root of the values. For calculated values, the quoted statistical errors are computed as described in Section 9.1.1.*

An overview on the selected charmed samples of events is presented in Table 7.14, based on information collected from Tables 7.9 to 7.12. The purities of

Channel	$N_{D\|MC(resc)}$ see Table 7.10	$N^c_{D\|MC(resc)}$ see Table 7.11	$\mathcal{P}_{MC}$	$N_{D\|Data}$ see Table 7.9	$N^c_{D\|Data}$ see Table 7.12	$\mathcal{P}_{Data}$
(a)	3009 ± 55	2585 ± 67	86%	3027 ± 55	2690 ± 80	88%
(b)	2307 ± 48	1308 ± 36	57%	2996 ± 55	1784 ± 100	60%
(c)	4122 ± 64	2580 ± 79	62%	4546 ± 67	2738 ± 103	60%
(d)	3975 ± 63	2126 ± 79	53%	4233 ± 65	2267 ± 101	54%
(e)	2816 ± 53	1780 ± 62	63%	3311 ± 58	2140 ± 82	65%
Total	16229 ± 127	10379 ± 149	65%	18113 ± 135	11619 ± 209	65%

Table 7.14: *Overview of the charm selection procedure in real data, at the working point. The quoted errors are statistical only.*

both the MC and real data samples are calculated as:

$$\mathcal{P} = \frac{N^c_D}{N_D} \tag{7.14}$$

The purities in MC and in real data have a relative variation of about 5%.

Their difference is due to the fact that a part of the selected charm events are made out of fake D candidates (N_F^c).

Because the charm selection procedure works correctly for MC (see Table 7.13) and because the Monte Carlo simulation correctly describes the data (see Chapter 4), each step of the charm selection procedure in real data was checked using MC samples rescaled to the real data samples. The numbers important hereafter when refering to the charm selection are summarised in Table 7.15. These represent true charmed candidate selected in real data sample and in the MC sample without rescaling.

Channel	$N^c_{D\|Data}$	$N^c_{D\|MC}$
(a)	2690 ± 80	4025 ± 63
(b)	1784 ± 100	2611 ± 51
(c)	2738 ± 103	4217 ± 65
(d)	2267 ± 101	3624 ± 60
(e)	2140 ± 82	2946 ± 54
Total	11619 ± 209	17423 ± 132

Table 7.15: *Number of charmed true D candidates in real data and in MC samples (before rescaling to data). The quoted statistical errors are computed as described in Section 9.1.1.*

Chapter 8

The (D, l) sample

In the event hemisphere opposite to the one where a highly-energetic reconstructed charmed meson has been found, leptons are identified and counted. The identification of the leptons found by the detector is performed using standard cuts [50]. To find the leptons from a charm quark one exploits the correlation between the electrical charges of the lepton and the parent charm quark.

8.1 Lepton Detection with the ALEPH Detector

Only two leptons, electrons and muons, are sufficiently light to be produced by the decay of a charm quark. Therefore, in this analysis, the word *lepton* means an electron or a muon, but not a tau.

All leptons selected in this analysis are required to have a high momentum, greater than 2 GeV, and a high transverse momentum p_T, with respect to the jet containing them, of 0.5 GeV. This p_T is calculated by including the lepton in the reconstructed jet (see Section 2.5).

In the ALEPH experiment, the electron and the muon follow different identification procedures. This is mainly due to the fact that the muon has a mass which is two orders of magnitude larger than the electron (see Table 2.1). Therefore, the electrons interact with the detector material differently from the muons. For the considered range of lepton momenta, the electrons are trapped inside the detector because of their interactions, while the muons can traverse the entire ALEPH detector and exit it.

8.1.1 Electrons

The electrons are identified using the ionisation loss dE/dx in the TPC, as well as the information of the shower profile in the ECAL. A charged particle has been defined as an electron, when:

- The ionisation power of the particle in the TPC, assuming it was an electron, was $R_I > -2.0$ (see Equation 3.4).

- The transverse shape of the shower created by the particle in the ECAL satisfied $R_T > -1.6$ (see Equation 3.5). The longitudinal mean position of the energy deposit of the particle in the ECAL was $-1.8 < R_L < 3.0$ (see Equation 3.7). Electrons have the tendency to deposit their energy in the first layers of the ECAL. As seen in Figure 8.1, these two cuts enable a good separation of electrons and charged hadrons.
- The momentum of the track was $p > 2.0\,\mathrm{GeV}$.

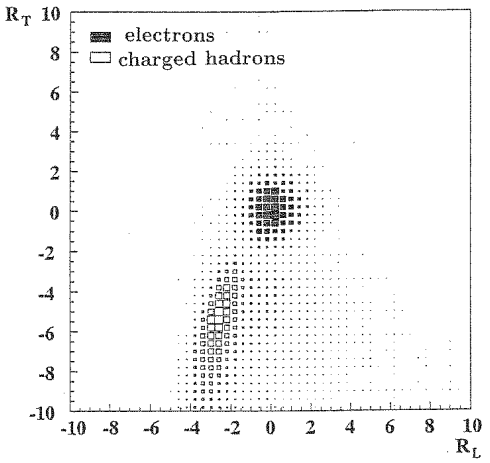

Figure 8.1: *R_T versus R_L for Monte Carlo simulated electrons and charged hadrons*

Electrons and pions could be separated with a high efficiency because most pions interact marginally only in the ECAL's 22 radiation lengths, while all the electrons did. However, some pion contamination exists in the region where electrons had a low interaction with the ECAL. By using the information on the shape of the electromagnetic shower and cutting on the variable E_4/p in Equation 3.5, one could reduce the pion contamination to the level of 10^{-3} at 10 GeV. At an energy of 5 GeV the hadron contamination, for an electron detection efficiency greater than 95%, was less than 3×10^{-3}. By combining this information with dE/dx from the TPC one could lower the hadron contamination of the electron sample to 10^{-3}.

8.1.2 Muons

The muons were identified by extrapolating the tracks from the TPC and using information from the HCAL and the muon chambers. A HCAL plane was *expected* to fire if the extrapolated track intersected it within an active region. The plane was considered as *fired* if at least one cluster lied within the extrapolated track. Regarding the signals in the HCAL, a charged particle with a momentum $p > 2.5\,\mathrm{GeV}$ was declared as a penetrating muon when:

- $N_{fir}/N_{exp} \geq 0.4$
- $N_{exp} \geq 10$

- $N_{10} > 4$

where N_{exp}, N_{fir} and N_{10} were the number of *expected* planes, the number of *fired* planes among the last *ten* planes expected to be fired, associated to the track, respectively. The final condition was that the track had at least one channel hit in the muon chambers.

The muons were identified with an efficiency of 86%. The probability of misidentifying a hadron as a muon, from a hadronic Z^0 decay, and the probability to have a muon generated by a kaon or pion, gave a 0.8% contamination of the muon sample. If a track was identified as both an electron and a muon, it was taken as a muon.

8.1.3 Neutrinos

The presence of neutrinos is signaled in ALEPH by the presence of a $e^{\pm}$, $\mu^{\pm}$ lepton. Neutrinos are not detected in ALEPH due to the fact that they interact via the weak force. Their momentum and energy are calculated from momentum and energy conservation laws.

8.2 Corrections to the Number of Leptons Generated by Monte Carlo

Production of Monte Carlo simulated events started in 1985. Since that time knowledge about the values of some of the parameters used has improved. In order to take into account the changes in their values, a rescaling of the selected MC events was applied when using the earlier generated events.

The quantities to be rescaled, q_{resc}, affecting the lepton selection, are presented in Table 8.1. Here q_{resc}^{old} is the old value of the given quantity, as it was implemented in the MC simulation, and q_{resc}^{new} is the newest experimental value for q_{resc}. q_{resc}^{new} was used in this analysis to correct the MC data.

No.	q_{resc}	q_{resc}^{old}	q_{resc}^{new}
1	$BR(b \to l)$	10.35 %	10.67%
2	$BR(b \to c \to l)$	9.30%	8.07%
3	$BR(b \to \overline{c} \to l)$	1.46%	1.62%

Table 8.1: *MC-quantities updated in this analysis to the newest experimental values*

If one denotes by:

- $f_{D,l}^{c}$ - the fraction of lepton candidates of interest for measuring the BR (events where true mesons D accompanied by true prompt leptons l have been detected).

- f_{resc} - the fraction of lepton candidates in the old implementation of the MC quantity q_{resc}, which has to be rescaled.
- f_{rest} - the fractional sum of all the other present lepton candidates (other than $f^c_{D,l}$ and f_{resc}).

The quantity $f^c_{D,l}$ shifts from the old value, given by Equation 8.1, to the new one, as given by Equation 8.2:

$$f^{c,old}_{D,l} = 1 - f_{rest} - f_{resc} \tag{8.1}$$

$$f^{c,new}_{D,l} = 1 - f_{rest} - f_{resc} \cdot \frac{q^{new}_{resc}}{q^{old}_{resc}} \tag{8.2}$$

8.3 Incorrect Assignment of the D Charge

Following the information from Tables 5.1 and 5.2, the decay of a $c\overline{c}$ pair into a lepton and a D–meson is signed by a $(l^+,\ D^-)$ or a (l^-, D^+) pair, which corresponds to a $(l^+,\ K^+)$ or (l^-, K^-) pair:

$$\begin{array}{rrcl} & \overline{c} \rightarrow & D^-/\overline{D}^0 & \rightarrow K^+ \\ & c \rightarrow & W^+ & \rightarrow l^+ \\ \text{or :} & & & \\ & c \rightarrow & D^+/D^0 & \rightarrow K^- \\ & \overline{c} \rightarrow & W^- & \rightarrow l^- \end{array} \tag{8.3}$$

While the charge assignment of the leptons is relatively straightforward, an uncertainty arises from the fact that the charge of the K could be incorrectly assigned, leading to $(l^+,\ D^+)$ or (l^-, D^-) pairs. As an example, this kind of mis-assignment happens in events where the track reconstruction was poor, and a pion was misidentified as a kaon. This background has a combinatorial nature, and it is treated together with the other combinatorial backgrounds, which are mainly due to *uds* initial quarks.

The events used to compute the branching ratio (see Equation 5.2) are those where both the lepton and the D candidates charge, and flavour, were correctly assigned, $N^c_{D,l}$. If the lepton and its electrical charge were correctly assigned, and if the electrical charge of the D meson (deduced from the charge of the kaon candidate from the meson decay, as shown in Equation 8.3) was incorrectly assigned, the lepton candidate is rejected from the category $N^c_{D,l}$ because the pair does not fall in the $(l^+,\ D^+)$ or (l^-, D^-) type.

An incorrect assignment of the electrical charge of the D meson candidate gives rise to a systematic uncertainty in selecting the lepton candidates. As classified in Section 9.2, this is a Type I error, where, even if correctly identified, the lepton candidate is rejected. This is explained in more detail below.

It is possible that the charge of a D meson was incorrectly assigned, even if the charm flavor of the initial quark was correctly identified. These sort of

events, even if could be part of $N^c_{D,l}$ class, are considered background in the second step of the analysis, which is related to leptons, in correlation with the mesons charges (see Section 9.2.1).

Misassignment of the D-meson charge can be reduced using special trained NN. The NN training used for the distinction between *uds* and *c* quarks has been described in Chapter 7. The MC background sample for this NN training consisted of *uds* quarks, and *c* quarks which had the charge of the reconstructed meson incorrectly assigned. The composition of this background samples is shown in Table 8.2 for each individual channel. Thus, thought not mentioned explicitly in Chapter 7, the NN was trained to do a distinction between *c* and *c* quarks which had the charge of the reconstructed meson incorrectly assigned.

Background for NN training	(a)	(b)	(c)	(d)	(e)
c with incorrect assignment of the charge, in %	13	13	16	15	26
uds, in %	87	87	84	85	74

Table 8.2: *The composition of MC background sample used as input for the NN training. This sample consisted of c-events, with an incorrect assignment of the charge, and uds-events.*

In Table 8.3 the rejection power of the NN, for the *c* quarks which had the charge of the reconstructed meson incorrectly assigned, is shown.

As one can see in Table 8.3, channel (*e*) is among the channels with the largest percentage of events which have the charge of the D meson mis-assigned, both before and after the NN selection. This behavior can be explained if the kaon candidate is interchanged with one of the two pions which have opposite charge to the charge of the kaon, is taken instead. Even if the assignment of the D candidate to the charm events class is still valid, this interchange flips the assigned electrical charge of the meson candidate, so that it becomes incorrect. For channel (*e*), the fraction of the mis-assigned charm events used in the training sample was the highest, with respect to the other analysed channels (see Table 8.2). An improvement of 178% was obtained in the purity of the charm events with the electrical charge correctly assigned, after the NN selection.

The situation for channel (*c*) is similar to the one of channel (*e*), in the sense that two pions with electrical charges opposite to the charge of the kaon exist among the decay products. However, if the kaon candidate is interchanged with a pion, only the interchanging of two out of the three

Channel	(a)	(b)	(c)	(d)	(e)
c with charge correctly assigned, before NN selection, in %	90	71	80	89	55
c with charge correctly assigned, after NN selection, in %	99	99	97	99	98

Table 8.3: *Influence of the NN selection on the number of c-events with the electrical charge correctly assigned, shown for each analysed channel, as given by the MC sample*

present pions changes the electrical charge of the meson candidate: If the kaon is interchanged with the pion having the same electrical charge, the resulting electrical charge of the D candidate remains correctly assigned, as does its assignment to the charm events class. After the NN selection, an improvement of 121% is observed in the purity of the charm events with the electrical charge correctly assigned. The NN is not as effective as for channel (e), in respect of removing the charm events with the sign of the electrical charge incorrectly assigned. This is because the NN cut optimises the purity of the signal (charm events with the sign of the electrical charge correctly assigned) with respect to both the charm with incorrect assignment of the electrical charge and the combinatorial (mainly uds) background. In summary, by training the NN to reject the two types of combinatorial background together, one does not have control of the purity of the sample with respect to each of these backgrounds separately.

After applying the NN cuts the percentage of the charm with the electrical charge correctly assigned increased. This increases the confidence in a method of lepton selection based on the charge of the charmed quark.

8.4 Principle of Selection

The number of events $N_{h,L}$, where leptons were identified in the hemisphere opposite to the charmed meson candidate (see Section 5.1), can be written as the sum of signal events ($N^c_{D,l}$) and background events ($N^{fake}_{h,L}$):

$$N_{h,L} \;=\; N^c_{D,l} + N^{fake}_{h,L} \tag{8.4}$$

The searched signal events, $N^c_{D,l}$, contain a D candidate and a lepton candidate, the two of them having opposite electrical charge. In order to identify the background, one splits the lepton candidates $N_{h,L}$ in two distinct classes:

$$N_{h,L} \;=\; N^{o.c.}_{h,L} + N^{s.c.}_{h,L} \tag{8.5}$$

The class where the D–candidate and the lepton have opposite electrical charge is denoted by $N^{o.c.}_{h,L}$. It contains the searched leptons, $N^{c}_{D,l}$, coming from charm decays (see Section 2.6.1):

$$N^{o.c.}_{h,L} = N^{c}_{D,l} + N^{fake,\ o.c.}_{h,L} \tag{8.6}$$

The class where the D–candidate and the lepton have the same electrical charge is denoted by $N^{s.c.}_{h,L}$:

$$N^{s.c.}_{h,L} = N^{fake,\ s.c.}_{h,L} \tag{8.7}$$

The signal events $N^{c}_{D,l}$ enter only in the $N^{o.c.}_{h,L}$ class (see Section 2.6.1), while the background events tend to be equally distributed between the $N^{o.c.}_{h,L}$ and $N^{s.c.}_{h,L}$ classes:

$$\begin{cases} N^{o.c.}_{h,L} = N^{c}_{D,l} + \frac{1}{2} \cdot N^{fake}_{h,L} \\ N^{s.c.}_{h,L} = \frac{1}{2} \cdot N^{fake}_{h,L} \end{cases} \tag{8.8}$$

In summary, in a first approach, the number of lepton signal events is given by the difference between the number of events where the lepton candidates have opposite charge to the detected D candidates and the number of events where they have the same charge (see the first three columns of Table 8.5):

$$N^{c}_{D,l} = N^{o.c.}_{h,L} - N^{s.c.}_{h,L} \tag{8.9}$$

However, small corrections $\Delta N_{h,L}$ remain to be applied to take into account that the background events may be unequally distributed between the two classes. Equation 8.9 now becomes:

$$N^{c}_{D,l} = N^{o.c.}_{h,L} - N^{s.c.}_{h,L} + \Delta N^{fake}_{h,L} \tag{8.10}$$

In the final result these corrections turn out to be very small for channels (a), (b), (e), or small, of the order of 1σ, for channels (c) and (d) (see Table 8.25). In order to extract the value of these corrections, the value of $N^{fake}_{h,L}$ has to be computed. One can write:

$$N^{fake}_{h,L} = N^{b}_{D,l} + N^{b,c}_{D,f} + N^{b,c}_{F,l} + N^{b,c,uds}_{F,f} \tag{8.11}$$

since the lepton background consist of events where:

1. $N^{c}_{F,l}$: events originating from a c quark where the reconstructed meson was fake and the lepton is true and prompt.

2. $N^{c}_{D,f}$: events originating from a c-quark where the reconstructed lepton was either fake (incorrect assignment of a K, π or other particle) or a non-prompt lepton (originating from a K, π, γ or other particle).

3. $N^{c}_{F,f}$: events originating from a c-quark where both the D meson and the lepton were not correctly reconstructed.

4. $N^{b}_{D,l}$: events from a $b \to l$, $b \to c \to l$ and $b \to \overline{b} \to \overline{c} \to l$ decays, where the reconstructed meson was true (D).

5. $N^{b}_{F,l}$: events originating from a b-quark where the reconstructed meson was fake (F).

6. $N^{b}_{D,f}$: events originating from a b quark where the reconstructed lepton was either fake (incorrect assignment of a K, π or other particle) or a non-prompt lepton (originating from a K, π, γ or other particle).

7. $N^{b}_{F,f}$: events originating from a b-quark where both the D-meson and the lepton were not correctly reconstructed.

8. $N^{uds}_{F,f}$: events originating from a uds quark where both the D-meson and the lepton were not correctly reconstructed.

The corrections to the lepton background have to be derived based on MC studies. They are further denoted by $\Delta N_{h,L}$. Taking them into account, the system of Equations 8.8 becomes:

$$\begin{cases} N^{o.c.}_{h,L} &= \frac{1}{2} \cdot (N^{fake}_{h,L} + \Delta N_{h,L}) + N^{c}_{D,l} \\ N^{s.c.}_{h,L} &= \frac{1}{2} \cdot (N^{fake}_{h,L} - \Delta N_{h,L}) \end{cases} \tag{8.12}$$

The corrections to the lepton background, $\Delta N^{fake}_{h,L}$, come from each of the right-hand terms of Equation 8.11:

$$\Delta N_{h,L} = \Delta N^{b,c}_{D,f} + \Delta N^{b}_{D,l} + \Delta N^{b,c}_{F,l} + \Delta N^{b,c,uds}_{F,f} \tag{8.13}$$

These effects are small and one has to discuss them with respect to their paring with D meson candidates having opposite and same sign electrical charge. One makes these corrections with the MC help with results presented in the end of this chapter (see Table 8.25). They are very small for channels (a), (b) and (e) and small (order of $2 \cdot \sigma$) for channels (c) and (d).

8.5 Lepton Sample

Table 8.4 shows the number of lepton candidates with opposite or same charge selected in MC and in data for each individual channel. For a better comparison, in the last two columns the numbers in MC are rescaled to the data luminosity, based on the total number of $Class$ 16 events available in data and MC. Within the statistical errors the number of lepton candidates calculated for the MC data are in good agreement with the real data.

Channel	$N^{o.c.}_{Data}$	$N^{s.c.}_{Data}$	$N^{o.c.}_{MC}$	$N^{s.c.}_{MC}$	$N^{o.c.}_{MC(resc)}$	$N^{s.c.}_{MC(resc)}$
(a)	303±17	85±9	552±23	117±11	350±23	74±9
(b)	310±18	67±8	400±20	85±9	254±16	54±7
(c)	423±21	122±11	661±26	174±13	419±20	110±10
(d)	439±21	157±13	686±26	252±16	435±21	160±13
(e)	347±19	89±9	485±22	149±12	308±18	94±10
Average	1822±43	509±23	2784±53	777±28	1766±42	492±22

Table 8.4: *Number of lepton candidates with same and opposite charge before applying the correction $\Delta N_{h,L}$. These numbers are given for the data, the MC and the MC rescaled to data.*

According to Equation 8.9, first estimators on the number of lepton candidates from charmed quark decays can be extracted. These values do not contain the correction $\Delta N_{h,L}$ and are shown in the first two columns of Table 8.5, for data and MC. It must be mentioned that until this step the MC serves only as comparison to the data.

The total numbers of lepton candidates are presented in the last column of Table 8.5, because the further lepton percentages, from Tables 8.7 to 8.25, are with respect to these numbers.

Channel	$(N^{o.c.} - N^{s.c.})_{Data}$	$(N^{o.c.} - N^{s.c.})_{MC}$	$(N^{o.c.} - N^{s.c.})_{MC\|resc}$	$(N^{o.c.} + N^{s.c.})_{MC}$
(a)	218± 19	435± 25	276± 25	424± 25
(b)	243± 20	315± 22	200± 17	308± 22
(c)	301± 24	487± 29	309± 22	529± 29
(d)	282± 25	434± 30	275± 25	595± 30
(e)	258± 21	336± 25	214± 21	402± 25
Average	1302± 49	2007± 60	1274± 47	2258± 60

Table 8.5: *Various combinations of the signal with opposite charge and the signal with same charge, as retrieved from Table 8.4*

8.6 Corrections of the Lepton Background

As mentioned in Section 8.4 the lepton background should at first order be equally distributed between lepton with same charge and opposite charge compared to the meson. At this point of the analysis it is important to estimate if a correction has to be applied to this equal distribution. This correction, called $\Delta N_{h,L}$ (see Equation 8.12), can be derived using the MC sample and by dividing the selected events into classes, according to their properties listed above. This is shown in Table 8.6 for all channels, where the upper–most left number (1290) corresponds to the searched signal, while the other numbers give the different contributions to the background. Splitting the lepton candidates into these classes has the advantage that MC-implemented quantities (q^{old}_{resc}) (see Table 8.1) can be easily rescaled to the most recent experimentally determined values (see Section 8.2). These corrections are further discussed in the following subsections and their values from the MC data are presented.

Lepton origin	True D meson		Fake D meson	
	$\pm$ and $\mp$	$++$ and $--$	$\pm$ and $\mp$	$++$ and $--$
$c \to l$	1274	1	102	26
$c \to fake$	99	78	13	9
fragmentation in c events	70	69	6	9
$b \to l$	39	165	27	31
$b \to c \to l$	75	24	10	11
$b \to \overline{c} \to l$	0	18	1	6
$b \to fake$	8	15	5	3
fragmentation in b events	1	2	0	1
uds	9	11	15	20
$Total$	1575	383	179	116

Table 8.6: *Splitting of the total MC sample (rescaled to data) according to the authenticity of the D meson candidate and the origin of the lepton candidate.*

8.6.1 Corrections due to Fake Leptons ($\Delta N^{b,c}_{D,f}$)

One can imagine to have n_f charm candidates, where the sign of the electrical charge flipped to the opposite one during the process of D reconstruction, and n_s charm candidates, where the sign of the electrical charge remained the same. If the charge of the lepton candidate is incorrectly reconstructed, with the probability p_w, and correctly reconstructed with the probability $p_r = 1 - p_w$, one can write:

$$\begin{aligned} N^{o.c}_{D,f} &= n_s \cdot p_r + n_f \cdot p_w \\ N^{s.c}_{D,f} &= n_s \cdot p_w + n_f \cdot p_r \end{aligned} \tag{8.14}$$

When a fake prompt-lepton candidate is identified, it has an equal probability to be reconstructed as positive electrical charge or negative. Therefore, one has:

$$\begin{aligned} N^{o.c}_{D,f} &= 0.5 \cdot (n_s + n_f) \\ N^{s.c}_{D,f} &= 0.5 \cdot (n_s + n_f) \end{aligned} \tag{8.15}$$

$b \to F$	$\frac{N^{o.c.}_{h,L\|MC}}{(N^{o.c.}+N^{s.c})_{MC}}$ in %	$\frac{N^{s.c.}_{h,L\|MC}}{(N^{o.c.}+N^{s.c})_{MC}}$ in %	$\Delta\frac{N^{b}_{D,F\|MC}}{(N^{o.c.}+N^{s.c})_{MC}}$ in %
(a)	0.45 ± 0.26	0.45 ± 0.26	0.00 ± 0.36
(b)	0.00 ± 0.00	0.21 ± 0.21	0.21 ± 0.21
(c)	0.00 ± 0.00	0.48 ± 0.24	0.48 ± 0.24
(d)	0.64 ± 0.26	0.64 ± 0.26	0.00 ± 0.37
(e)	0.32 ± 0.22	1.26 ± 0.44	0.95 ± 0.50
Average	0.28 ± 0.09	0.61 ± 0.44	0.33 ± 0.16

Table 8.7: *Corrections* $\Delta N^{b}_{D,F|MC}$.

$c \to F$	$\frac{N^{o.c.}_{h,L\|MC}}{(N^{o.c.}+N^{s.c})_{MC}}$ in %	$\frac{N^{s.c.}_{h,L\|MC}}{(N^{o.c.}+N^{s.c})_{MC}}$ in %	$\Delta\frac{N^{c}_{D,F\|MC}}{(N^{o.c.}+N^{s.c})_{MC}}$ in %
(a)	4.63 ± 0.81	3.89 ± 0.75	-0.74 ± 1.10
(b)	3.92 ± 0.88	3.92 ± 0.88	0.00 ± 1.25
(c)	4.55 ± 0.72	2.87 ± 0.58	-1.68 ± 0.92
(d)	4.48 ± 0.67	2.67 ± 0.65	-1.81 ± 0.86
(e)	3.79 ± 0.76	4.11 ± 0.79	0.32 ± 1.09
Average	4.27 ± 0.35	3.49 ± 0.32	-0.78 ± 0.47

Table 8.8: *Corrections* $\Delta N^{c}_{D,F|MC}$.

Tables 8.7 and 8.8 show that, for both MC b and c quarks, the fraction of lepton candidates paired to a well reconstructed D meson tend to be equally split between opposite and same charge samples, $N^{o.c}_{D,F} = N^{s.c}_{D,F}$. The corrections found in the MC are consistent with zero, within the error range, for all the analysed channels.

When the leptons are true, but non prompt, they mainly originate from the fragmentation processes $b \to q \to l$ and $c \to q \to l$. (The electrons might also be one of the electrons from photons conversion.) During the fragmentation, the sign of the electrical charge for the initial quark may, or may not, flip the sign. Therefore, the non–prompt fake lepton candidates paired to a well reconstructed D meson, $N_{D,non\ prompt}$, tend to be equally distributed between same and opposite charge samples, $N^{s.c}_{D,F} = N^{o.c}_{D,F}$, for D mesons originating both from b quarks (see Table 8.9) and c quarks (see Table 8.10).

$b \to$ *non prompt*	$\frac{N^{o.c.}_{h,L\|MC}}{(N^{o.c.}+N^{s.c})_{MC}}$ in %	$\frac{N^{s.c.}_{h,L\|MC}}{(N^{o.c.}+N^{s.c})_{MC}}$ in %	$\Delta\frac{N^{b}_{D,non\ prompt\|MC}}{(N^{o.c.}+N^{s.c})_{MC}}$ in %
(a)	0.00 ± 0.00	0.15 ± 0.15	0.15 ± 0.15
(b)	0.00 ± 0.00	0.00 ± 0.00	0.00 ± 0.00
(c)	0.12 ± 0.12	0.00 ± 0.00	-0.12 ± 0.12
(d)	0.11 ± 0.11	0.00 ± 0.00	-0.11 ± 0.11
(e)	0.00 ± 0.00	0.00 ± 0.00	0.00 ± 0.00
Average	0.04 ± 0.03	0.03 ± 0.03	-0.01 ± 0.04

Table 8.9: *Corrections* $\Delta N^{b}_{D,non\ prompt|MC}$.

$c \to$ *non prompt*	$\frac{N^{o.c.}_{h,L\|MC}}{(N^{o.c.}+N^{s.c})_{MC}}$ in %	$\frac{N^{s.c.}_{h,L\|MC}}{(N^{o.c.}+N^{s.c})_{MC}}$ in %	$\Delta\frac{N^{c}_{D,non\ prompt\|MC}}{(N^{o.c.}+N^{s.c})_{MC}}$ in %
(a)	4.04 ± 0.76	2.84 ± 0.64	-1.20 ± 1.00
(b)	2.26 ± 0.68	3.30 ± 0.81	1.03 ± 1.06
(c)	2.63 ± 0.55	3.35 ± 0.62	0.72 ± 0.83
(d)	3.52 ± 0.60	2.98 ± 0.56	-0.53 ± 0.82
(e)	2.21 ± 0.58	2.37 ± 0.60	1.16 ± 0.84
Average	2.93 ± 0.29	2.97 ± 0.29	0.03 ± 0.41

Table 8.10: *Corrections* $\Delta N^{c}_{D,non\ prompt|MC}$.

One can conclude that the correction due to fake prompt lepton candidates, $\Delta N^{b,c}_{D,f}$, have a value consistent with zero within the error range for all the analysed channels, as expected in Equations 8.8. This is summarised in Tables 8.11 and 8.12.

8.6.2 Corrections due to b–D candidates ($\Delta N^{b}_{D,l}$)

When a D candidate coming from a $Z^0 \to b\overline{b}$ decay is reconstructed in one hemisphere, in the opposite hemisphere a b quark also has to be reconstructed (see Section 5.1). The b quark produced the charmed D meson via a $b \to c$, or a $b \to \overline{b} \to \overline{c}$ process. Since $BR(b \to c) > BR(b \to \overline{b} \to \overline{c})$, in the hemisphere where one detects the charmed anti-quark $\overline{c}$, events of the type $\overline{b}^{+1/3} \to \overline{c}^{\,-2/3}$ are dominating, where the superscript is the quark charge. This implies that, in the N^{b}_{D} sample, events where the charge of the charm candidate reverses the sign are more likely to be reconstructed.

The b quark can decay leptonically via $b \to l$, $b \to c \to l$ or $b \to \overline{b} \to \overline{c} \to l$ processes. Therefore, the correction $\Delta N^{b}_{D,l}$ consists of three terms:

$$\Delta N^{b}_{D,l} \;=\; \Delta N^{b}_{D,l|b\to l} + \Delta N^{b}_{D,l|b\to c\to l} + \Delta N^{b}_{D,l|b\to\overline{c}\to l} \qquad (8.16)$$

If one had a $b^{-1/3} \to l^{-}$ decay in the first hemisphere, it would correspond

$b \to f$	$\frac{N^{o.c.}_{h,L\|MC}}{(N^{o.c.}+N^{s.c})_{MC}}$ in %	$\frac{N^{s.c.}_{h,L\|MC}}{(N^{o.c.}+N^{s.c})_{MC}}$ in %	$\Delta\frac{N^{b}_{D,f\|MC}}{(N^{o.c.}+N^{s.c})_{MC}}$ in %
(a)	0.45 ± 0.26	0.60 ± 0.30	0.15 ± 0.40
(b)	0.00 ± 0.00	0.21 ± 0.21	0.21 ± 0.21
(c)	0.12 ± 0.12	0.48 ± 0.24	0.36 ± 0.27
(d)	0.75 ± 0.28	0.64 ± 0.26	-0.11 ± 0.39
(e)	0.32 ± 0.22	1.26 ± 0.44	0.95 ± 0.50
Average	0.04 ± 0.03	0.03 ± 0.03	-0.01 ± 0.04

Table 8.11: *Corrections $\Delta N^{b}_{D,f|MC}$, when b decays to a l directly, or via a c quark.*

$c \to f$	$\frac{N^{o.c.}_{h,L\|MC}}{(N^{o.c.}+N^{s.c})_{MC}}$ in %	$\frac{N^{s.c.}_{h,L\|MC}}{(N^{o.c.}+N^{s.c})_{MC}}$ in %	$\Delta\frac{N^{c}_{D,f\|MC}}{(N^{o.c.}+N^{s.c})_{MC}}$ in %
(a)	8.67 ± 1.09	6.73 ± 0.97	-1.94 ± 1.46
(b)	6.67 ± 1.09	6.73 ± 0.97	-1.94 ± 1.46
(c)	7.19 ± 0.89	6.23 ± 0.84	-0.96 ± 1.22
(d)	8.00 ± 0.89	5.65 ± 0.75	-2.35 ± 1.16
(e)	6.00 ± 0.94	6.48 ± 0.98	0.47 ± 1.36
Average	7.21 ± 0.44	6.46 ± 0.43	-0.75 ± 0.61

Table 8.12: *Corrections $\Delta N^{c}_{D,f|MC}$.*

$b \to l$	$\frac{N^{o.c.}_{h,L\|MC}}{(N^{o.c.}+N^{s.c})_{MC}}$ in %	$\frac{N^{s.c.}_{h,L\|MC}}{(N^{o.c.}+N^{s.c})_{MC}}$ in %	$\Delta\frac{N^{b}_{D,l\|b\to l\|MC}}{(N^{o.c.}+N^{s.c})_{MC}}$ in %
(a)	1.64 ± 0.49	7.32 ± 1.01	5.68 ± 1.12
(b)	1.03 ± 0.46	5.57 ± 1.04	4.54 ± 1.14
(c)	1.68 ± 0.44	5.15 ± 0.76	3.47 ± 0.88
(d)	1.92 ± 0.45	10.23 ± 0.99	8.31 ± 1.09
(e)	1.58 ± 0.50	6.79 ± 1.00	5.20 ± 1.12
Average	1.57 ± 0.21	7.01 ± 0.43	5.44 ± 0.48

Table 8.13: *Corrections $\Delta N^{b}_{D,l|MC}$ when $b \to l$.*

to a mis-identified $\overline{c}^{\,-2/3} \to l^-$ decay because the final state is the same. Therefore, the prompt lepton candidate will tend to have the same sign of electrical charge as the charm candidates from the second hemisphere. Table 8.13 shows the splitting of $N^{b}_{D,l|b\to l}$ MC events in opposite and same charge electrical sign pairs. A non–negligible correction of the order of 5% is required.

If in the first hemisphere one has $b^{-1/3} \to c^{+2/3} \to l^+$, it would correspond

to a $c^{+2/3} \to l^+$. Therefore, the charm candidates from the two hemispheres tend to have opposite sign of electrical charge, because the sign of the charm candidate flips twice via the $b \to c$ process. Table 8.14 shows the splitting of $N^b_{D,l|b\to c\to l}$ MC events in opposite and same charge electrical sign pairs. A correction of the order of 2% is required.

$b \to c \to l$	$\frac{N^{o.c.}_{h,L\|MC}}{(N^{o.c.}+N^{s.c})_{MC}}$ in %	$\frac{N^{s.c.}_{h,L\|MC}}{(N^{o.c.}+N^{s.c})_{MC}}$ in %	$\Delta\frac{N^{b}_{D,l\|b\to c\to l\|MC}}{(N^{o.c.}+N^{s.c})_{MC}}$ in %
(a)	4.63 ± 0.81	0.60 ± 0.30	4.03 ± 0.86
(b)	1.65 ± 0.58	0.41 ± 0.29	1.09 ± 0.65
(c)	2.40 ± 0.53	0.96 ± 0.34	1.44 ± 0.63
(d)	3.94 ± 0.64	0.96 ± 0.32	2.98 ± 0.72
(e)	3.31 ± 0.71	2.05 ± 0.56	1.26 ± 0.90
Average	3.19 ± 0.30	1.00 ± 0.17	2.16 ± 0.34

Table 8.14: *Corrections* $\Delta N^b_{D,l|MC}$ *when* $b \to c \to l$.

$b \to \overline{c} \to l$	$\frac{N^{o.c.}_{h,L\|MC}}{(N^{o.c.}+N^{s.c})_{MC}}$ in %	$\frac{N^{s.c.}_{h,L\|MC}}{(N^{o.c.}+N^{s.c})_{MC}}$ in %	$\Delta\frac{N^{b}_{D,l\|b\to \overline{c}\to l\|MC}}{(N^{o.c.}+N^{s.c})_{MC}}$ in %
(a)	0.00 ± 0.00	1.20 ± 0.42	1.20 ± 0.42
(b)	0.00 ± 0.00	0.62 ± 0.36	0.62 ± 0.36
(c)	0.00 ± 0.00	0.24 ± 0.36	0.24 ± 0.36
(d)	0.00 ± 0.00	1.07 ± 0.33	1.07 ± 0.33
(e)	0.00 ± 0.00	0.63 ± 0.32	0.63 ± 0.32
Average	0.00 ± 0.00	0.75 ± 0.15	0.75 ± 0.15

Table 8.15: *Corrections* $\Delta N^b_{D,l|MC}$ *when* $b \to \overline{c} \to l$.

$b(\to q) \to l$	$\frac{N^{o.c.}_{h,L\|MC}}{(N^{o.c.}+N^{s.c})_{MC}}$ in %	$\frac{N^{s.c.}_{h,L\|MC}}{(N^{o.c.}+N^{s.c})_{MC}}$ in %	$\Delta\frac{N^{b}_{D,l\|(b\to q)\to l\|MC}}{(N^{o.c.}+N^{s.c})_{MC}}$ in %
(a)	6.28 ± 0.94	9.12 ± 1.11	2.84 ± 1.46
(b)	2.68 ± 0.73	6.50 ± 1.13	3.92 ± 1.34
(c)	4.07 ± 0.68	6.35 ± 0.84	2.28 ± 1.09
(d)	5.86 ± 0.77	12.26 ± 1.07	6.40 ± 1.32
(e)	4.90 ± 0.86	9.48 ± 1.16	4.58 ± 1.45
Average	4.75 ± 0.36	8.77 ± 0.48	4.00 ± 0.60

Table 8.16: *Sum of corrections* $\Delta N^b_{D,l|MC}$.

If in the first hemisphere one has $b^{-1/3} \rightarrow \overline{b}^{+1/3} \rightarrow \overline{c}^{\,-2/3} \rightarrow l^-$, it would correspond to a $\overline{c}^{\,-2/3} \rightarrow l^-$. The two charm candidates have the same sign of the electrical charge again. Table 8.15 shows the splitting of $N^b_{D,l|b\rightarrow\overline{c}\rightarrow l}$ MC events in opposite and same charge electrical sign pairs. A correction of the order of 2% is required.

Because $BR(b \rightarrow l) + BR(b \rightarrow \overline{c} \rightarrow l) > BR(b \rightarrow c \rightarrow \mathrm{l})$, the term $N^b_{D,l}$ tends to be predominantly distributed in the $N^{s.c.}_{h,L}$ sample. An overall correction $\Delta N^b_{D,l}$ has to be applied and it is shown in Table 8.16.

8.6.3 Corrections due to Fake D Candidates ($\Delta N^{b,c}_{F,l}$)

Tables 8.17 to 8.21 show the splitting of $N^{b,c}_{Fl}$ Monte Carlo events in opposite and same charge electrical sign pairs. As shown in Section 8.3, the reconstruction of the electrical charge of the fake D candidate depends on the number of tracks involved in the D decay. In Tables 8.17 to 8.21, one can see that the $N_{F,l}$ events tend to follow the behaviour of the $N_{D,l}$ events, depending on the flavour of the initial quark and on the leptonic decay mode. A non–zero correction is required, which is dependent on the channel.

(a)	$\frac{N^{o.c.}_{h,L\|MC}}{(N^{o.c.}+N^{s.c})_{MC}}$ in %	$\frac{N^{s.c.}_{h,L\|MC}}{(N^{o.c.}+N^{s.c})_{MC}}$ in %	$\Delta\frac{N^{b,c}_{F,l\|MC}}{(N^{o.c.}+N^{s.c})_{MC}}$ in %
$(b \rightarrow l;F^b)$	0.00 ± 0.00	0.30 ± 0.21	0.30 ± 0.21
$(b \rightarrow c \rightarrow l;F^b)$	0.15 ± 0.15	0.00 ± 0.00	-0.15 ± 0.15
$(b \rightarrow \overline{c} \rightarrow l;F^b)$	0.00 ± 0.00	0.00 ± 0.00	0.00 ± 0.00
$(b(\rightarrow q) \rightarrow l;F^b)$	0.15 ± 0.15	0.30 ± 0.21	0.15 ± 0.26
$(c \rightarrow l;F^c)$	0.75 ± 0.33	0.14 ± 0.15	-0.60 ± 0.36

Table 8.17: *Corrections* $\Delta N^{b,c}_{F,f|MC}$ *for channel* (a).

(b)	$\frac{N^{o.c.}_{h,L\|MC}}{(N^{o.c.}+N^{s.c})_{MC}}$ in %	$\frac{N^{s.c.}_{h,L\|MC}}{(N^{o.c.}+N^{s.c})_{MC}}$ in %	$\Delta\frac{N^{b,c}_{F,l\|MC}}{(N^{o.c.}+N^{s.c})_{MC}}$ in %
$(b \rightarrow l;F^b)$	0.41 ± 0.30	0.21 ± 0.21	0.21 ± 0.36
$(b \rightarrow c \rightarrow l;F^b)$	0.00 ± 0.00	0.00 ± 0.00	0.00 ± 0.00
$(b \rightarrow \overline{c} \rightarrow l;F^b)$	0.00 ± 0.00	0.00 ± 0.00	0.00 ± 0.00
$(b(\rightarrow q) \rightarrow l;F^b)$	0.41 ± 0.29	0.21 ± 0.21	-0.21 ± 0.36
$(c \rightarrow l;F^c)$	4.33 ± 0.92	0.41 ± 0.29	-3.92 ± 0.97

Table 8.18: *Corrections* $\Delta N^{b,c}_{F,f|MC}$ *for channel* (b).

(c)	$\frac{N^{o.c.}_{h,L\|MC}}{(N^{o.c.}+N^{s.c})_{MC}}$ in %	$\frac{N^{s.c.}_{h,L\|MC}}{(N^{o.c.}+N^{s.c})_{MC}}$ in %	$\Delta\frac{N^{b,c}_{F,l}}{(N^{o.c.}+N^{s.c})_{MC}}$ in %
$(b \to l;F^b)$	0.84 ± 0.32	1.80 ± 0.46	0.96 ± 0.56
$(b \to c \to l;F^b)$	0.72 ± 0.29	0.24 ± 0.17	-0.48 ± 0.34
$(b \to \overline{c} \to l;F^b)$	0.00 ± 0.00	0.00 ± 0.00	0.00 ± 0.00
$(b(\to q) \to l;F^b)$	1.56 ± 0.43	2.04 ± 0.49	0.48 ± 0.65
$(c \to l;F^c)$	10.30 ± 1.05	1.91 ± 0.47	-8.38 ± 1.15

Table 8.19: *Corrections* $\Delta N^{b,c}_{F,f\|MC}$ *for channel* (c).

(d)	$\frac{N^{o.c.}_{h,L\|MC}}{(N^{o.c.}+N^{s.c})_{MC}}$ in %	$\frac{N^{s.c.}_{h,L\|MC}}{(N^{o.c.}+N^{s.c})_{MC}}$ in %	$\Delta\frac{N^{b,c}_{F,l\|MC}}{(N^{o.c.}+N^{s.c})_{MC}}$ in %
$(b \to l;F^b)$	1.81 ± 0.44	1.92 ± 0.45	0.11 ± 0.62
$(b \to c \to l;F^b)$	0.64 ± 0.26	0.75 ± 0.28	0.11 ± 0.38
$(b \to \overline{c} \to l;F^b)$	0.11 ± 0.11	0.21 ± 0.15	0.11 ± 0.18
$(b(\to q) \to l;F^b)$	2.56 ± 0.52	2.88 ± 0.55	0.32 ± 0.75
$(c \to l;F^c)$	0.75 ± 0.28	1.28 ± 0.37	0.53 ± 0.46

Table 8.20: *Corrections* $\Delta N^{b,c}_{F,f\|MC}$ *for channel* (d).

(e)	$\frac{N^{o.c.}_{h,L\|MC}}{(N^{o.c.}+N^{s.c})_{MC}}$ in %	$\frac{N^{s.c.}_{h,L\|MC}}{(N^{o.c.}+N^{s.c})_{MC}}$ in %	$\Delta\frac{N^{b,c}_{F,l\|MC}}{(N^{o.c.}+N^{s.c})_{MC}}$ in %
$(b \to l;F^b)$	2.21 ± 0.58	1.58 ± 0.50	-0.63 ± 0.77
$(b \to c \to l;F^b)$	0.00 ± 0.00	0.63 ± 0.31	0.63 ± 0.31
$(b \to \overline{c} \to l;F^b)$	0.00 ± 0.00	0.79 ± 0.35	0.79 ± 0.35
$(b(\to q) \to l;F^b)$	2.21 ± 0.58	3.00 ± 0.68	0.79 ± 0.89
$(c \to l;F^c)$	6.32 ± 0.97	1.27 ± 0.44	-5.06 ± 1.06

Table 8.21: *Corrections* $\Delta N^{b,c}_{F,f\|MC}$ *for channel* (e).

8.6.4 Corrections due to Fake D and Lepton Candidates ($\Delta N^{b,c,uds}_{F,f}$)

When a fake candidate is reconstructed, the probability for it to have positive electrical charge is equal to the probability for it to have a negative one.

Tables 8.22, 8.23 and 8.24 show the splitting of $N_{F,f}$ MC events in opposite and same charge electrical sign pairs, when the fake D candidates originate from all possible flavours. As expected, the corrections found in the MC are consistent with zero for all the analysed channels.

$(b \to f; F^b)$	$\frac{N^{o.c.}_{h,L\|MC}}{(N^{o.c.}+N^{s.c})_{MC}}$ in %	$\frac{N^{s.c.}_{h,L\|MC}}{(N^{o.c.}+N^{s.c})_{MC}}$ in %	$\Delta\frac{N^{b}_{F,f\|MC}}{(N^{o.c.}+N^{s.c})_{MC}}$ in %
(a)	0.00 ± 0.00	0.00 ± 0.00	0.00 ± 0.00
(b)	0.00 ± 0.00	0.00 ± 0.00	0.00 ± 0.00
(c)	0.12 ± 0.12	0.36 ± 0.21	0.24 ± 0.24
(d)	0.43 ± 0.21	0.11 ± 0.11	-0.32 ± 0.24
(e)	0.16 ± 0.16	0.00 ± 0.00	0.16 ± 0.16
Average	0.14 ± 0.06	0.09 ± 0.05	0.05 ± 0.07

Table 8.22: *Corrections* $\Delta N^{b}_{F,l|MC}$.

$(c \to f; F^c)$	$\frac{N^{o.c.}_{h,L\|MC}}{(N^{o.c.}+N^{s.c})_{MC}}$ in %	$\frac{N^{s.c.}_{h,L\|MC}}{(N^{o.c.}+N^{s.c})_{MC}}$ in %	$\Delta\frac{N^{c}_{F,f\|MC}}{(N^{o.c.}+N^{s.c})_{MC}}$ in %
(a)	0.45 ± 0.26	0.15 ± 0.15	-0.30 ± 0.30
(b)	0.82 ± 0.41	0.62 ± 0.36	-0.21 ± 0.54
(c)	1.56 ± 0.43	1.68 ± 0.44	0.12 ± 0.62
(d)	0.11 ± 0.11	0.32 ± 0.18	0.21 ± 0.21
(e)	0.63 ± 0.31	0.79 ± 0.35	0.16 ± 0.47
Average	0.71 ± 0.15	0.71 ± 0.14	0.00 ± 0.20

Table 8.23: *Corrections* $\Delta N^{c}_{F,l|MC}$.

$(uds \to f; F^{uds})$	$\frac{N^{o.c.}_{h,L\|MC}}{(N^{o.c.}+N^{s.c})_{MC}}$ in %	$\frac{N^{s.c.}_{h,L\|MC}}{(N^{o.c.}+N^{s.c})_{MC}}$ in %	$\Delta\frac{N^{c}_{F,f\|MC}}{(N^{o.c.}+N^{s.c})_{MC}}$ in %
(a)	0.00 ± 0.00	0.00 ± 0.00	0.00 ± 0.00
(b)	0.41 ± 0.29	1.03 ± 0.46	0.62 ± 0.54
(c)	0.60 ± 0.27	0.72 ± 0.29	0.12 ± 0.40
(d)	1.07 ± 0.33	1.39 ± 0.38	0.32 ± 0.51
(e)	0.95 ± 0.38	0.95 ± 0.38	0.00 ± 0.55
Average	0.60 ± 0.13	0.82 ± 0.15	0.21 ± 0.20

Table 8.24: *Corrections* $\Delta N^{uds}_{F,l|MC}$.

8.7 Implementation of MC Corrections

In order to derive the number of leptons available in real data for each of these classes, a rescaling of the MC values is made, by a factor f_{MC}:

$$f_{MC} = \frac{N^{o.c.}_{Data} + N^{s.c.}_{Data}}{N^{o.c.}_{MC} + N^{s.c.}_{MC}} \tag{8.17}$$

This rescaling is based on the total number of lepton candidates found in real data ($N^{o.c.}_{Data} + N^{s.c.}_{Data}$) and in the MC simulated data ($N^{o.c.}_{MC} + N^{s.c.}_{MC}$). The

values of the rescaling factor f_{MC} and of the total corrections are given in Table 8.25. The correction, extracted from the MC, is:

$$\Delta N_{h,L} \quad = \quad [N^{c}_{D,l|MC} - (N^{o.c.}_{MC} - N^{s.c.}_{MC})] \cdot f_{MC} \tag{8.18}$$

The values of the total corrections $\Delta N_{h,L}$ are given in the fifth column of Table 8.25, comparative with the total number of leptons found with these corrections included, $(N^{o.c.}_{Data} + N^{s.c.}_{Data} = N^{c}_{D,l|Data})$, shown in the last column. The second column in the table shows the scaling factor f_{MC}, while the third and the forth columns show the number of leptons found in MC data prior and after rescaling to the amount of Z^0 events in data.

8.8 Number of Leptons Found in Data

From Equations 8.10, 8.17 and 8.18, the final formula for computing $N^{c}_{D,l|Data}$ is:

$$N^{c}_{D,l|Data} = (N^{o.c.}_{Data} - N^{s.c.}_{Data}) + [N^{c}_{D,l|MC} - (N^{o.c.}_{MC} - N^{s.c.}_{MC})] \cdot \frac{N^{o.c.}_{Data} + N^{s.c.}_{Data}}{N^{o.c.}_{MC} + N^{s.c.}_{MC}} \tag{8.19}$$

The numbers of true prompt leptons coming from c quarks found in data is shown in the last column of Table 8.25.

Channel	f_{MC}	$N^{c}_{D,l\|MC}$	$N^{c}_{D,l\|MC(resc)}$	$\Delta N_{h,L}$	$N^{c}_{D,l\|Data}$
(a)	0.57	440	280	3	221±22
(b)	0.77	314	200	1	243±22
(c)	0.65	439	280	−31	270±26
(d)	0.63	389	247	35	257±26
(e)	0.69	346	220	7	265±24

Table 8.25: *The number of leptons in MC, due to MC corrections and their values without corrections.*

Using Equation 5.4 with the branching ratio implemented in the MC $BR(c \to l)_{MC} = 0.102$ and the numbers given by Tables 7.15 and 8.25, the branching ratios given in third column of Table 9.18 are computed. Their computation used fractional numbers for the fitted N^{c}_{D}, $N_D|MC^{c}$ and $N^{c}_{D,l|MC}$, while Tables 7.15 and 8.25 show integer, rounded numbers.

Chapter 9

Error Analysis

The five values f_k, which were calculated for the channels (a) to (e) (see Section 5.1; there $f_k = BR_k$) represent the values of an estimator f of the parameter $BR = BR(c \to l+X)$, estimator given by Equation 9.1. The set of $n = 5$ experimental variables, f_k, are accompanied by a set of n uncorrelated statistical errors σ_k^{stat}, and a set of n partially correlated systematic errors σ_k^{syst}. In Equation 9.1, σ is the set of the errors and $Cov(\sigma_{stat}, \sigma_{syst})$ is their correlation matrix, both of which are known.

$$f = f(f_k|k = 1,5; \sigma_{stat}; \sigma_{syst}; Cov(\sigma_{stat}, \sigma_{syst})) \tag{9.1}$$

Statistical errors are presented in Section 9.1, while systematic uncertainties are shown in Section 9.2. The combination of both error types is discussed in Sections 9.3 and 9.4, with the final error presented in Section 9.5. The probability and statistics notions used in this chapter are detailed in Appendix B.

9.1 Statistical Errors

Statistical errors are due to natural variations in the measured quantities q for the selected sample of events. The square root of the variance of the measured quantity σ_q is quoted as statistical error. The component of the statistical $\sigma_q^{stat}(BR)$ due to the quantity q is obtained applying (see Equation 9.2) the error propagation formula.

$$\sigma_q^{stat}(BR) = \frac{\partial\ BR(c \to l + X)_{Data}}{\partial\ q} * \sigma_q \tag{9.2}$$

The statistical error $BR(c \to l + X)$, as computed in this analysis (see Equation 5.4), has a factor related to the number of true charm D candidates,

$$g_{N_D^c} = \frac{N^c_{D|Data}}{N^c_{D|MC}}, \tag{9.3}$$

and a factor related to the number of prompt leptons coming from these candidates,

$$g_{N^c_{D,l}} = \frac{N^c_{D,l|Data}}{N^c_{D,l|MC}}, \tag{9.4}$$

The detailed procedure how one calculates N^c_D and N_{D,l^c}, and their values for Data and MC, are given in Sections 7.5 and 8.8, respectively.

9.1.1 The Statistical Errors on the Number of D Candidates

Equation 7.13 can be rewritten as

$$N^c_D = \frac{\epsilon_b \times N_1 - N_2}{\epsilon_b - \epsilon_c} \tag{9.5}$$

The statistical error $\sigma_{N^c_D}$ has four sources:

- $\sigma_{N_{signal}}$ due to the fluctuations σ_1 of signal events in the mass window, $N_{signal} = N_1 = N_h - N_F$;
- $\sigma_{N^{btag}_{signal}}$ due to fluctuations σ_2 of signal b-tagged events in the mass window, $N^{btag}_{signal} = N_2 = N^{btag}_h - N^{btag}_F$;
- σ_{ϵ_c} due fluctuations σ_3 of the efficiency to b-tag particles coming from c quarks, $\epsilon_c = \frac{N^{btag}_c}{N_c}$ (see Section 7.5);
- σ_{ϵ_b} due to fluctuations σ_4 of the efficiency to b-tag particles coming from b quarks, $\epsilon_b = \frac{N^{btag}_b}{N_b}$ (see Section 7.5).

$$\begin{aligned}
\sigma_{N^c_D} &= \sqrt{{\sigma_{N^{btag}_{signal}}}^2 + \sigma^2_{N_{signal}} + \sigma^2_{\epsilon_c} + \sigma^2_{\epsilon_b}} \\
\sigma_{N_{signal}} &= \tfrac{\epsilon_b}{\epsilon_b - \epsilon_c}\sigma_1 \\
\sigma_{N^{btag}_{signal}} &= \tfrac{-1}{\epsilon_b - \epsilon_c}\sigma_2 \\
\sigma_{\epsilon_c} &= \tfrac{-N^c_D}{\epsilon_b - \epsilon_c}\sigma_3 \\
\sigma_{\epsilon_b} &= \tfrac{-N^b_D}{\epsilon_b - \epsilon_c}\sigma_4
\end{aligned} \tag{9.6}$$

where N^b_D is given by Equation 7.12 and

$$\begin{aligned}
\sigma_1 &= \sqrt{\sigma^2_{N_h} + \sigma^2_{N_F}} \\
\sigma_2 &= \sqrt{\sigma^2_{N^{btag}_h} + \sigma^2_{N^{btag}_F}} \\
\sigma_3 &= \sqrt{\tfrac{\epsilon_c(1-\epsilon_c)}{N_c}} \\
\sigma_4 &= \sqrt{\tfrac{\epsilon_b(1-\epsilon_b)}{N_b}}
\end{aligned}$$

Above one uses $\sigma_{\mathcal{N}} = \sqrt{\mathcal{N}}$, while the error on the combinatorial background σ_{N_F} is given by the second order polynomial fit procedure (see Section 7.5).

The equations 9.6 can be written both for data and MC, the statistical errors on the number of selected D candidates $\sigma_{N_D^c}$ being listed in Tables 9.1 and 9.2 respectively, together with their components.

Channel	$\sigma_{N_{signal}}$	σ_{ϵ_c}	σ_{ϵ_b}	$\sigma_{N_{signal}^{btag}}$	$N^c_{D\|Data} \pm \sigma_{N^c{}_{D\|Data}}$
(a)	60	22	11	47	2690±80
(b)	65	16	10	74	1784±100
(c)	82	19	23	53	2738±103
(d)	82	17	23	53	2267±101
(e)	65	15	18	44	2140±82

Table 9.1: *The statistical error on the number of charmed D candidates selected in the data, and its sources.*

Channel	$\sigma_{N_{signal}}$	σ_{ϵ_c}	σ_{ϵ_b}	$\sigma_{N_{signal}^{btag}}$	$N^c_{D\|MC} \pm \sigma_{N^c{}_{D\|MC}}$
(a)	75	34	30	59	4070±106
(b)	86	18	7	83	2060±121
(c)	97	29	33	17	4064±124
(d)	100	25	32	63	3348±124
(e)	75	19	28	53	2803±98

Table 9.2: *The statistical error on the number of charmed D candidates selected in the MC, and its sources.*

The resulting statistical errors σ_{D^c} (see Equation 9.7) due to the number of true charmed D candidates, given by

$$\begin{aligned} \sigma_{D^c} &= \sqrt{\sigma^2_{D^c_{Data}} + \sigma^2_{D^c_{MC}}} \\ \sigma_{D^c_{Data}} &= \frac{N^c_{D,l|Data} N^c_{D|MC}}{N^c_{D|Data} N^c_{D,l|MC}} \cdot \sigma_{N^c{}_{D|Data}} \cdot BR(c \to l)_{MC} \\ \sigma_{D^c_{MC}} &= \frac{N^c_{D,l|Data}}{{N^c_{D|Data}}^2 N^c_{D,l|MC}} \cdot \sigma_{N^c{}_{D|MC}} \cdot BR(c \to l)_{MC} \end{aligned} \tag{9.7}$$

are presented in the last column of Table 9.3.

Channel	$\sigma_{D^c_{Data}}$ in %	$\sigma_{D^c_{MC}}$ in %	σ_{D^c} in %
(a)	0.23	0.20	0.31
(b)	0.54	0.54	0.76
(c)	0.35	0.29	0.45
(d)	0.35	0.30	0.46
(e)	0.39	0.36	0.53

Table 9.3: *The absolute statistical errors due to the number of charmed D candidates.*

9.1.2 The Statistical Errors on the Number of (D, l) Candidates

As seen in Equation 9.8, the statistical error $\sigma_{N^c_D}$ has five sources of independent fluctuations, which are combined by adding them quadratically:

- $\sigma_{N^{s.c.}_{Data}}$;
- $\sigma_{N^{o.c.}_{Data}}$;
- $\sigma_{N^{s.c.}_{MC}}$;
- the two components of $\sigma_{N^{o.c.}_{MC}}$:
  - $\sigma_{N^c_{D,l|MC}}$;
  - σ_R, where $N^{o.c.}_{MC} = R + N^c_{D,l|MC}$, $R = N^{fake,o.c.}_{h,L|MC}$ (see Equation 8.7).

All the statistical fluctuations listed above are given by $\sigma_{\mathcal{N}} = \sqrt{\mathcal{N}}$.

The (D, l) term in computing the $BR(c \to l + X)$ is (see Equations 9.4 and 8.19):

$$g_{N^c_{D,l}} = \frac{N^c_{D,l|Data}}{N^c_{D,l|MC}} = \frac{(N^{o.c.}_{Data} - N^{s.c.}_{Data}) - (R - N^{s.c.}_{MC})}{N^c_{D,l|MC}} \cdot \frac{N^{o.c.}_{Data} + N^{s.c.}_{Data}}{R + N^c_{D,l|MC} + N^{s.c.}_{MC}} \tag{9.8}$$

Channel	$\sigma_{N^{s.c.}_{Data}}$ in %	$\sigma_{N^{o.c.}_{Data}}$ in %	$\sigma_{N^{s.c.}_{MC}}$ in %	$\sigma_{N^{o.c.}_{MC}}$ in %	$\sigma_{N^c_{D,l|MC}}$ in %	σ_R in %	$\sigma_{(D,l)^c}$ in %
(a)	0.32	0.62	0.22	0.48	0.43	0.21	0.87
(b)	0.30	0.67	0.27	0.56	0.48	0.27	0.96
(c)	0.40	0.67	0.32	0.67	0.58	0.33	1.06
(d)	0.36	0.68	0.31	0.44	0.30	0.33	0.92
(e)	0.36	0.73	0.33	0.62	0.52	0.33	1.06

Table 9.4: *The absolute statistical errors due to the number of charmed $(D,l)^c$ lepton candidates.*

9.1.3 Combining Statistical Errors due to D and (D,l) Candidates

The statistical errors due to charmed D candidates and true prompt lepton candidates are added in quadrature,

$$\sigma^{stat}(BR) = \sqrt{{\sigma_{D^c}}^2 + {\sigma_{(D,l)^c}}^2} \quad (9.9)$$

with results shown in Table 9.5.

One can see that the dominant statistical error comes from the leptonic side,

Channel	σ_{D^c} in %	$\sigma_{(D,l)^c}$ in %	$\sigma^{stat}(BR)$ in %
(a)	0.31	0.84	0.89
(b)	0.76	0.96	1.22
(c)	0.45	1.06	1.15
(d)	0.46	0.92	1.03
(e)	0.53	1.06	1.18

Table 9.5: *The absolute statistical errors due to the number of charmed D candidates and true prompt lepton candidates.*

since the number of leptons is about ten times smaller than the number of charmed D candidates, depending on the channel.

9.1.4 Combining Statistical Errors due to Data and MC

Rewriting Equation 5.4 as:

$$BR(c \to l + X) = \frac{g_{Data}}{g_{MC}} \cdot BR(c \to l)_{MC} \quad (9.10)$$

one can split the statistical total relative error into one related to the data, $\sigma^{stat}_{Data}(BR)$, and one related to the MC, $\sigma^{stat}_{MC}(BR)$, where the two factors are:

$$g_{Data} = \frac{N^c_{D,l|Data}}{N^c_{D|Data}}$$

$$g_{MC} = \frac{N^c_{D,l|MC}}{N^c_{D|MC}}.$$

The errors on the number of charmed D and true lepton candidates are calculated using the numbers in Tables 7.11, 7.12, and 8.25.

The total statistical error, $\sigma^{stat}(BR)$, is the sum in quadrature (see Equation 9.9) of the statistical error due to the collected data, $\sigma^{stat}_{Data}(BR)$, and the statistical error due to the finite number of events available in the MC samples, $\sigma^{stat}_{MC}(BR)$:

$$\sigma^{stat}(BR)^2 = \sigma^{stat}_{Data}(BR)^2 + \sigma^{stat}_{MC}(BR)^2 \quad (9.11)$$

In Table 9.6, a summary of the statistical errors is presented for the five channels, (a) to (e). The statistical errors $\sigma^{stat}_{Data}(BR)$ and $\sigma^{stat}_{MC}(BR)$ are computed by using Equation 9.9 for real and Monte Carlo data samples.

Channel	$\sigma^{stat}(BR)$ in %	$\sigma^{stat}_{Data}(BR)$ in %	$\sigma^{stat}_{MC}(BR)$ in %
(a)	0.89	0.73	0.51
(b)	1.22	0.90	0.82
(c)	1.15	0.86	0.77
(d)	1.03	0.84	0.59
(e)	1.18	0.90	0.76

Table 9.6: *Absolute statistical errors, due to real and Monte Carlo data.*

9.2 Systematic Uncertainties

During the selection of the signal events, two types of errors have to be considered:

- Type I: Rejecting the event, even if it was a signal event. This sort of error is usually reflected by the efficiency of the selection, and cancels out in the final result. However, at a certain stage of this analysis, this error does not cancel, but enters twice in the final result.
- Type II: Accepting a background event as signal.

The systematic errors coming from incorrect assignment of the electrical charge of the charm candidate (see Section 9.2.1) are Type I errors. All the other systematic uncertainties, coming from the detection of charmed mesons and prompt leptons (see Sections 9.2.1 to 9.2.9), can be included in the Type II errors class.

9.2.1 Charge Tagging in Charm Quark Hemispheres

As shown in Section 8.3, special care was taken of D-candidates with the electrical charge incorrectly assigned. According to Equation 8.8, the number of prompt lepton candidates coming from c quarks is given, up to corrections $\Delta N_{h,L}$ based on MC studies, by:

$$N^{c}_{D,l} \;=\; N^{oc}_{D,L} - N^{sc}_{D,L} \tag{9.12}$$

where the charge of the D meson is supposed to be correctly assigned.

By wrongly assigning the charge of the D meson, one does not assign the lepton candidate to the correct class, but to the opposite one. (Lepton candidates migrate from $N^{oc}_{D,L}$ to $N^{sc}_{D,L}$, or from $N^{sc}_{D,L}$ to $N^{oc}_{D,L}$.) Therefore, a variation δ counts twice:

$$\begin{aligned} N_{\delta} &= (N^{oc}_{D,L} + \delta) - (N^{sc}_{D,L} - \delta) \\ &= N^{c}_{D,l} + 2\delta \end{aligned} \tag{9.13}$$

These errors are not related to the number of events available in each channel, but only to the number of tracks reconstructed in each of the events. Therefore, they are not incorporated in the statistical errors, but in the systematic ones – being a systematic effect due to the procedure of analysis. This type of error was studied by artificially increasing in the sample selected in the MC the number of (l^-, D^+) and (l^+, D^-) events and decreased by the same amount the (l^-, D^+) and (l^+, D^-) events by the percentages shown in the second line of Table 9.7. The corresponding variation of the $BR(c \to l + X)$ (see third line of Table 9.7) is taken as a systematic uncertainty for each of the five studied channels.

Channel	(a)	(b)	(c)	(d)	(e)
percentage of D mesons with electrical charge incorrectly assigned	1	1	3	1	2
$\sigma_{wr\ assig}$ in %	< 0.01	< 0.01	< 0.01	0.01	< 0.01

Table 9.7: *Uncertainties on the $BR(c \to l + X)$ due to wrong assignment of the electrical charge of the D meson.*

These uncertainties should increase with the number of tracks which have to be reconstructed in each of the channels, hence they are an expression of a statistical effect. The errors between the channels are considered completely uncorrelated, because the procedures to reconstruct the individual tracks are completely uncorrelated. However, the number of D mesons with the electrical charge incorrectly assigned was equal to zero in all the channels, except for channel d, where one event (having a true prompt lepton with the electrical charge having the same sign as the charmed quark) was found in MC, out of a total of 1403 $c \to$ leptonic events selected.

9.2.2 Fragmentation of b and c Quarks

Charm and bottom fragmentation were simulated in the Monte Carlo of the ALEPH experiment using the Peterson model (see Section 2.5.2). The momentum shapes of the c and b flavored mesons are controlled by the parameters ξ_c and ξ_b. These shapes are adjusted in the MC to reproduce the measured values of the mean scaled energies of weakly decaying c and b hadrons respectively.

Fitting the experimental curves observed by ALEPH, values of $< \xi_c >= (3.6 \pm 0.7) \cdot 10^{-2}$ and $< \xi_b >= (3.8 \pm 0.1) \cdot 10^{-3}$ have been extracted. In the MC simulation, these values have been varied by their experimental errors

and the resulting change in the branching ratio taken as a systematic error. These errors are presented in Table 9.8.

Channel	$\sigma_{b\ fragmentation}$ in %	$\sigma_{c\ fragmentation}$ in %	$\sigma_{c\&b\ fragmentation}$ in %
(a)	0.02	0.07	0.07
(b)	0.16	0.15	0.17
(c)	0.07	0.04	0.08
(d)	0.01	0.10	0.10
(e)	0.08	0.18	0.20

Table 9.8: *Systematic uncertainties on the $BR(c \to l + X)$ due to b and c fragmentation.*

In Table 9.8, the last column represents the combined variation, where both the b and c fragmentation effects were considered. Its values are the sum in quadrature of separate effects. The systematic uncertainty, due to b fragmentation in channel (d), is less than 10^{-4}. To show that it has a nonzero value, one takes it equal to 0.01%, which is a conservative upper limit of the calculated value.

9.2.3 Heavy Quarks from Gluon Splitting

In this analysis bottom and charm quarks can be produced from direct Z^0 decay, and also from the splitting of hard gluons. In the second case, the resulting b and c quarks will have a significantly softer energy spectrum. As a consequence, the resulting leptons will show different kinematic properties. The world average values have been used [52] for the ratio of the number of gluons splitting to b and c quarks per Z^0 decay (see Table 9.9).

No.	q_{resc}	Experimental value	Experimental uncertainty
1	$N(g \to c\bar{c})$	0.0296	± 0.038
2	$N(g \to b\bar{b})$	0.00254	± 0.00051

Table 9.9: *Number of gluons splitting to heavy quarks per hadronic Z^0 decay*

The above values for the experimental numbers of c and b quarks, from gluon splitting per hadronic Z^0 decay, are consistent with the values implemented in the JETSET part of MC (see Section 4.1.1). Further re-scalings for these quantities were not necessary.

The experimental errors in Table 9.9, for measuring the number of gluons splitting to heavy quarks per hadronic Z^0 decay, were used to compute the associated systematic uncertainty (see Table 9.10).

Channel	(a)	(b)	(c)	(d)	(e)
$\sigma_{g\ split}$ in %	0.01	0.02	0.01	0.01	0.01

Table 9.10: *Absolute systematic uncertainties on the $BR(c \to l + X)$ due to gluon splitting.*

9.2.4 B–$\overline{B}$ Mixing

The mixing of neutral B mesons contributes to the degradation of the correlation between the charge of the lepton and the charge of the initial b quark produced in $Z^0 \to b\overline{b}$ decay. B–mixing affects the b background subtraction. The $\chi = 0.187 \pm 0.004$ parameter [53], giving the fraction of B^0–mesons oscillating to $\overline{B}^0$, is varied inside its experimental uncertainties. The shifts observed in the value of $BR(c \to l + X)$ are taken as systematic uncertainties (see Table 9.11).

Channel	(a)	(b)	(c)	(d)	(e)
$\sigma_{B\ mix}$ in %	0.01	0.01	0.01	0.01	0.01

Table 9.11: *Absolute systematic uncertainties on the $BR(c \to l + X)$ due to B-mixing.*

9.2.5 Efficiencies of b Tagging

The calculation of sample composition, described in Section 7.5, relies on events selected applying the b tagging (see Equations 7.9 and 7.10). The estimates of these selection efficiencies, for the charm, bottom and light quarks, have values obtained by studying the MC simulated sample.

Table 9.12 shows, in the first two columns, the values of the efficiency to select a b quark when applying the b tagging, ϵ_b, and the efficiency to select a c quark ϵ_c. The efficiencies used in each of the five analysed channels are presented, and their quoted errors are due to statistical variations of the numbers of events used in their computation.

When varying the efficiencies ϵ_b and ϵ_c inside the range of their errors, approximately 10% (which includes the range of σ_{ϵ_b} and σ_{ϵ_c}), one takes the corresponding variation of the $BR(c \to l + X)$ as a systematic uncertainty.

For all the considered channels, the values of the systematic uncertainties

Channel	ϵ_b in %	ϵ_c in %	$\sigma_{b\ tagging\ efficiencies}$ in %
(a)	33.25 ± 2.02	2.75 ± 0.25	0.01
(b)	31.19 ± 2.76	2.20 ± 0.26	0.01
(c)	30.09 ± 1.78	2.07 ± 0.19	0.01
(d)	31.39 ± 1.51	2.06 ± 0.20	0.01
(e)	35.19 ± 0.54	1.99 ± 0.11	0.01

Table 9.12: *Absolute systematic uncertainties on the $BR(c \to l + X)$ due to lepton identification efficiency.*

were less than 0.01%. The last column of Table 9.12 shows the conservative systematic uncertainties, underlining their nonzero values, which are used to compute the final error.

The efficiencies ϵ_{uds}, to select a light quark by applying the b tagging, are negligible to an order of magnitude less than 0.1%. Therefore, the influence of their variation on the value of the branching ratio $BR(c \to l + X)$, is also negligible.

9.2.6 Uncertainties of Leptonic Branching Ratios

The rescaled leptonic branching ratios of the b quark are listed in Table 9.13 with their errors. In order to obtain the systematic uncertainties, the branching ratios are rescaled, according to the procedure described in Section 8.2, to $q \pm \sigma_q$. The corresponding variation of the $BR(c \to l + X)$, due to this rescaling, is taken as a systematic uncertainty.

No.	q_{resc}	Experimental value, q (absolute values),σ_q	Experimental uncertainty
1	$BR(b \to l)$	10.67 %	$\pm$ 0.21 %
2	$BR(b \to c \to l)$	8.08 %	$\pm$ 0.17 %
3	$BR(b \to \overline{c} \to l)$	1.62 %	$\pm$ 0.44 %

Table 9.13: *Sources of systematic uncertainties on the $BR(c \to l+X)$ due to leptonic branching ratios experimental errors*

The systematic uncertainties, shown in Table 9.14, are computed using relations type Equations 8.1 and 8.2. The values from the last column, $BR(b\ (\to X) \to l)$, represent the systematic errors due to the 3 sources varied together (each by $+1\sigma$). These values are equal to the values one obtains by adding in quadrature the three separate errors. Therefore, they constitute a cross check of those last three types of errors.

For channels (b) and (e), the systematic uncertainties due to the uncertainties in the branching ratio $BR(b \to c \to l)$ are less than 0.01%. The

Channel	$\sigma_{BR(b\to l)}$ in %	$\sigma_{BR(b\to c\to l)}$ in %	$\sigma_{BR(b\to\bar{c}\to l)}$ in %	$\sigma_{BR(b\ (\to X)\to l)}$ in %
(a)	0.02	0.01	0.05	0.05
(b)	0.01	0.01	0.03	0.03
(c)	0.02	0.01	0.03	0.04
(d)	0.03	0.01	0.06	0.07
(e)	0.01	0.01	0.07	0.07

Table 9.14: *Absolute systematic uncertainties on the $BR(c \to l + X)$ due to leptonic branching ratios experimental errors*

corresponding values for these two errors, as shown in Table 9.14, are therefore conservative estimates.

9.2.7 Lepton Background

The lepton candidate has to be real and prompt. Therefore, lepton background is due to two sources: incorrectly identified non-leptons and real non-prompt leptons.

Channel	σ due to misidentified leptons in %	σ due to non-prompt leptons in %	σ due to lepton background in %
(a)	0.04	0.01	0.04
(b)	0.02	0.01	0.02
(c)	0.01	0.01	0.02
(d)	0.07	0.05	0.08
(e)	0.01	0.02	0.02

Table 9.15: *Absolute systematic uncertainties on the $BR(c \to l + X)$ due to lepton misidentification and non-prompt leptons*

Some hadrons, for example charged kaons and pions, can be misidentified as leptons. For the ALEPH data samples, this type of background was studied [52] and an uncertainty of 20% on the background level has be assigned. The systematic uncertainty due to lepton background was estimated by varying, in the MC, the fake lepton candidates coming from $K^{\pm}$ and $\pi^{\pm}$ by 20%. This leads to the systematic uncertainties shown in the first column of Table 9.15.

Also considered is the background due to electrons coming from an unidentified photon conversion $\gamma \to e^+e^-$, and due to kaons and pions decaying before entering the calorimeters ($K \to \mu$, $\pi \to \mu$). The associated systematic uncertainty (see second column in Table 9.15) was calculated considering the previous studies performed in ALEPH [52]. The number of this type of non-prompt leptons, present in the MC samples, was varied by 10%.

The values in the third column, in Table 9.15 represent the combined systematic uncertainty due to the previous discussed sources of leptonic background. Because the two types of background are uncorrelated, the values in the third column are obtained for each channel by adding in quadrature the values from the first and second columns.

9.2.8 Lepton Identification Efficiency

The electron identification efficiency has been measured from data using photon conversions in the detector material [52]. The average identification efficiency for leptons was about 93% (94% for electrons and 92% for muons). The dependence on momentum, transverse momentum and polar angle have been considered. The variations between data and MC simulations were less than 1%.

The identification efficiency for high energy muons has been measured from data using Z^0 decays to muon pairs [52]. The dependence on the polar and the azimuthal angles have been considered. The variations between data and MC simulations were typically a few per mil.

In the present analysis, a variation of 2% of the MC lepton identification efficiency has been considered, for both the electron and muon candidates. This was implemented by increasing the number of detected true prompt lepton candidates by 2%. The corresponding variations of the $BR(c \to l+X)$ (see Table 9.16) were taken as a systematic uncertainty.

Channel	(a)	(b)	(c)	(d)	(e)
σ due to lept eff in %	0.15	0.19	0.18	0.19	0.20

Table 9.16: *Absolute systematic uncertainties on the $BR(c \to l + X)$ due to lepton identification efficiency.*

One observes that the variation by 2% of the lepton identification efficiency is consistent with the variation by approximatively 2% in the branching ratio value.

9.2.9 Modelling of Leptonic Decays

A $c \to l + X$ decay spectrum is obtained by means of a combined fit [52] to DELCO and MARK III data, performed using the ACCMM model [52]. The $b \to l + X$ prompt decay spectrum is modelled, as described in [52]. In order to describe $b \to c \to l + X$ decays, the model for $c \to l + X$ is combined with the measured $b \to D$ spectrum from CLEO.

These lepton spectra is varied in MC to correspond to the models described above. The shifts observed in the value of $BR(c \to l + X)$ are taken as systematic uncertainties (see Table 9.17).

Channel	(a)	(b)	(c)	(d)	(e)
$\sigma_{l\ mod}$ in %	0.28	0.31	0.29	0.35	0.37

Table 9.17: *Absolute systematic uncertainties on the $BR(c \to l+X)$ due to modelling of the leptonic decays.*

9.3 Combining Statistical and Systematic Errors

In order to calculate the total error of the final result, one denotes the five measured branching ratios as f_k (with $k = 1, 5$). The measurements are made on subsamples selected out of the same sample of MC and data events. Therefore, the total error has to take into account the existing correlations between the individual errors of the measurement representing each channel.

Up to this point, the statistical and systematic errors have been presented. However, because the same data sample is used for the five determinations f_k, the correlation between different channels has to be taken in account. Because there is a large number of contributing systematic errors they cancel out. One can expect that the systematic uncertainty knowledge in the final value fluctuates in the same way as the statistical one. Therefore, one can assume that the systematic and statistical errors can be treteaded in the same way.

To compute the final correlation matrix, $V^{tot} \in \Re(n \times n)$, one has to compute the statistical and systematic correlation matrices and to combine them, using the BLUE technique described later (see Section 9.4).

9.3.1 The Correlation Matrix of Statistical Errors

To compute the correlation matrix of the statistical errors, V^{stat}, one has to start from the error matrix, $E^{stat} \in \Re(n \times 1)$. Computed as described in Section 9.1, the elements $E^{stat}_{k1} = \sigma^{stat}_k$ are given by the first column of Table 9.6:

$$E^{stat} = (0.89 \quad 1.22 \quad 1.15 \quad 1.03 \quad 1.18) \tag{9.14}$$

The statistical errors are completely uncorrelated between the channels. The elements of their correlation matrix, $V^{stat} \in \Re(n \times n)$, are given by a diagonal matrix:

$$V_{kl}^{stat} = \rho_{kl}^{stat} \cdot E_{k1}^{stat} \cdot E_{l1}^{stat} \text{ with } k,l = 1,5 \tag{9.15}$$

with

$$\rho_{ij}^{stat} = \begin{cases} 1 & if\ i = j \\ 0 & if\ i \neq j \end{cases}$$

9.3.2 The Correlation Matrix of Systematic Errors

In this section one considers that the individual systematic errors within an analysed channel are completely uncorrelated. However, one has to take into consideration the correlation between different channels, due to the same source of systematic uncertainty. To do this, one acts as if they were statistical errors.

By denoting x_i the N sources of systematic errors on which the functions f_k depend, the systematic infinitesimal variation $\delta^{syst} f_k$ is related to the infinitesimal variation δx_i as:

$$\delta^{syst} f_k = \frac{\partial f_k}{\partial x_i} \cdot \delta x_i \tag{9.16}$$

The general formula to combine the errors is [54]:

$$Cov^{syst}(f_k, f_l) = \sum_{i=1}^{N} \sum_{j=1}^{N} \left(\frac{\partial f_k}{\partial x_i}\right) \cdot \left(\frac{\partial f_l}{\partial x_j}\right) \cdot Cov(x_i, x_j) \tag{9.17}$$

where $V_{kl}^{syst} = Cov^{syst}(f_k, f_l)$. One can write the correlation matrix V^{syst} compactly, using matrices, as:

$$V^{syst} = D \cdot V^x \cdot D^T, \tag{9.18}$$

with

$$D_{ki} = \left(\frac{\partial f_k}{\partial x_i}\right). \tag{9.19}$$

In Formula 9.18, one uses the correlation matrix of the sources of systematics errors, $V^x \in \Re(N \times N)$. If the sources of systematic errors are correlated, V^x has the general form:

$$V_{i,j}^x = \rho_{ij}^x \cdot \sigma_i^x \cdot \sigma_j^x.$$

If the sources of systematic errors are completely uncorrelated, as they are considered in the particular case analysed here, their correlation matrix, V^x, takes the diagonal form with its diagonal elements given by $V_{ii}^x = (\sigma_i^x)^2$ and its off–diagonal elements zero.

In Section 9.2, the elements of the error matrix, $E^{syst} \in \Re(n \times N)$, are supposed to arise because of the variation of the source of systematic error x_i through linear variations, $\left(\frac{\partial f_k}{\partial x_i}\right)$, in the measured f_k:

$$E_{ki}^{syst} = D_{ki} \cdot \sigma_i^x \tag{9.20}$$

The matrix elements, $E_{k,i}^{syst}$, of the absolute systematic errors are extracted from the Tables 9.7, 9.8, 9.10 to 9.12 and 9.14 to 9.17:

$$E^{syst} = \begin{pmatrix} 0.00 & 0.00 & 0.00 & 0.01 & 0.00 \\ 0.07 & 0.17 & 0.08 & 0.10 & 0.20 \\ 0.01 & 0.02 & 0.01 & 0.01 & 0.01 \\ 0.01 & 0.01 & 0.01 & 0.01 & 0.01 \\ 0.01 & 0.01 & 0.01 & 0.01 & 0.01 \\ 0.05 & 0.03 & 0.04 & 0.07 & 0.07 \\ 0.04 & 0.02 & 0.02 & 0.08 & 0.02 \\ 0.15 & 0.19 & 0.18 & 0.19 & 0.20 \\ 0.28 & 0.31 & 0.29 & 0.35 & 0.37 \end{pmatrix} \tag{9.21}$$

Therefore, one can write the systematic correlation matrix, $V^{syst} \in \Re(n \times n)$, as a non–diagonal matrix:

$$V_{k,l}^{syst} = \sum_{i=1}^{N} E_{ik}^{syst} \cdot E_{il}^{syst} \tag{9.22}$$

9.3.3 The Correlation Matrix of Total Errors

The total error is produced by combining the statistical and the systematic errors, where x^{stat} and x^{syst} denote the sources of statistical and systematic errors. Since these two types of sources are independent, each function f_k, one operates with a term sensitive to the statistical variations, $\frac{\partial f_k}{\partial x^{stat}}$, and a term sensitive to the systematic variations, $\frac{\partial f_k}{\partial x^{syst}}$. The two sources of errors are completly uncorrelated, with

$$Cov(x^{stat}, x^{syst}) = 0 \tag{9.23}$$

When calculating the correlation matrix of the total errors, $V^{tot} \in \Re(n \times n)$,

$$\begin{aligned} V_{kl}^{tot} &= \left(\frac{\partial f_k}{\partial x^{stat}}\right)^2 + \left(\frac{\partial f_k}{\partial x^{stat}}\right) \cdot \left(\frac{\partial f_k}{\partial x^{syst}}\right) \cdot Cov(x^{stat}, x^{syst}) + \left(\frac{\partial f_k}{\partial x^{syst}}\right)^2 \\ &= V_{kl}^{stat} + V_{kl}^{syst} \end{aligned} \tag{9.24}$$

with V^{stat} and V^{syst} given by Equations 9.15 and 9.22 respectively.

The correlation matrix of the total errors for the present analysis has the form below, where the correlation coefficients between the channels are shown in parenthesis in the left–bottom part.

$$V^{tot} = \begin{pmatrix} \sigma_i\sigma_i & \rho_{ij}\sigma_i\sigma_j \\ (\rho_{ij}) & \sigma_j\sigma_j \end{pmatrix} = \begin{pmatrix} 0.90 & 0.13 & 0.12 & 0.14 & 0.15 \\ (.11) & 1.65 & 0.14 & 0.17 & 0.19 \\ (.10) & (.09) & 1.47 & 0.15 & 0.16 \\ (.13) & (.12) & (.11) & 1.24 & 0.19 \\ (.13) & (.12) & (.11) & (.13) & 1.61 \end{pmatrix} \tag{9.25}$$

9.4 Combining Correlated Estimates of a Single Quantity using the BLUE Technique

The Best Linear Unbiased Estimate (BLUE) technique makes full use of the correlation matrix. This method is described in [55], or, in more detail, in [56]. The BLUE estimator is a particular case ($z_p = 0$ for $\forall p = 1, m$, and $m = 1$) of affine transformation g, whose most general expression is written as:

$$g_p = \sum_{k=1}^{n} W_{pk} f_k + z_p$$

with $W \in \Re(m \times n)$ and $z \in \Re(m)$. It is widely used because it provides an estimate which has the minimum variance σ^2 among all affine estimators.

Let f_k ($k = 1..n$) be the unbiased estimates one has to consider. Weights, w_k, are assigned in order to compute the linear estimator:

$$f = \sum_{k=1}^{n} w_k \cdot f_k, \tag{9.26}$$

where the sum of all the weights has to be unity:

$$\sum_{k=1}^{n} w_k = 1 \ . \tag{9.27}$$

The variance of the measured branching ratio is given by:

$$\sigma^2 \;=\; \sum_{k,l=1}^{n} w_k \cdot V_{kl}^{tot} \cdot w_l \qquad (9.28)$$

The problem of finding the best estimator f, of variance σ, reduces itself into finding the set of weights w_k, subject to the Equation 9.27, which minimizes σ^2. In order to compute the weighting factors, from Equation 9.27, one can extract a particular w_k, for example w_n. Then, one can minimize σ^2, given by Equation 9.28, with respect to the remaining w's (therefore, with respect to $w_1 ... \; w_{n-1}$), which are regarded as independent.

Alternatively, one can use the method of Lagrangian multipliers to give:

$$w \;=\; V^{tot^{-1}} U / (U^T V^{tot^{-1}} U) \qquad (9.29)$$

where $V^{tot^{-1}}$ is the inverse of matrix V^{tot} and U^T is the transpose of the linear matrix $U \in \Re(n \times 1)$. Each of the components of this matrix is equal to unity:

$$U_{k1} = 1, \; \forall k = 1, n \; .$$

9.5 The Final Error and its Components

Five estimates, $f_k = BR_k$, of the measured branching ratio are produced by the present analysis. Each estimate corresponds to one of the five different decay channels considered. Using the techniques described in Section 9.4, these measurements are weighted by the factors shown in Table 9.18. In this table, the values of the individual total errors $\sigma^{tot}(BR)$ represent the square roots of the diagonal elements of the matrix from Equation 9.25.

Channel	weight	BR in %	$\sigma^{tot}(BR)$ in %	$\sigma^{stat}(BR)$ in %	$\sigma^{syst}(BR)$ in %
(a)	0.32	7.82	0.95	0.89	0.33
(b)	0.15	9.37	1.28	1.22	0.40
(c)	0.18	9.38	1.20	1.15	0.35
(d)	0.20	9.75	1.11	1.03	0.42
(e)	0.14	10.30	1.27	1.18	0.47
Average		9.09	0.61	0.48	0.38

Table 9.18: *Input values and results in the weighting procedure applying the BLUE technique*

In order to describe the method of computing the values of the errors shown in the last line of Table 9.18, one denotes by y a given source of errors in the

present measurement. The variation of the average value $f = \overline{BR}$, due to variation δy, will be:

$$\begin{aligned} \delta^y f &= \delta^y(\textstyle\sum_{k=1}^n w_k f_k) = \sum_{k=1}^n w_k \delta^y(f_k) \\ &= \textstyle\sum_{k=1}^n w_k \ \frac{\partial f_k}{\partial y} \ \delta y. \end{aligned} \tag{9.30}$$

The variance of f is:

$$\begin{aligned} Var^y(f) &= < f^2 >_{|y} - < f >_{|y}^2 \\ &= < (\textstyle\sum_k w_k f_k)^2 >_{|y} - < \sum_k w_k f_k >_{|y}^2 \\ &= \textstyle\sum_{k,l} w_k \ w_l \ (< f_k f_l >_{|y} - < f_k >_{|y} < f_l >_{|y}) \\ &= \textstyle\sum_{k,l} w_k \ w_l \ V_{kl}^y \\ \sigma^y &= \sqrt{Var^y(f)} \end{aligned} \tag{9.31}$$

The total statistical error is an example of the particular case when there does not exist a correlation between the channels. Applying Equations 9.31 and 9.15 one obtains:

$$\sigma^{stat} = \sqrt{\sum_{k=1}^n w_k^2 (\sigma_k^{stat})^2} = 0.48 \tag{9.32}$$

For the systematic errors, the values are correlated between the different channels. Applying Equations 9.31 and 9.22 one obtains:

$$\sigma^{syst} = \sqrt{\sum_{k,l=1}^{n} w_k \ w_l \ V_{kl}^{syst}} = 0.38 \tag{9.33}$$

Using the same reasoning as for deriving Equation 9.22, for each of the sources of systematic errors x', one has:

$$V_{k,l}^{x'} = E_k^{x'} \cdot E_l^{x'} \tag{9.34}$$

The individual contributions of each source of systematic uncertainty, computed using Equations 9.31 and 9.34, are shown in Table 9.19.

One can observe that the largest largest systematic uncertainty is generated by the lepton modelling uncertainty, while the second largest is due to lepton identification efficiency. Therefore, the main experimental systematic uncertainty comes from the lepton selection procedure, and not from the charmed quark selection. In the charm selection procedure the main uncertainty is

Source of systematic error	Value of error
b and c fragmentation	0.11
gluon splitting	0.02
B mixing	0.01
b–tag efficiency	0.01
wrong D charge assignment	< 0.01
uncertainties in lepton BR's	0.05
lepton background	0.04
lepton identification efficiency	0.12
lepton modelling	0.31
Total systematic error	0.38

Table 9.19: *Composition of the total systematic uncertainty.*

given by the b and c fragmentation model, while the error due to the incorrect D charge assignment is very small and it can be neglected.

Chapter 10

Discussion of the Results

In the first part of this chapter different consistency checks of the previous results are presented. One verifies the stability of the result with respect to variations of the mass cut in the distributions of the D meson mass, and to year-by-year variations in data and MC. The present ALPEH result with other ALEPH results obtained making use only of partial ALEPH data samples or using a slightly different procedure of fitting signal candidates. The identical results within statistical fluctuations give confidence in the method used.

In the second part, the final results of the analysis are summarised. Following this, the impact of the presult result on the present world average is calculated.

In the third part, the result of this analysis is put in the light of previous and contemporary experiments, comparing the ALEPH result with the results of other collaborations, making use of different data samples and of more or less different procedure of fitting the signal candidates. This is followed by comments on the prospect of further improvement by future experiments.

10.1 Consistency Checks

10.1.1 Variation Within the Time of Data Acquisition

In order to check for possible effects related to changes in the detector, the analysis was performed separately, for each year of data taking. Distinct samples of MC simulated events have been generated for every year of data acquisition (see Table 4.1). This was performed in order to mimic the variations in the data sample because of the variations in the experimental set-up.

The results for each year were obtained from data and MC events selected from samples corresponding to the same year. However, the Neural Nets used and trained for the total sample of events (see Chapters 6 and 7) have been maintained. The NN retraining, based only on MC events belonging to the analysed year, would have been difficult because of small statistics available (especially for the year 1991).

Year	(a) $in\%$	(b) $in\%$	(c) $in\%$	(d) $in\%$	(e) $in\%$
1991	11.92 ± 5.33	9.89 ± 8.48	10.39 ± 4.40	11.08 ± 3.66	12.13 ± 4.92
1992	11.26 ± 2.96	10.57 ± 3.30	10.29 ± 3.92	10.57 ± 1.71	9.58 ± 3.13
1993	6.93 ± 2.07	7.45 ± 3.16	9.70 ± 2.45	10.04 ± 1.91	9.45 ± 2.68
1994	8.38 ± 1.53	6.44 ± 3.12	10.23 ± 2.38	8.63 ± 1.76	8.81 ± 1.74
1995	4.70 ± 1.48	12.85 ± 3.00	6.47 ± 2.03	7.99 ± 1.68	8.96 ± 2.82
Average	7.82 ± 0.89	9.37 ± 1.22	9.38 ± 1.15	9.75 ± 1.03	10.30 ± 1.18

Table 10.1: *$BR(c \to l + X)$ computed separately for the samples corresponding to each of the five years. The quoted errors are statistical ones.*

In Table 10.1 statistical errors are also shown for each of the computed branching ratios. The numbers presented in the last line of this table represent the values extracted analysing the full samples of data and MC, collected during all five years. The large differences in the size of the samples corresponding to each specific year (see Table 4.1) gave rise to large variations in the mean value and statistical variance of the extracted branching ratio.

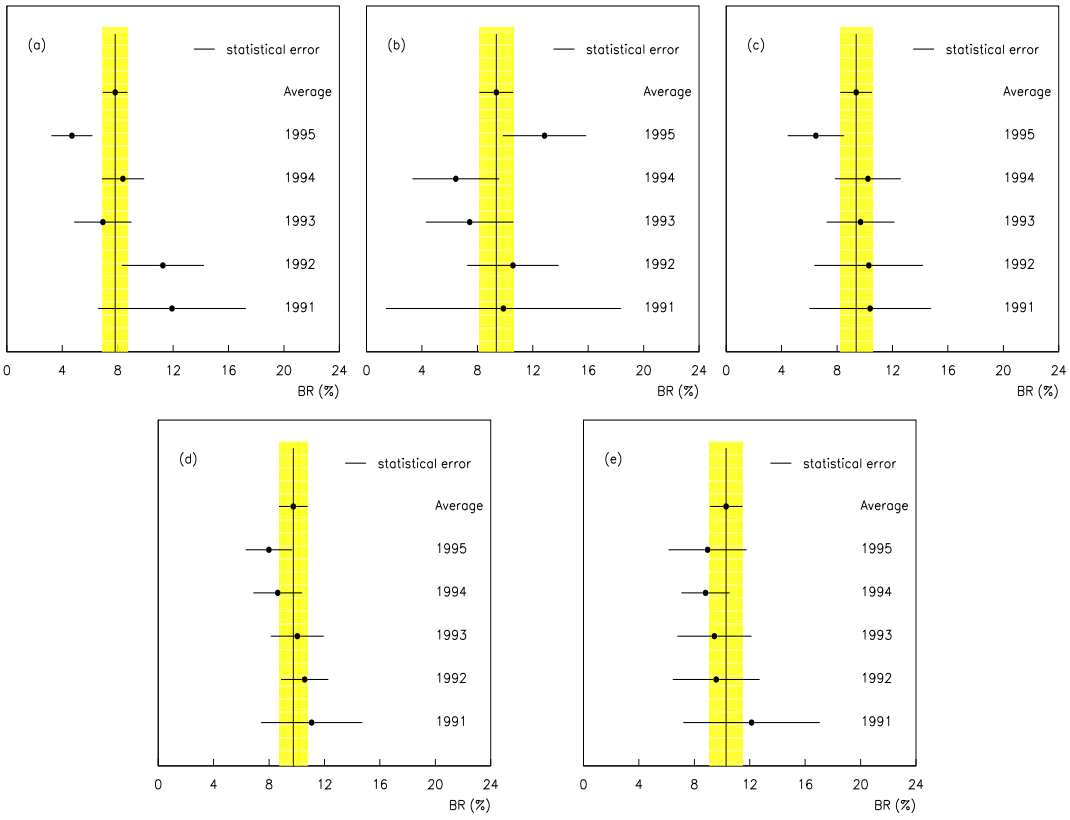

Figure 10.1: *Fitting channel each of the channels, (a) to (e), using samples of MC and data events corresponding to each of the analysed years.*

As one can see also in Figure 10.1, the different subsets over the years give

statistical compatible results with the average value obtained using the total sample of data. The five different channels also give the same results within the stated statistical errors, as can bee seen by comparing the numbers in the last row of Table 10.1. One is, therefore, entitled to average of the full experiment (the five years, 1991 to 1995, and the five channels, (a) to (e)) in order to obtain the final result.

10.1.2 Variations of the Mass Cut $3\sigma_{MC}$

The stability of the result is studied as a function of the mass cuts which are made in the final plots for the mass distribution of the D meson (see Table 7.3).

The resonance of the mass distribution should be described in data by the same Gaussian function in MC and real data. The mass window in which the signal is analysed was chosen to be $\mu_{MC} \pm 3\sigma_{MC}$, both for MC and data events. Here μ_{MC} and σ_{MC} are the mean and the variance of the mass distribution, as fitted from the MC events.

The impact of a change in the mass range cut in the selected events on the fitted branching ratios has been studied using two different approaches. The first was to vary the $3\,\sigma_{MC}$ width of the mass cut from $2.5\,\sigma_{MC}$ to $3.5\,\sigma_{MC}$. The second approach was to repeat the whole analysis using the parameters of the Gaussian as fitted from real data .

Variations of number of σ's

Assuming a Gaussian distribution of the D meson mass, a mass window of $3\,\sigma$ selects 99.73% of the events. Performing the cut inside a 3.5 σ window around the mean, one selects 99.95% of the events; while performing it inside $2.5\,\sigma$ selects 98.76% of the events. Therefore, a variation between $2.5\,\sigma$ and $3.5\,\sigma$ corresponds to a small variation of 1.19% in the number of D candidates fitted by the Gaussian peak. However, since the combinatorial background lying under the Gaussian peak has an almost linear shape, the systematic variation of this is approximately 30% (proportional to the relative variation of the mass window).

In this study the mass window of 3 σ_{MC} around μ_{MC}, was varied by 1 σ_{MC}, as shown in Figure 10.2. The analysis was completely redone for a mass window of 2.5 σ_{MC} and for one of 3.5 σ_{MC}. The parameters used are presented in Table 10.2.

The shift between $BR_{2.5\ \sigma}$ and $BR_{3.5\ \sigma}$, quoted as $\Delta_{(2.5\to3.5)\sigma_{MC}}$, is shown in the second column of Table 10.3. It is due to the variation of the proportion and number of the combinatorial background events among the selected D candidates. The final $BR(c \to l + X)$ changes are smaller than the statistical fluctuations σ_{stat}, indicated in the last column of the same table.

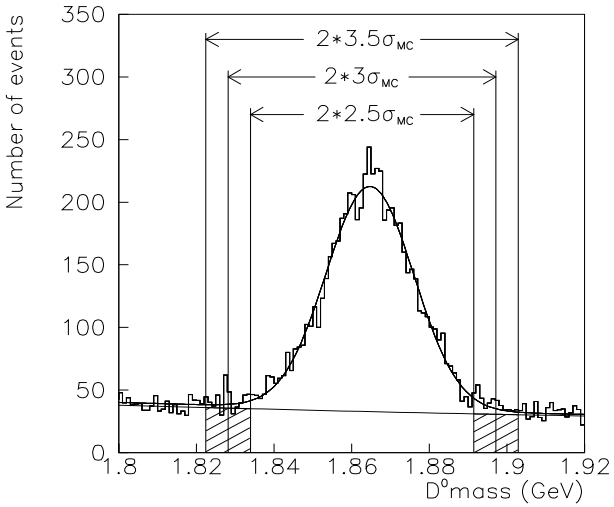

Figure 10.2: *Varying the mass cuts within $1\sigma_{MC}$*

Channel	Type of D meson	μ_{MC} (GeV)	μ_{Data} (GeV)	$\mu_{experim}$ (GeV)	σ_{MC} (GeV)	σ_{Data} (GeV)
(a)	D^0	1.8645	1.8661	1.8645	0.0118	0.0126
(b)	D^0	1.8722	1.8636	1.8645	0.0295	0.0303
(c)	D^0	1.8647	1.8659	1.8645	0.0091	0.0100
(d)	D^0	1.8627	1.8665	1.8645	0.0115	0.0116
(e)	D^+	1.8694	1.8710	1.8690	0.0106	0.0115

Table 10.2: *Parameters of the Gaussian distribution fitting the resonance in the mass of the analysed D mesons. The last column shows the current experimental width [9].*

Using σ_{Data} instead of σ_{MC}

In this analysis the parameters of the cut in the D–meson mass distribution were retrieved using MC events. To take into account the differences between the distributions of the D meson mass in data and in MC, a fit of the mass distribution in data was also performed. The new parameters that were obtained, σ_{Data} and μ_{Data}, were used to assign the mass window cuts when repeating the analysis.

Table 10.2 shows the parameters of the fitted Gaussian distribution, for MC (σ_{MC}, μ_{MC}) and for data (σ_{Data}, μ_{Data}) events, for each analysed channel. The fitted values agree inside their errors with the best known [9] experimental mass values $\mu_{experim}$ which have an error of $\sigma_{experim}$=0.0005 GeV.

The variation in the width of mass distribution, of $< 5\%$, because of the change $\sigma_{MC} \rightarrow \sigma_{Data}$, implies a variation of about 5% of the combinatorial background (as in the case presented before). The variation in the mean of the distribution produces a shift of the mass window (using the parameters fitted from the MC selects the events from the region A_1, while using the

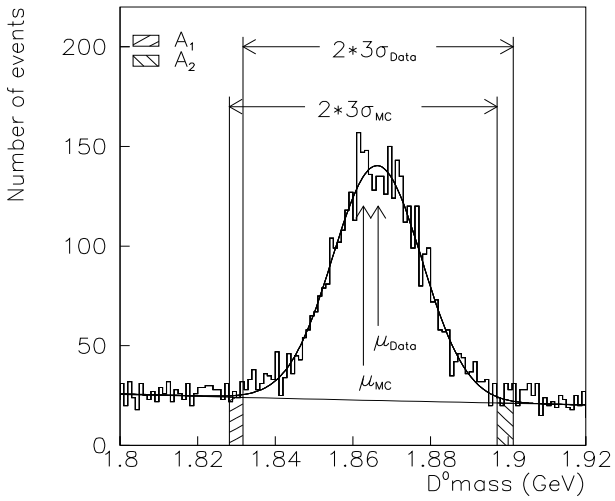

Figure 10.3: *Varying the 3σ cut, with σ fitted from MC and real data, respectively.*

parameters fitted from data selects instead the events from the region A_2, as shown in Figure 10.3). The variation in the mean of the distribution, of the order of 0.1–0.3 σ, corresponds to a change of about 0.4% in the number of selected true D meson candidates fitted by the Gaussian peak.

The difference between $BR_{\sigma_{MC}}$ and $BR_{\sigma_{Data}}$, quoted as $\Delta_{\sigma_{MC}\to\sigma_{Data}}$, is shown in the third column of Table 10.3. It is due to a variation of the proportions and numbers of the different components of the selected sample of D candidates. The computed $BR(c \to l + X)$ changes again within the statistical fluctuations (σ_{stat}) for each of the analysed channels.

Channel	$\Delta_{(2.5\to3.5)\sigma_{MC}}$ $in\%$	$\Delta_{\sigma_{MC}\to\sigma_{Data}}$ $in\%$	σ_{stat} $in\%$
(a)	0.41	0.11	0.89
(b)	1.03	0.40	1.22
(c)	0.60	0.10	1.15
(d)	0.10	0.10	1.03
(e)	0.30	0.10	1.18

Table 10.3: *Stability Checks.*

10.2 The Final Result and Overall Discussion

Following Equations 5.4, 7.13 and 8.19, the five branching ratios shown in Table 9.18 are obtained. The three equations summarise the procedure of going from data to the final result.

The final result, obtained using the BLUE technique (see Section 9.4) , is:

$$\begin{aligned} BR(c \to l + X) &= 9.09 \pm 0.48^{(stat)} \pm 0.38^{(syst)} \ \% \\ &= 9.09 \pm 0.61^{(tot)} \ \% \end{aligned} \tag{10.1}$$

The relation between the result for each channel, and the averaged result, can be seen in figure 10.4. One can observe that all the measurements are consistent, with no one result significantly biasing the average.

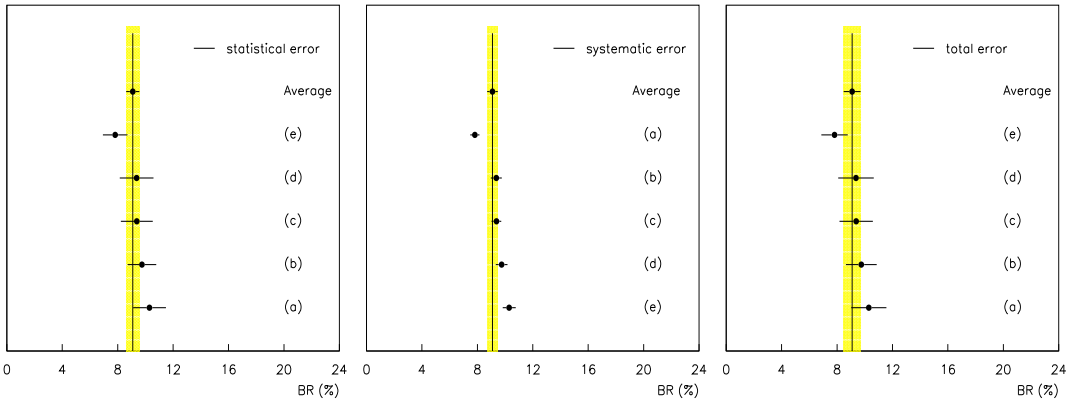

Figure 10.4: *Final result and the results for each of the channels, (a) to (e), showing the statistical, the systematic and the total errors.*

The present measurement is limited by the statistical error; it can therefore be improved with more data. Since one works in a three dimensional space to make the cuts for selecting the charmed D candidates, it is difficult to visualise them all at the same time, or the effect they have. However, the systematic errors play a major role due to their correlations. Taking into account non-diagonal terms of their correlation matrix rises the total error from 0.5% to 0.6%, the two largest systematic errors being due to lepton modelling and lepton detection efficiency. An improvement in future studies would be to vary the working point in order to reduce the total error by optimising both the statistical and systematic errors together.

By considering the present result as uncorrelated to the actual world average of 9.90±0.37% ([9]), the new world is:

$$BR(c \to l + X)^{new}_{world\ average} = 9.68 \pm 0.32\% \tag{10.2}$$

However, the systematic errors of the LEP experiments have to be considered partially correlated, since all the LEP experiments use the same recipe and values to describe the uncertainties in lepton and charm hadron branching

ratios, for example the lepton modelling and b and c fragmentation. Therefore, this analysis gives an improvement of about 10% over the previous world average.

The present result can be compared with the theoretical prediction of the spectator model (see Section 2.6.2), which is based on the idea of independent couplings. Here, one expects that the measured branching ratio would be approximately the same for all the decay channels. This prediction of the spectator model is compatible with the present results.

Accurate and precise knowledge of the direct inclusive semileptonic branching ratio of c hadrons $BR(c \to l + X)$ (where $l = e$ or μ), provides the opportunity to improve the theoretical models on the dynamics of heavy hadrons. This will have important physics implications for future experiments, such as the LHC, where heavy hadrons will be produced in large amounts.

10.3 Comparison to Other Measurements

The current world average of $BR(c \to l + X)$ is based on results from past (ARGUS, MARK2, JADE, DELCO) and contemporary (OPAL) measurements, with respect to the present one. The $BR(c \to l + X)$ results from all the above experiments are summarised in Figure 10.5.

This section presents an overview of these measurements, as well as of the other LEP measurement performed in the meantime by DELPHI, and which is not yet included in the world average.

10.3.1 Comparison to Past Measurements

In order to put the presented analysis in a wider context, a brief summary of some of the various past measurements is given. ARGUS, MARK2, JADE and DELCO studied $\gamma \to c\overline{c}$.

DELCO

The DELCO measurement was done only for electrons. Their $BR(c \to e$ issued from data taken at the SLAC storage ring PEP, where e^+e^- annihilated at a centre-of-mass energy of 29 GeV.

The analysis [6] was based on the fits of momentum and transverse momentum distributions of electrons, where the contributions from $b \to ce^-\overline{\nu}_e$, $b \to c \to se^+\nu_e$ and $c \to se^+\nu_e$ were unfolded. A total number of 2101 electron candidates was used. They fitted three free parameters because, in addition to the branching ratio of interest, the Peterson fragmentation parameters ξ_b and ξ_c were also fitted.

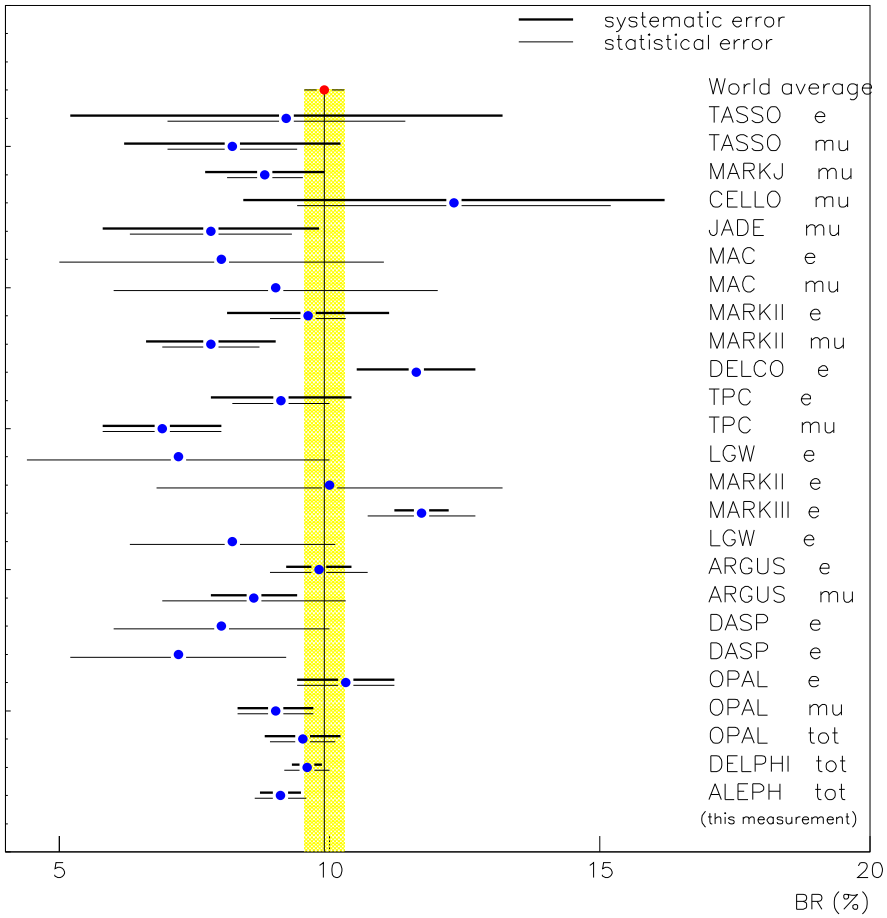

Figure 10.5: *Comparison of different $BR(c \to l)$ measurements*

MARK II

MARK II was also, as DELCO, a detector at the SLAC storage ring PEP. For this analysis the center of mass energy was 29 GeV. Their results [4], using both the muon and the electron data sample, were based on their full data sample of $204\,\mathrm{pb}^{-1}$.

After preselection cuts, used to reduce the background events, one was left with a sample of candidates made of 2621 electrons and of 1230 muons.

The fit of the p and p_t distributions was achieved by putting the branching ratios $\mathrm{BR}(b \to l)$, $\mathrm{BR}(c \to l)$ and the mean of the Peterson fragmentation function for b hadronisation, $< \xi_b >$, as free parameters. Another free parameter was a scaling factor for the background distribution, which was simulated in an earlier step. The $< \xi_c >$ was set to 0.68 ± 0.06, and could vary in the error range.

JADE

The JADE analysis [5] was based on data taken with the JADE detector at PETRA using e^+e^- events at a centre-of-mass energy of 34.6 GeV.

After a first preselection, the analysis started with 959 muon candidates which were attributed to 5 different channels:

- $b \to c\mu^-\overline{\nu}_\mu$
- $c \to s\mu^+\nu_\mu$
- decay muons arising from charged pions
- decay muons arising from kaons
- secondary decays in b events

The momentum and transverse momentum distributions were then fitted by varying the branching ratios, the fragmentation parameters and the background fractions. Different definitions of z (the fraction of energy taken away by the produced hadron) were considered (see Section 2.5.2).

ARGUS

This measurement was using the DORIS II e^+e^- storage ring, at an energy around 10 GeV. In comparison to the previously presented experiments, this analysis used a new approach, which consisted, as is the case for most recent BR($c \to l$) determinations, in using reconstructed D^{*+} mesons and searching for a lepton with the correct sign in the opposite hemisphere.

The following channels have been used [2]:

$$\begin{aligned} D^{\star +} \quad \to \quad & D^0\,\pi_s^+ \\ & \hookrightarrow K^-\,\pi^+ \\ & \hookrightarrow K^-\,\pi^+\,\pi^-\pi^+ \\ & \hookrightarrow K_s^0\,\pi^+\pi^- \end{aligned}$$

After preselection cuts, and a cut in the invariant mass distribution, one ended with a subsample of 2693, 2969 and 617 events for each of the above channels, giving a total of 6279 events. The background was determined by using a Gaussian fit above a linear background applied to the invariant mass distribution

For these events the experiment found 240±21±3 electron and 69±13±4 muon signal events.

After a correction for the lepton identification efficiencies down to lower momenta, $507 \pm 47^{29}_{27}$ electron events and $445 \pm 87 \pm^{41}_{36}$ muon events were found.

10.3.2 Comparison to Contemporary Measurements

All the measurements performed by the LEP I collaborations, including the present one, were done at the same energy. One major question was if the $BR(c \to l)$ is dependent on the energy of the charm.

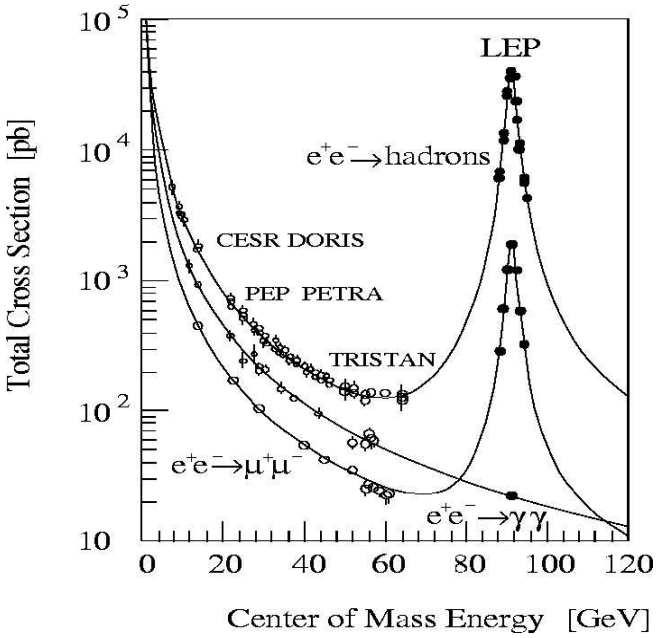

Figure 10.6: *Total e^+e^- cross section from CESR/DORIS to LEP energies*

The LEP experiments, OPAL, DELPHI and the ALEPH present measurement, confirmed that the branching ratio is independent on the charm energy. Figure 10.6 (courtesy of Toshinori Mori) shows the centre-of-mass energies at which measurements have been performed at various accelerators.

OPAL

The analysis undertaken by the OPAL collaboration [7] was based on five $D^{\star+}$ decaying channels:

$$\begin{aligned} D^{\star+} \quad \rightarrow \quad & D^0\,\pi_s^+ \\ & \hookrightarrow K^-\,\pi^+ \\ & \hookrightarrow K^-\,\pi^+\,\pi^0 \\ & \hookrightarrow K^-\,\pi^+\,\pi^-\pi^+ \\ & \hookrightarrow K^-\,e^+\,\nu_e \\ & \hookrightarrow K^-\,\mu^+\,\nu_\mu \end{aligned}$$

The principle of the measurement [7] is similar to the one used by the present analysis, where leptons with the correct charge correlation are searched in the hemisphere opposite to a detected $D^{\star+}$. The analysis has also been performed using NN, but during the second step of the analysis, to discriminate the lepton candidate from possible background.

The first set of cuts include the cosine of the helicity angle, the mass difference $\Delta M = M_{D^{*+}} - M_{D^0}$, the mass M_{D^0}, the scaled energy $E_{D^{*+}}/E_{beam}$

and the probability to have identified the K^-. A total of 27662 candidates from all the five channels remained.

The combinatorial background was subtracted from this sample on a statistical basis using an independent set of background candidate events. The contributions from gluon splitting was subtracted using multiplicity arguments. After these corrections the remaining sample contained 15784±99 $D^{\star+}$ events, with a charm purity of $f_c = 77.4 \pm 0.8 \pm 2.2\%$.

The efficiency to detect a lepton was computed using Monte Carlo simulations and found to be: $\epsilon^e = 30.2 \pm 0.7\%$ and $\epsilon^\mu = 43.3 \pm 0.8\%$. The background due to $b \to l$ and $b \to c \to l$, as well as the combinatorial background, were subtracted from the data using a sample of ($D^{\star+}$, l^+) events. A correction due to the fact that the combinatorial background was different for the ($D^{\star+}$, l^+) and ($D^{\star+}$, l^-) sample was applied. The total number of leptons originating from charm decays was estimated to be 378±31 for the electrons and 476±40 for the muons.

DELPHI

This analysis [8] used data collected between 1992 and 1995 at LEP and is based on a set of D^*, D^0 and D^+ mesons: in total 21898±216 charmed mesons reconstructed with a purity of $f_c = 80.9 \pm 1.1\%$.

The principle was the same as in the previously presented OPAL analysis, and in the present analysis, where the number of identified leptons in the hemisphere opposite to the D mesons was compared to the total number of reconstructed D mesons.

The leptons detection efficiencies were computed from Monte Carlo simulations, and found to be: $\epsilon^e = 51.4 \pm 1.3\%$ and $\epsilon^\mu = 60.8 \pm 1.3\%$. After having subtracted the background due to lepton misidentification, and the background due to true leptons from light particle decays (using the multiplicity of charged particles) a total of 1187±51 leptons was found. The DELPHI analysis used all the seven channels ((*a*)–(*g*)) listed in Section 5.1.

This measurement is compatible with the OPAL[7], DELPHI [8] and past measurements. A summary of the charm semileptonic branching ratios measured so far, including the one presented in this thesis, is given in Table 10.4. When two errors are quoted, the first stands for the statistical, while the second stands for the systematic error. If the measuremet was separately performed for electrons, $BR(c \to e + X)$ and muons, $BR(c \to l + X)$), the table includes both of these measurements, as well as their averaged value, $B(c \to l + X)$, as presented by each collaboration.

10.4 Outlook for Running and Future Experiments

The measurement presented here has the potential to improve in the next few years. For example, the BABAR and BELLE experiments should be

	Experiment	$\sqrt{s}$ (GeV)	$B(c \to e + X)$ (%)	$B(c \to \mu + X)$ (%)	$B(c \to l + X)$ (%)
Petra	TASSO	35	9.2±2.2±4.0	$8.2 \pm 1.2^{+2.}_{-1}$	
	MARK J	35,43		8.8±0.7±1.1	
	CELLO	14,22,34		12.3±2.9 ± 3.9	
	JADE	34		7.8±1.5 ± 2.0	
PEP	MAC	29	8±3	9±3	
	MARK II	29	9.6±0.7±1.5	7.8±0.9±1.2	
	DELCO	29	$11.6^{+1.1}_{-0.9}$		
	TPC	29	9.1±0.9±1.3	6.9±1.1±1.1	
SPEAR	DELCO	3.8	8.0±1.5		
	LGW	3.8	7.2±2.8		
	MARK II	3.8	10.0±3.2		
	MARK III	3.8	11.7±1.0±0.5		
	LGW	4-7	8.2±1.9		
DORIS	ARGUS	10	$9.8 \pm 0.9^{+0.6}_{-0.5}$	$8.6 \pm 1.7^{+0.8}_{-0.7}$	
	DASP	4-5	8.0±2.0 and 7.2±2.0		
LEP	OPAL	91	$10.3 \pm 0.9^{+0.9}_{-0.8}$	$9.0 \pm 0.7^{+0.7}_{-0.6}$	$9.5 \pm 0.6^{+0.7}_{-0.6}$
	DELPHI	91			9.58±0.42±0.28
	ALEPH	91			9.09±0.48±0.38
(this measurement)					

Table 10.4: *Summary of the charm semileptonic branching ratios measurements presently available.*

able to measure the branching ratio, even though they are mainly specialised in b-physics. Many parameters of the c quark can be measured, since large quantities of c quarks would be produced via the $b \to c$ process. However, to measure the branching ratio $BR(c \to l)$, the $b \to l$ modelling has to be both accurate and precise.

Other experiments which are able to achieve improvements are E791, a fixed-target experiment at Fermilab, and CLEO, running at the CESR e^+e^- storage ring. CLEO-C is a future upgrade of the CLEO experiment, designed to study charm physics in detail.

Finally, much hope can be set in TESLA, a e^+e^- linear collider suggested to run at DESY (Hamburg). A number of 10^9 Z^0 events are expected in

the first four months of possible running at the Z^0 resonance. This would significantly decrease the statistical and systematic error on the present measurement. The associated detector is planned to be much closer to the beam pipe than ALEPH was, which would enable impoved vertex resolution. This is an important consideration in heavy flavour physics.

The study of the branching ratio $BR(c \to l)$ within ALEPH has enabled an improvement in the world average for this quantity. This in turn improves the knowledge of high energy particle physics and will help future studies to make the most of their data.

Appendix A

Monte Carlo Methods

Numerical discreet calculation is typically applied to the differential equations describing some underlying physical or mathematical system. In contrast to this conventional calculation, the Monte Carlo methods use statistical simulation. In High Energy Physics (HEP), 4–dimensional quantities are used – describing the connected time and the 3–spatial components. Integrals run over at least one such quantity, hence over a d–dimensional region with $d \geq 4$. Therefore, by using n random numbers to obtain an estimate, the accuracy of the MC, which remains proportional to $n^{-1/2}$ for any number of dimensions d, is better than the accuracy of the numerical methods also using n numbers. The latter is proportional to $n^{-2/d}$ and suffers a loss with the increase of d.

The MC methods are ideal for the complicated HEP boundary conditions, which are due to the mixture of shapes present in the current particle detectors, and to the boosting of the observed variables subject to velocity–related transformations. The MC predicted values of the observed variables vary by repeating the calculations; hence simulating the real life variations due to limited experimental accuracy, or to finite statistics.

In order to study their feasibility, current HEP experiments need extensive MC simulation, from both the event generation and the detector simulation points of view.

The physical process is simulated directly, with only the requirement that the system can be described by probability density functions; or, with even the weaker requirement that the process can be treated as a stochastic process (hence, can have a probability density function attached). Therefore, a Monte Carlo simulation method has to include a set of probability distribution functions (*pdf*'s), describing the physical (or mathematical) system. A random number generator has to be available, to produce unpredictable individual values uniformly distributed on the unit interval. It also has to be given a sampling rule prescribing the sampling required from the specified pdf's. This assumes the availability of random numbers on the unit interval. For the quantities of interest, the outcomes must be accumulated into overall tallies (or scores).

An estimate of the statistical error (variance), as a function of the number of trials and other quantities, must be determined in order for it to be possible to develop variance reduction techniques, which will reduce the computational time for Monte Carlo simulation. The PHYTIA 5.7 [37] program (used to produce the MC physics events on which this analysis is based) used non–parallel computing. The current trend is to use parallel computing architectures. Therefore, algorithms allowing the Monte Carlo methods to be implemented efficiently on these architectures are searched for.

Appendix B

More Diagrams of NN Outputs

Figure B.1 presents the two-dimensional histograms of the NN outputs, for b and uds purities. Thus, one has a good visualisation on the NN selection criteria (see Section 7.2), since the b events have the tendency to cluster at (0,1) - b and not uds events, while the uds prefer the (1,0) corner -non b events which are uds events.

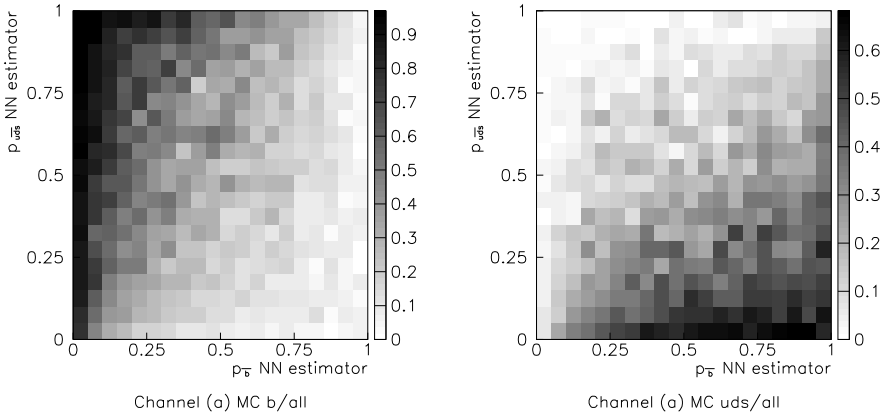

Figure B.1: *Channel (a): $p_{\overline{uds}}$–$p_{\overline{b}}$ diagrams for b and uds quark purities.*

In this appendix the rest, channels (b) to (e), of two dimensional plots on which the cuts in NN outputs is based, are shown.

Hereafter the upper-left plot displays the NN outputs information on all the MC candidates which passed the preselection cuts, while the upper-right plot shows this distribution for real data. The total sample of candidates is splitted in three classes, according to the flavour of the quark q originating from primary $Z^0 \to q\overline{q}$ decay. The middle-left, middle-right and lower-left plots show the $p_{\overline{b}}$ versus $p_{\overline{uds}}$ outputs, as given by the two discriminating NN, for uds, c and b initial quarks, respectively.

The lower-right plot represents the charm purity two-dimensional histogram, with respect to the NN outputs. It is generated by dividing histogram "'MC c quark" by "MC all flavours". As expected, the charm events cluster in the corner (1,1). The box including this corner indicates the cuts which have been applied for the final signal selection - both non b and non uds quarks.

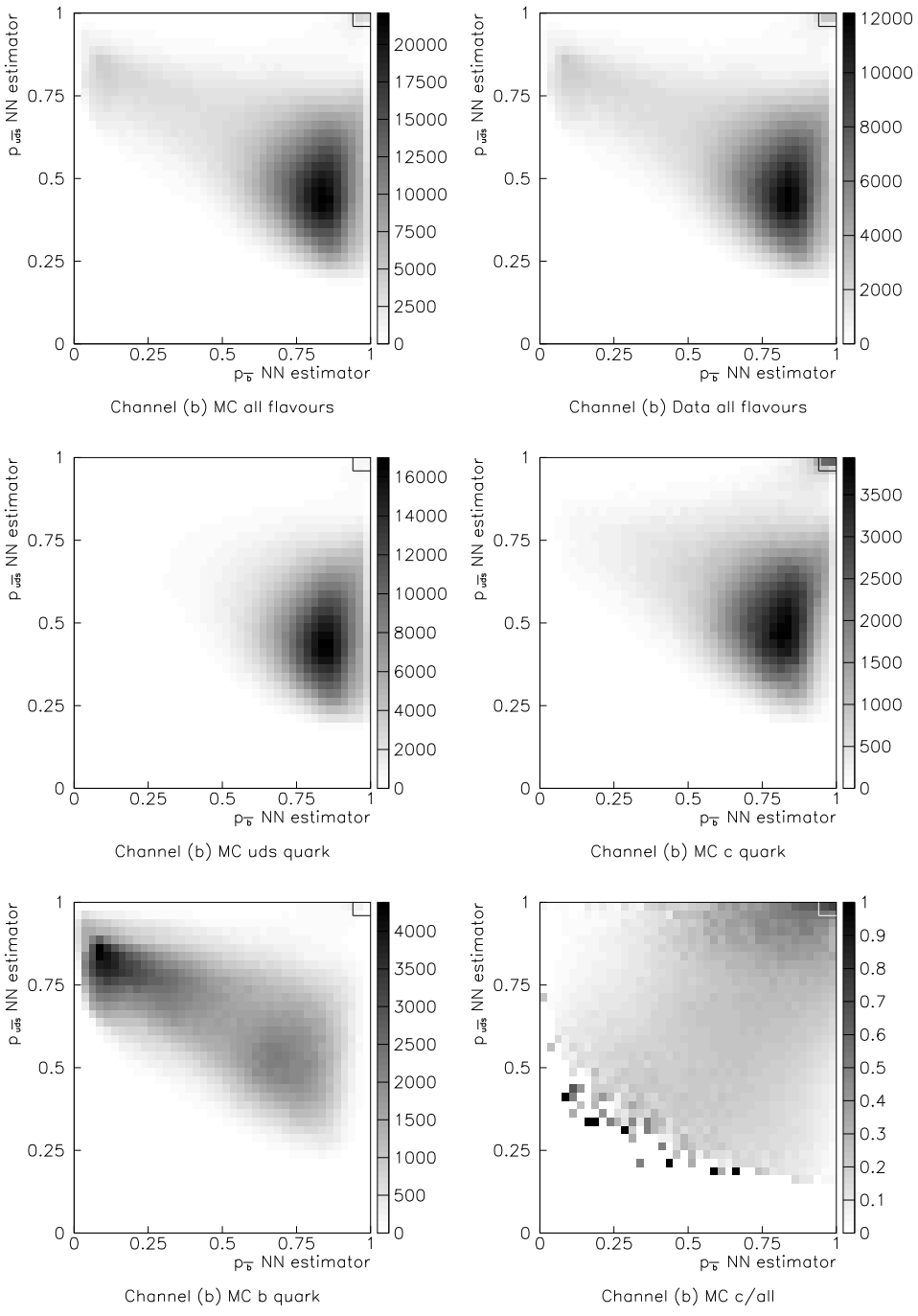

Figure B.2: *Channel (b):* $p_{\overline{uds}}$–$p_{\overline{b}}$ *diagrams.*

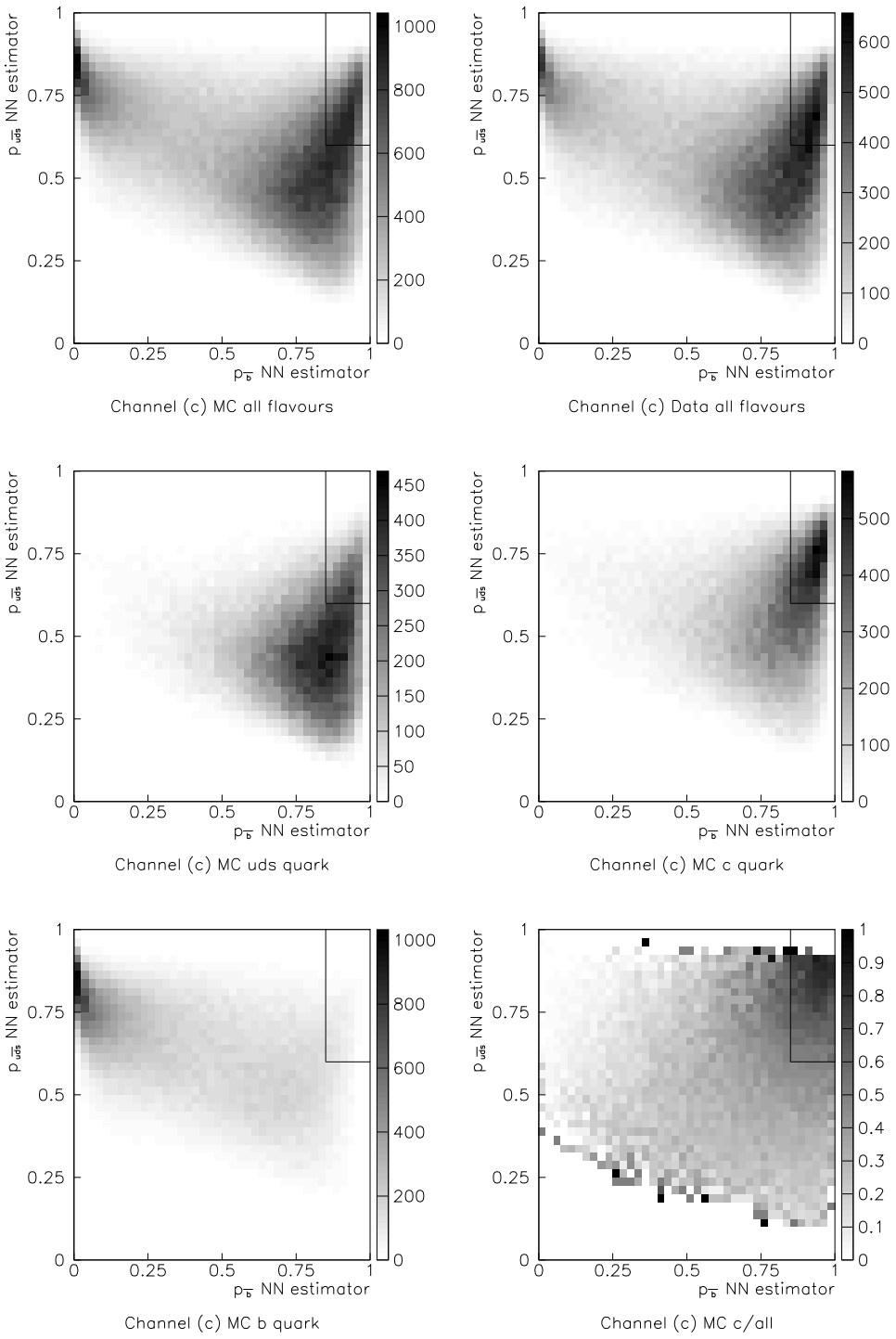

Figure B.3: *Channel (c): $p_{\overline{uds}}$–$p_{\overline{b}}$ diagrams.*

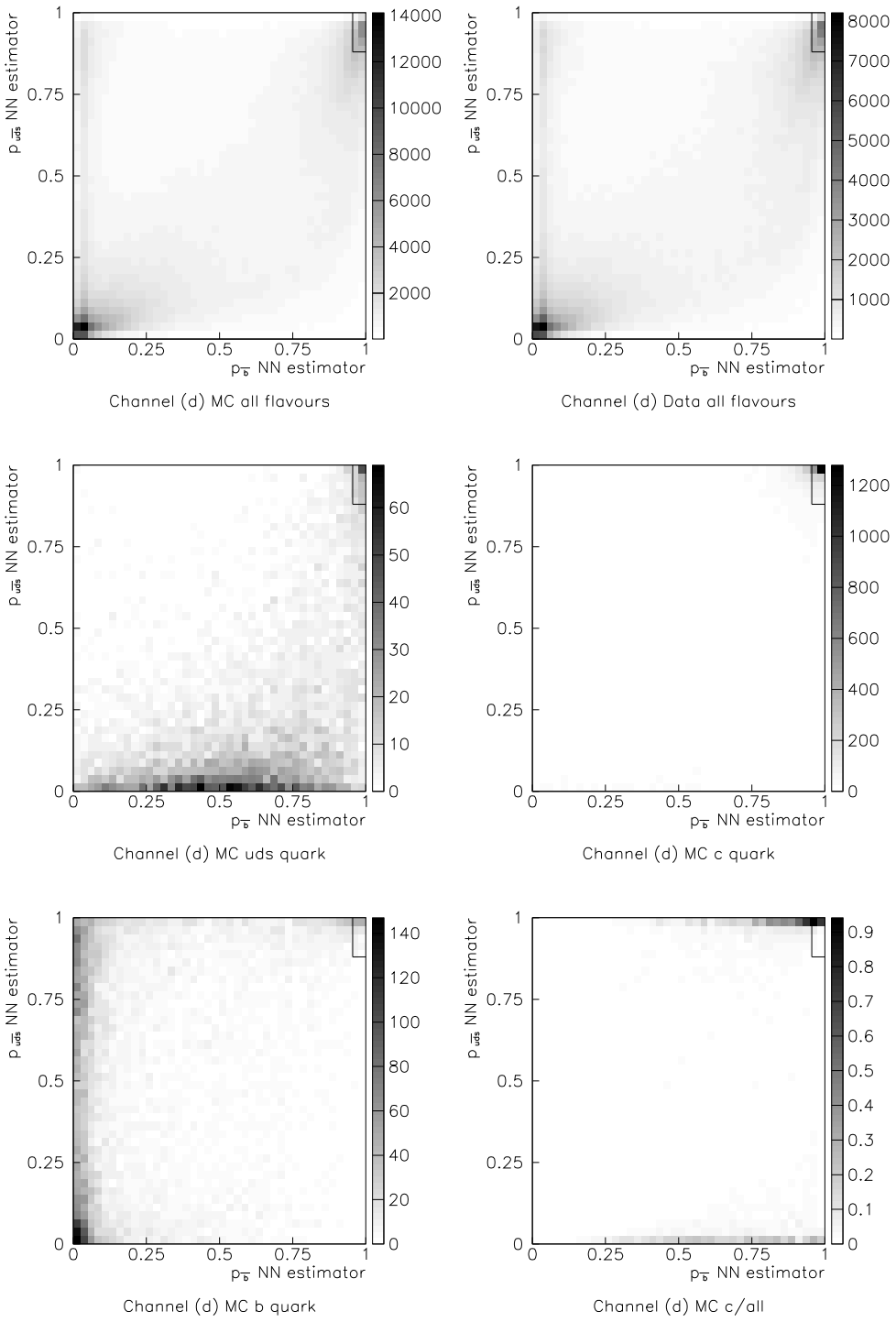

Figure B.4: *Channel (d): $p_{\overline{uds}}$–$p_{\overline{b}}$ diagrams.*

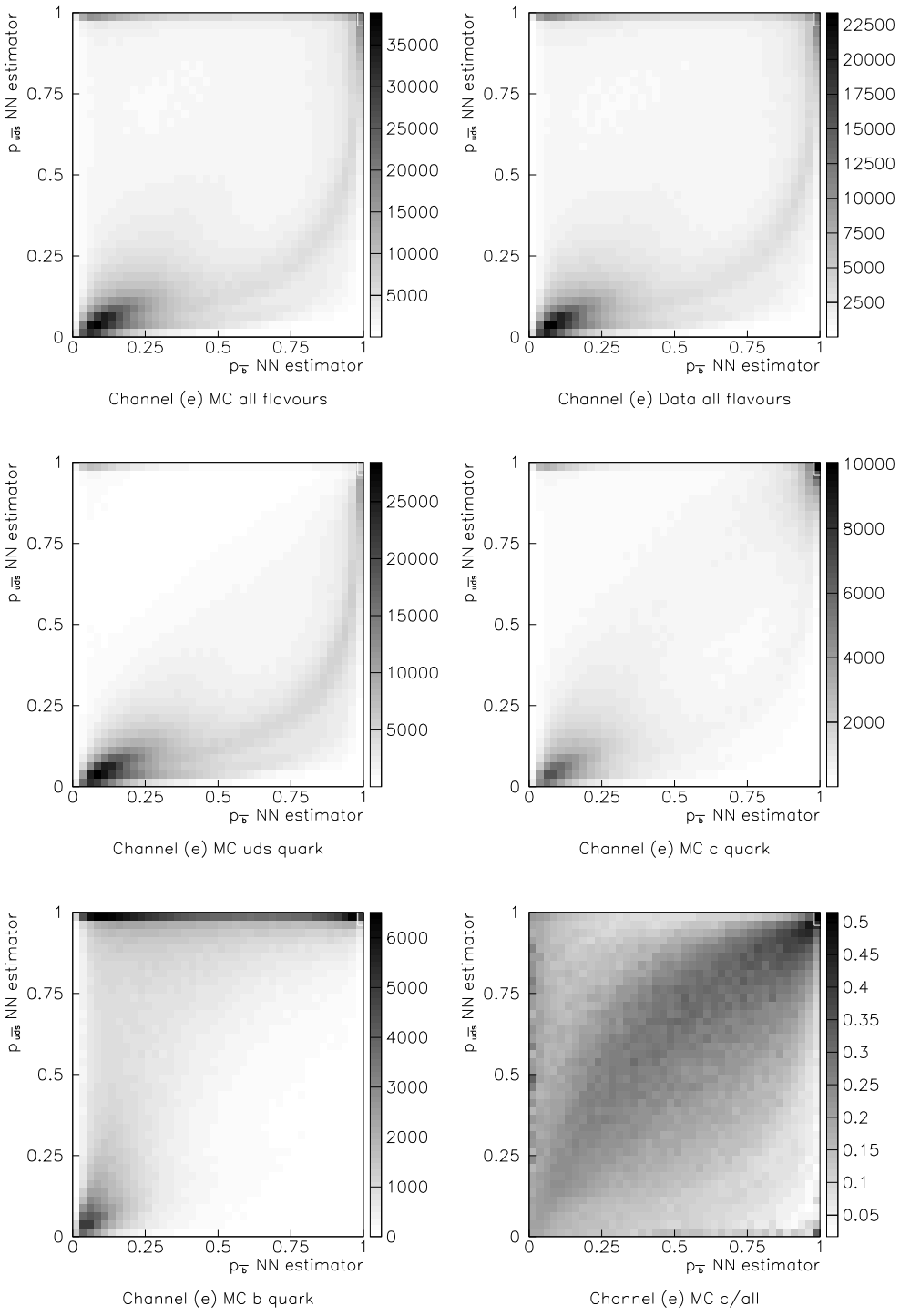

Figure B.5: *Channel (e):* $p_{\overline{uds}}$–$p_{\overline{b}}$ *diagrams.*

Appendix C

Introduction to Probabilities and Statistics

For a discrete variable x, taking one of its values x_i with the frequency P_i, one define its *expectation*, $E(x)$, as:

$$E(x) = \sum_{i=1}^{n} x_i \cdot P_i \tag{C.1}$$

and its *variance*, $V(x)$, as:

$$\begin{aligned} V(x) &= E((x - E(x))^2) \\ &= E(x^2) - (E(x))^2 \end{aligned} \tag{C.2}$$

The standard deviation σ_x is the square root of the variance

$$\sigma_x = \sqrt{Var(x)} \tag{C.3}$$

It is the most commonly used measure of the spread of the variable, especially when working with normal distributions.

A generalization of the variance is the covariance. Given two variables, x and y, the covariance $Cov(x, y)$ shows if they are independent ($Cov(x, y) = 0$), or they depend on one another ($Cov(x, y) \neq 0$):

$$\begin{aligned} Cov(x, y) &= E((x - E(x)) \cdot (y - E(y))) \\ &= E(xy) - E(x) \cdot E(y) \end{aligned} \tag{C.4}$$

Because the covariance is not dimensionless, one can define a dimensionless *correlation coefficient*, ρ, as:

$$\rho = \frac{Cov(x, y)}{\sigma_x \cdot \sigma_y} \tag{C.5}$$

ρ is a number between -1 (if the variables are completely anti-correlated) and $+1$ (if the variables are completely correlated). It is zero if x and y are uncorrelated.

An *estimator* is any function of data, independent of unknown parameters, whose value is intended as a meaningful guess for the value of a parameter.

Acknowledgements

I would like to thank to all those who have made my work and my life in the past almost four years to be so nice.

In chronological order, I should start with Prof. Achim Stahl, who suggested me to become a member of ALEPH, and Dr. Duccio Abbaneo, who initiated and supervised the most of my analysis.

I benefited from the supervision of Prof. Walter Blum through the writing of my thesis, who was carefully going through all the details of my analysis. I thank to Dr. Richard (Matthew) Pearson and Dr. Ronald Settles for eliminating most of my English mistakes. I would like to thank to Dr. Florian Bauer, Prof. Otmar Bibel and Dr. Gennaro Corcella for their helpful comments while reading my thesis.

During the years spent in Munich and in Geneva, I had friends and colleagues without whom this work would have been undoubtly much harder: all the wonderful people from ALEPH, ATLAS/OPAL, HERA-B and theory MPI divisions, and the former or present members of the ALEPH Heavy Flavours group from Pisa.

I would like to thank to my parents, who always have (spiritually and financially:) supported me. Tuturor celor pe care i–am iubit şi–i iubesc.

Bibliography

[1] ALEPH Collaboration, "Measurement of the b forward-backward asymmetry and mixing using high-$p_\perp$ leptons", Phys. Lett. **B 384** (1996) 414

[2] ARGUS Collaboration, "A measurement of the inclusive semileptonic decay fraction of charmed hadrons", Phys. Lett. **B 278** (1992) 202

[3] ARGUS Collaboration, "Measurement of the semileptonic branching fractions of the D^0 meson", Phys. Lett. **B 374** (1996) 249

[4] MARK2 Collaboration, "Inclusive Lepton Production in e^+e^- Annihilation at 29 GeV", Phys. Rev. Lett. Vol. 60 No. **25** (1988) 2587

[5] JADE Collaboration, "Determination of Semi-Muonic Branching Ratios and Fragmentation Functions of Heavy Quarks in e^+e^- Annihilation at $< \sqrt{s} >= 34.6$ GeV", Z. Phys. **C 33** (1987) 339

[6] DELCO Collaboration, "Prompt electron production from the DELCO detector at the SLAC storage ring PEP", Phys. Rev.D Vol.33 No. **9** (1986) 2708

[7] OPAL Collaboration, "Measurement of the Semileptonic Branching Ratio of Charm Hadrons Produced in $Z^0 \to c\overline{c}$ Decays", Eur. Phys. J. **C 8** (1998) 573

[8] DELPHI Collaboration, "Determination of $P(c \to D^{*+})$ and $BR(c \to l^+)$ at LEP 1", Eur. Phys. J. **C 12** (2000) 209

[9] Particle Data Group, C. Caso et al., "Review of Particle Properties"Eur. Phys. J. C **A21292** (2000) 1

[10] I.J.R. Aitchison and A.J. Hey, "Gauge Theories in Particle Physics", Institute of Physics Publishing, Bristol, 2nd Edition (1996)

[11] LEP Experiments and LEP Electroweak Working Group, "A Combination of preliminary LEP Electroweak Measurements and Constraints on the Standard Model", CERN-PPE/95-172 (1995)

[12] LEP Experiments and LEP Electroweak Working Group and SLD Heavy Flavor and Electroweak Group, "A Combination of Preliminary Electroweak Measurements and Constraints on the Standard Model", SLAC-REPRINT-2000-098, CERN-EP-2000-016, (2000) 83

[13] F. Halzen and A.D. Martin, "Quarks and Leptons: An introductory course in modern particle physics", ISBN 0-471-81187-4, (1984)

[14] R.K. Ellis, W.J. Stirlin and B.R. Webber, "QCD and Collider Physics", ISBN 0-521-5819-3, (1996)

[15] C.K.Jung et al., (Super-Kamiokande collaboration) "Oscillations of atmospheric neutrinos", Annu. rev. Nucl. Part. Sci 2001.51 (2001) 451

[16] G. A. Abrams et al, (Mark II collaboration) "Initial measurements of Z boson resonance parameters in the e+ e- annihilation", ,Phys. Rev. Let. **63** (1989) 724

[17] F. Abe et al, (CDF collaboration), "Measurement of the mass and width of the Z^0 boson at the Fermilab Tevatron", Phys. Rev. Let. **63** (1989) 720

[18] G. Arnison et al., (UA1 collaboration), " Further evidence for charged intermediate vector bosons at the SPS collider", Phys. Lett. **B129**, (1983),273

[19] R. Rückl, "Weak decays of heavy quark states", "Elementary particles (Proceedings of the International School of Physics 'Enrico Fermi'; course 92)", ISBN 0-444-87075-X

[20] G. Altarelli at al, "Z Physics at LEP", CERN 89-08, Volume 1, 1989

[21] J.L. Cortes Rückl, "Mass effects in weak decays of heavy particles",Phys. Rev. **D 25** (1982) 188

[22] R. Rückl, "Weak decays of heavy flavours", Habilitationsschrift at the University of Munich, CERN print (1983).

[23] Particle Data Group: Rev. Mod. Phys., **73** (1984) 1

[24] S.L. Glashow, J. Iliopoulos, L. Maiani, "Weak Interactions with leptom-hadron symmetry", Phys. Rev. **D 2** (1970) 1285

[25] M. Kobayashi and T. Maskawa, "CP violation in the renormalizable theory of weak interaction", Prog. Theor. Phys. **49** (1973) 652

[26] M.K. Gaillard and B. W. Lee, "$\Delta I = \frac{1}{2}$ rule for nonleptonic decays in asymptotically free field Theories", Phys. Rev. Lett. **33** (1974) 108

[27] R. L. Kingsley, S.B. Treiman, F. Wilczek, A. Zee, "Weak decays of charmed hadrons", Phys. Rev **D 11** (1975) 1919

[28] J. Ellis, M.K. Gaillard , "On the weak decays of high mass hadrons", Nucl. Phys. **B 100** (1975) 313

[29] G. Altarelli, N. Cabibbo, L. Maiani, "Enhancement of nonleptonic decays of charmed particles" Nucl. Phys. **B 88** (1975) 285

[30] P. Petiau and M. Porneuf, "Proceedings of the XXI International Conference on High energy Physics", Les Editions de Physique, Les Ulis **49** (1982) 631

[31] C. Peterson et al., "Scaling violations in inclusive e^+e^- annihilation spectra", Phys. Rev. **D 27** (1983) 105

[32] S. Myers, E. Picasso, "The LEP Collider", Sci.Am. **263** (1990) 34

[33] G. Marchesini et al., "A Monte Carlo event generator for simulating hadron emission reactions with interfering gluons. Version 5.1", Comp. Phys. Comm. **67** (1992) 465

[34] ALEPH Collaboration, "ALEPH: A detector for electron-positron annihilations at LEP", Nucl. Instr. Meth. **A 294** (1991) 121; ALEPH Collaboration, "Performance of the ALEPH detector at LEP", Nucl. Instr. Meth. **A 360** (1995) 481

[35] J.E. Campagne and R. Zitoun, "Electromagnetic radiative corrections at LEP-SLC energies for experimentalists", Z. Phys. **C 43** (1989) 469

[36] ALEPH Collaboration, "Performances of the ALEPH detector at LEP", Nucl. Instr. Meth. **A 360** (1995) 481

[37] T. Sjöstrand, "High-energy physics event generation with PYTHIA 5.7 and JETSET 7.4" Computer Physics Commun. **82** (1994) 74

[38] T. Sjöstrand, "Z physics at LEP1", Ed. G. Altarelli et al., CERN EP/89-08 (1989), Vol. 3, 259

[39] T. Sjöstrand, "Pythia 5.7 and Jetset 7.4, Physics Manual", CERN TH 7112/93

[40] R. Brun et al., "The GEANT3 electromagnetic Shower Program", CERN DD/EE/84-1 (1987)

[41] Marsaglia and Zaman, "Toward a universal C Random Number Generator", report FSU-SCRI-87-50, Florida State University, 1987

[42] ALEPH Collaboration, "Measurement of the fraction of hadronic Z decays into charm quarks pairs", Eur. Phys. J. **C 4** (1998) 557

[43] ALEPH Collaboration, "Studies of Quantum Chromodynamics with the ALEPH Detector", Physics Reports (1997)

[44] M. Riedmiller and H. Braun, "A Direct Adaptive Method for Faster Backpropagation Learning: The RPROP Algorithm", Proc. ICNN, San Fransisco (1993)

[45] W. Schiffmannet al.,"Comparison of Optimized Backpropagation Algorithms", Proc. ESANN 93 Brussels (1993)

[46] C. Peterson, T. Rognvaldsson, L. Lonnblad "JETNET 3.0: A versatile artificial neural network package", Comput. Phys. Commun. **81** (1994), 185

[47] R.D. Field and R.P. Feynman, "A parametrization of the properties of the quark jets" Nucl. Phys. **B 136** (1978), 1

[48] D. Abbaneo and V. Ciulli, "Feasibility studies for new measurements of R_c and $BR(c \to l)$ in ALEPH" CERN print, ALEPH 98-098, PHYSIC 98-046, (1998), 1

[49] J. Hertz, A. Kroogh, R.G. Palmer, "Introduction to the theory of neural computation", ISBN 0-201-50395-6', Redwood City, (1991)

[50] ALEPH Collaboration, "Heavy quark tagging with leptons in the ALEPH detector",Nucl. Instrum. Meth. **A 346** (1994) 461

[51] ALEPH Collaboration, "A measurement of R_b using a lifetime-mass cut", Physics Letters **B 401** (1997) 150

[52] ALEPH Collaboration, "Inclusive semileptonic branching ratios of b hadrons produced in Z decays", Eur. Phys.J. **C 22** (2002) 613

[53] "Results for the summer 2002 conferences", 31st International Conference on High Energy Physics, ICHEP02, Amsterdam, 2002

[54] R. Barlow, "Statistics: a guide to the use of statistical methods in the Physical Sciences", ISBN 0-471-92295-1', New York, (1989)

[55] L. Lyons et al., "How to combine correlated estimates of a single physical quantity", Nucl. Inst. Meth. **A 270** (1998) 110

[56] K.V. Mardia et al.,"Multivariate Analysis", Academic Press (1979)

[57] F. Becattini, Proceedings of the "Strangeness and Quark Matter 97" conference (Santorini), hep-ph/9708248(1997)

[58] Yi-Jin Pei, " A simple approach to describe hadron production rates in e+ e- annihilation" Z.Phys. **C 72** (1996) 39

List of Figures

1.1 *Diagram symbolising charmed quark production at a primary vertex created by an e^+ e^- annihilation.* 1

2.1 *The B mixing ($\overline{B}^0 \rightarrow B^0$).* 11
2.2 *The charmed hadrons' production mechanism* 12
2.3 *The Peterson fragmentation function for the production of b-hadrons and c-hadrons* 14
2.4 *The c decays via W^+* 15
2.5 *Spectator model for c meson decay* 16
2.6 *Quark description of inclusive heavy-meson decay* 17

3.1 *The LEP accelerator complex at CERN* 19
3.2 *View of the ALEPH detector.* 21
3.3 *The Vertex detector* 22
3.4 *Impact parameter resolution of tracks in $Z^0 \rightarrow qq$ events, where the points are data and the curve is MC simulated.* 23
3.5 *The inner tracking chamber* 24
3.6 *The time projection chamber.* 25
3.7 *The measured dE/dx versus particle momentum* 26
3.8 *The average R_I energy loss separation in standard deviations between particle types as a function of momentum* 27
3.9 *The magnet coil.* 29

4.1 *ALEPH kaon and charged pion momentum distributions in data versus MC* 34
4.2 *ALEPH data versus MC simulated π^0 data* 35
4.3 *Kaons, pions and soft pions momenta in MC, at the truth and at the reconstructed level.* 37
4.4 *Masses of D^0 and D^* mesons, directly reconstructed and as resulting from the D^0 and D^* mesons fitting* 38
4.5 *The relative energy loss for the final decay products tracks and the momenta of the kaon candidates, in MC and data* 39
4.6 *D^* momenta and the angles between the D^0 momentum and the direction of the track of the D^0 candidate, in MC and data* 40

4.7 *The relative decay length of the D^0 candidates and the χ^2 of the D vertex fit, in MC and data* . . . 40
4.8 *The probability of the charmed quark candidate to come from a b quark and the value of the sphericity angle of the event, in MC and data.* . . . 40
4.9 *Momenta of the soft pion and the D^0, and the difference between the reconstructed masses of D^* and D^0, in MC and data* . . . 41
4.10 *The difference between the reconstructed masses of D^* and D^0, in MC and data* . . . 41
4.11 *The NN outputs.* . . . 41
4.12 *The D meson candidates mass peaks* . . . 42

5.1 *Schematic view of the searching procedure* . . . 43
5.2 *Schematic view of an event containing a D^0 and a lepton* . . . 45
5.3 *D^0 event, as viewed by the ALEPH detector.* . . . 46

6.1 *A schematic view of neurons and synapses in biology* . . . 53
6.2 *A schematic view of a multilayer-perceptron.* . . . 54
6.3 *The sigmoid function.* . . . 55
6.4 *An intuitive view of the training process of multilayer perceptron NN* 57

7.1 *Energy loss, in deviations from the average energy loss, for kaons and pions.* . . . 66
7.2 *p_{D^*} distribution.* . . . 70
7.3 *Distribution of the probability P that the D meson came from a b quark.* . . . 70
7.4 *Distribution of the energy loss, $dE/dx(K)$.* . . . 70
7.5 *Distribution of the kaon momentum, p_K* . . . 71
7.6 *Distribution of the decay length significance, l_D/σ_{l_D}* . . . 71
7.7 *Distribution of the angle θ_{p_D,l_D}, between the D directions in momentum and spatial coordinates* . . . 71
7.8 *The decay angle distribution of the D, with respect to sphericity axis* 72
7.9 *$\chi^2(D)$.* . . . 73
7.10 *$m_{D^{*+}} - m_{D^0}$* . . . 73
7.11 *π_{soft}' momentum* . . . 74
7.12 *p_{D^0} momentum distribution.* . . . 74
7.13 *Influence of NN on D^0 mass spectra, in channel $D^{*+} \to D^0\pi^+, D^0 \to K^-\pi^+$, with the decomposition into the flavour classes taken from MC.* 75
7.14 *Influence of NN on D^0 mass spectra, in channel $D^{*+} \to D^0\pi^+, D^0 \to K^-\pi^+\pi^0$, with the decomposition into the flavour classes taken from MC* . . . 75
7.15 *Influence of NN on D^0 mass spectra, in channel $D^{*+} \to D^0\pi^+, D^0 \to K^-\pi^+\pi^-\pi^+$, with the decomposition into the flavour classes taken from MC.* . . . 75

7.16 *Influence of NN on D^0 mass spectra, in channel $D^0 \to K^-\pi^+$, with the decomposition into the flavour classes taken from MC.* 76
7.17 *Influence of NN on D^+ mass spectra, in channel $D^+ \to K^-\pi^+\pi^+$, with the decomposition into the flavour classes taken from MC.* . . . 76
7.18 *Channel (a): $p_{\overline{uds}}$–$p_{\overline{b}}$ diagrams.* 77
7.19 *Channel (a): Normalised D^0 mass distribution before and after the NN cuts for MC and data* 81
7.20 *Channel (b): Normalised D^0 mass distribution before and after the NN cuts for MC and data* 81
7.21 *Channel (c): Normalised D^0 mass distribution before and after the NN cuts for MC and data* 82
7.22 *Channel (d): Normalised D^0 mass distribution before and after the NN cuts for MC and data* 82
7.23 *Channel (e): Normalised D^+ mass distribution before and after the NN cuts for MC and data* 82
7.24 *Combined gaussian and second order polynomial fit in the D mass window.* 86

8.1 *R_T versus R_L for Monte Carlo simulated electrons and charged hadrons* 91

10.1 *Fitting channel each of the channels, (a) to (e), using samples of MC and data events corresponding to each of the analysed years.* 128
10.2 *Varying the mass cuts within $1\sigma_{MC}$* 130
10.3 *Varying the 3σ cut, with σ fitted from MC and real data, respectively.* 131
10.4 *Final result and the results for each of the channels, (a) to (e), showing the statistical, the systematic and the total errors.* 132
10.5 *Comparison of different $BR(c \to l)$ measurements* 134
10.6 *Total e^+e^- cross section from CESR/DORIS to LEP energies* 136

B.1 *Channel (a): $p_{\overline{uds}}$–$p_{\overline{b}}$ diagrams for b and uds quark purities.* 142
B.2 *Channel (b): $p_{\overline{uds}}$–$p_{\overline{b}}$ diagrams.* 143
B.3 *Channel (c): $p_{\overline{uds}}$–$p_{\overline{b}}$ diagrams.* 144
B.4 *Channel (d): $p_{\overline{uds}}$–$p_{\overline{b}}$ diagrams.* 145
B.5 *Channel (e): $p_{\overline{uds}}$–$p_{\overline{b}}$ diagrams.* 146

List of Tables

2.1 *The basic constituents of matter in SM [9]* 5
2.2 *Masses of the Gauge Bosons in the SM* 8
2.3 *The coupling and probability of the Z^0 boson to different final states* . 10

4.1 *Monte Carlo events available in ALEPH for this analysis. The numbers represent thousands of Class* 16 *events* 39

5.1 *Charm quark content of the D-candidates* 44
5.2 *Channels of D decays which are used by the present analysis* 44
5.3 *Channels of D decays which might be further used for this analysis* . 45

6.1 *Values of the parameters for the events used to train the NNs* 63

7.1 *The cuts applied for the preselection.* 65
7.2 *Number of candidates selected in MC and in Data after preselection cuts and before the cuts in the NN outputs and in the mass of the D meson.* 68
7.3 *The final cuts applied on the NN outputs, $p_{\overline{uds}}$ and $p_{\overline{b}}$, and on the mass of the D meson.* 78
7.4 *MC event numbers (rescaled to data), before NN cuts and after mass window cuts.* 78
7.5 *MC event numbers (rescaled to data), after NN and mass window cuts* 78
7.6 *Data event numbers, before NN cuts and after mass window cuts* . . 79
7.7 *Data event numbers, after NN and mass window cuts* 79
7.8 *Number of candidates selected after NN and before mass window cuts.* 83
7.9 *Number of candidates selected after NN and mass window cuts.* . . . 83
7.10 *Number of D candidates selected before and after reweighting the MC sample.* 84
7.11 *Number of D candidates in MC (rescaled to data), after the final selection.* 87
7.12 *Number of D candidates in real data, after the final selection.* 87
7.13 *Number of c and b true D candidates in MC (before rescaling to data), after the final selection.* 88
7.14 *Overview of the charm selection procedure in real data, at the working point.* 88

7.15 *Number of charmed true D candidates in real data and in MC samples (before rescaling to data).* 89

8.1 *MC-quantities updated in this analysis to the newest experimental values* 92
8.2 *The composition of MC background sample used as input for the NN training. This sample consisted of c-events, with an incorrect assignment of the charge, and uds-events.* 94
8.3 *Influence of the NN selection on the number of c-events with the electrical charge correctly assigned, shown for each analysed channel, as given by the MC sample* 95
8.4 *Number of lepton candidates with same and opposite charge before applying the correction* $\Delta N_{h,L}$. *These numbers are given for the data, the MC and the MC rescaled to data.* 98
8.5 *Various combinations of the signal with opposite charge and the signal with same charge.* 98
8.6 *Splitting of the total MC sample (rescaled to data) according to the authenticity of the D meson candidate and the origin of the lepton candidate.* 99
8.7 *Corrections* $\Delta N^{b}_{D,F|MC}$. 100
8.8 *Corrections* $\Delta N^{c}_{D,F|MC}$. 100
8.9 *Corrections* $\Delta N^{b}_{D,non\ prompt|MC}$. 101
8.10 *Corrections* $\Delta N^{c}_{D,non\ prompt|MC}$. 101
8.11 *Corrections* $\Delta N^{b}_{D,f|MC}$, *when b decays to a l directly, or via a c quark.* 102
8.12 *Corrections* $\Delta N^{c}_{D,f|MC}$. 102
8.13 *Corrections* $\Delta N^{b}_{D,l|MC}$ *when* $b \to l$. 102
8.14 *Corrections* $\Delta N^{b}_{D,l|MC}$ *when* $b \to c \to l$. 103
8.15 *Corrections* $\Delta N^{b}_{D,l|MC}$ *when* $b \to \overline{c} \to l$. 103
8.16 *Sum of corrections* $\Delta N^{b}_{D,l|MC}$. 103
8.17 *Corrections* $\Delta N^{b,c}_{F,f|MC}$ *for channel* (a). 104
8.18 *Corrections* $\Delta N^{b,c}_{F,f|MC}$ *for channel* (b). 104
8.19 *Corrections* $\Delta N^{b,c}_{F,f|MC}$ *for channel* (c). 105
8.20 *Corrections* $\Delta N^{b,c}_{F,f|MC}$ *for channel* (d). 105
8.21 *Corrections* $\Delta N^{b,c}_{F,f|MC}$ *for channel* (e). 105
8.22 *Corrections* $\Delta N^{b}_{F,l|MC}$. 106
8.23 *Corrections* $\Delta N^{c}_{F,l|MC}$. 106
8.24 *Corrections* $\Delta N^{uds}_{F,l|MC}$. 106
8.25 *The number of leptons in MC, due to MC corrections and their values without corrections.* 107

9.1 *The statistical error on the number of charmed D candidates selected in the data, and its sources.* 110
9.2 *The statistical error on the number of charmed D candidates selected in the MC, and its sources.* 110

9.3 *The absolute statistical errors due to the number of charmed D candidates.* . . . 111
9.4 *The absolute statistical errors due to the number of charmed $(D, l)^c$ lepton candidates.* . . . 111
9.5 *The absolute statistical errors due to the number of charmed D candidates and true prompt lepton candidates.* . . . 112
9.6 *Absolute statistical errors, due to real and Monte Carlo data.* . . . 113
9.7 *Uncertainties on the $BR(c \to l + X)$ due to wrong assignment of the electrical charge of the D meson.* . . . 114
9.8 *Systematic uncertainties on the $BR(c \to l + X)$ due to b and c fragmentation.* . . . 115
9.9 *Number of gluons splitting to heavy quarks per hadronic Z^0 decay* . . . 115
9.10 *Absolute systematic uncertainties on the $BR(c \to l+X)$ due to gluon splitting.* . . . 116
9.11 *Absolute systematic uncertainties on the $BR(c \to l + X)$ due to B-mixing.* . . . 116
9.12 *Absolute systematic uncertainties on the $BR(c \to l+X)$ due to lepton identification efficiency.* . . . 117
9.13 *Sources of systematic uncertainties on the $BR(c \to l + X)$ due to leptonic branching ratios experimental errors* . . . 117
9.14 *Absolute systematic uncertainties on the $BR(c \to l + X)$ due to leptonic branching ratios experimental errors* . . . 118
9.15 *Absolute systematic uncertainties on the $BR(c \to l+X)$ due to lepton misidentification and non-prompt leptons* . . . 118
9.16 *Absolute systematic uncertainties on the $BR(c \to l+X)$ due to lepton identification efficiency.* . . . 119
9.17 *Absolute systematic uncertainties on the $BR(c \to l+X)$ due to modelling of the leptonic decays.* . . . 120
9.18 *Input values and results in the weighting procedure applying the BLUE technique* . . . 124
9.19 *Composition of the total systematic uncertainty.* . . . 126

10.1 *$BR(c \to l + X)$ computed separately for the samples corresponding to each of the five years.* . . . 128
10.2 *Parameters of the Gaussian distribution fitting the resonance in the mass of the analysed D mesons.* . . . 130
10.3 *Stability Checks.* . . . 131
10.4 *Summary of the charm semileptonic branching ratios measurements presently available.* . . . 138

Lebenslauf

Familienname	: David
Vorname	: Aretina, Magdalena
Geburtsdatum	: 23 Februar, 1972 in Bukarest (Rumänien)
Adresse	: Natiunile Unite 8, Bl 104, Ap 75, RO-74317, Bukarest
Telefon	: 0040-21-336 25 91
E-mail	: aretina@mppmu.mpg.de

Ausbildung :

1999 – 2003	: Doktorarbeit im Rahmen des ALEPH Experimentes am Max-Planck Institut für Physik in München "Cum laude"
1997 – 1998	: Master of Science in Photonik und optischer Informationsübertragung an der Polytechnischen Universität, Bukarest Durchschnittsnote: 9.57/10
1992 – 1997	: Bachelor of Science in Computerwissenschaften an der Polytechnischen Universität, Bukarest Fakultät für Computer und Automation Durchschnittsnote: 8.35/10
1991 – 1995	: Universität Bukarest, Fakultät für Mathematik Durchschnittsnote: 8.48/10
1990 – 1995	: Bachelor of Science in Physik Schwerrpunkt: Fundamentale Interaktionen und Teilchenphysik an der Universität, Bukarest Durchschnittsnote: 9.94/10; Klassenbeste
1986 – 1990	: Nicolae Balcescu Gymnasium, Bukarest, Abitur(Mathematik-Physik)

Zusatzinformation:

seit 1999	Mitglied an der Deutschen Physikalischen Gesellschaft
seit 1997	Assistentin an der Polytechnischen Universität, Bukarest Fakultät für Electronik und Telekommunikation (Spl. Independentei 313, sect 6, 77206 Bukarest, Rumänien).

Besondere Kenntnisse :

Sprachen	: Deutsch, Englisch, Französisch, Italienisch, Russisch, Rumänisch
Physik	: Teilchenphysik, Nuklearphysik, Photonik, Informatik
Mathematik	: Statistische Modelle, Monte-Carlo Techniken, Optimierungstheorie, numerische Methoden, neurale Netze
Progammiersprachen	: Basic, C, C++, FORTRAN, Pascal
Betriebsysteme	: Unix, MS-DOS, Windows
Desweiteren	: Microsoft Office, Correl Draw, Latex, Lotus

Hobby :

Bergsteigen, Film, klassische Musik